INFORMATION TO USERS

This manuscript has been reproduced from the microfilm master. UMI films the text directly from the original or copy submitted. Thus, some thesis and dissertation copies are in typewriter face, while others may be from any type of computer printer.

The quality of this reproduction is dependent upon the quality of the copy submitted. Broken or indistinct print, colored or poor quality illustrations and photographs, print bleedthrough, substandard margins, and improper alignment can adversely affect reproduction.

In the unlikely event that the author did not send UMI a complete manuscript and there are missing pages, these will be noted. Also, if unauthorized copyright material had to be removed, a note will indicate the deletion.

Oversize materials (e.g., maps, drawings, charts) are reproduced by sectioning the original, beginning at the upper left-hand corner and continuing from left to right in equal sections with small overlaps.

Photographs included in the original manuscript have been reproduced xerographically in this copy. Higher quality 6" x 9" black and white photographic prints are available for any photographs or illustrations appearing in this copy for an additional charge. Contact UMI directly to order.

Bell & Howell Information and Learning
300 North Zeeb Road, Ann Arbor, MI 48106-1346 USA

UMI®
800-521-0600

NOTE TO USERS

This reproduction is the best copy available

UMI

OPTOELECTRONIC DEVICE MODELING USING FIELD SIMULATION TECHNIQUES

By

MINYA ZHANG

B. Sc., M. Eng.

A Thesis

Submitted to the School of Graduate Studies

in Partial Fulfilment of the Requirements

for the Degree

Doctor of Philosophy

McMaster University

May 1998

©Copyright 1998

OPTOELECTRONIC DEVICE MODELING USING FIELD SIMULATION TECHNIQUES

DOCTOR OF PHILOSOPHY (1998) MCMASTER UNIVERSITY

(Electrical and Computer Engineering) Hamilton, Ontario

TITLE: **Optoelectronic Device Modeling Using Field Simulation Techniques**

AUTHOR: Minya Zhang

B. Sc. (East China Normal University)

M. Eng. (McMaster University)

SUPERVISOR: Dr. D. R. Conn

Professor, Chairman of Department of Electrical and Computer Engineering

B.Sc., M.Sc., Ph.D. (Queen's University)

NUMBER OF PAGES: xviii, 167

ABSTRACT

Optoelectronic devices are important devices in optical fiber communications, optical signal processing, and optoelectronic equipment. This thesis develops new models for optoelectronic devices using electromagnetic field simulation techniques.

To demonstrate this new technique, two kinds of optoelectronic devices are investigated in this thesis. Vertical cavity surface emitting laser (VCSEL) is taken as the first research example due to the promising features in the application of fiber communications. A $LiTaO_3$ electro-optic (E-O) high-speed probe for external electro-optic sampling measurement is the second research example in terms of the need to develop a three-port electrical and optical model for the probe with the coplanar waveguide (CPW) test structure.

A new microcavity model for VCSEL is developed in this thesis. The model is based on optical wave equations and implemented with state-space techniques to predict the characteristics of the microcavities. The model can be used to analyze microcavities in both time and frequency domains in terms of the material

parameters and physical parameters of lasers and provides a simple and fast way to optimize cavity length, reflective mirror and material parameters.

A three-dimensional discrete time-domain electromagnetic modeling method for microcavities is developed in this thesis. Finite-difference transmission line matrix (FD-TLM) method is modified to involve the distributed optical gain region into the full wave simulation. A simplified microcavity model is developed with the effective mirror derived in this thesis to replace the quarter-wave stacks, and can be used in the full wave modeling of optoelectronic integrated systems having complex inhomogeneities. The near-field and far-field distribution of VCSELs is obtained for the design of interconnections in fiber communication systems.

A new dynamic equivalent circuit model for VCSEL is developed in this thesis to add to the equivalent circuit model family of lasers. To describe the laser dynamics, the microcavity model is coupled to the rate equations. A nonlinear resistance is used to represent the optical gain in the cavity. A spontaneous emission noise source is added to the equivalent circuit model to simulate the noise process throughout the laser operation, which is favored in the system modeling. Simulation results are compared with the direct rate equation solutions and show that the model is accurate and effective for providing the carrier, photon, optical field, output power, and frequency chirping response of the VCSEL in one simulation. The model enables the laser and its electrical driving circuit to be directly connected and analyzed in a unified manner and can be a powerful computer CAD model to be incorporated into nonlinear circuit modeling software. The model is a useful design tool because

it is such a close analogue to the laser device which may be easily modified and enhanced.

This thesis addresses the FD-TLM modeling of the $LiTaO_3$ E-O probe with coplanar waveguides (CPW) test structure with various configurations. A new system transfer function for the probe is defined to sample the signal directly on the sampling point. The full wave modeling of the probe with CPW test structure lays the foundation of the three-port electrical and optical model of $LiTaO_3$ probe with CPW test structure.

To diagnose integrated circuits, it is desirable to measure signal waveforms on internal circuits. $LiTaO_3$ probe is widely used in E-O sampling due to its high sensitivity and transverse sampling configuration matched to the CPW test structure. Three-port electrical and optical model of the $LiTaO_3$ probe with CPW test structure is extremely important to the calibration of E-O measurement. With neural network techniques, the field based three-port model is constructed to provide necessary data for the optimum E-O measurement. The three-port model has the same accuracy as the full wave modeling, but its characteristics are directly obtained from the neural network weighting parameters rather than the complicated full wave simulation. With this model, it is possible to de-embed both invasiveness and waveform distortion in the external E-O sampling by giving the sampling configurations, which moves E-O sampling further towards the quantitative measurement.

Acknowledgements

I would like to express sincere gratitude to my supervisor Dr. David R. Conn for his valuable supervision and constant support and encouragement throughout this Ph.D. program. Without his guidance, this work would not be possible.

I would like to thank Dr. John Litva and Dr. Stephen Chisholm for their important roles in my thesis supervisory committee.

I would also like to express my thanks to Dr. Conn's research group for their great discussions and help. I would like to thank Dr. Howard X. Wu for his insightful suggestion to this thesis, Mr. Kent Nickerson for his instructive discussion, and Mr. Ronald Hemmers for his helpful information.

Finally, I would like to give cordial thanks to my parents. I am especially indebted to my husband, Xiangqun Sun, and my daughter, Nike Sun. Without their constant understanding, support, and love, I would not have been able to successfully complete this work.

Contents

List of Figures

List of Tables

Chapter 1

Introduction

1.1 Purpose of the Research

The purpose of this research is to develop new models of optoelectronic devices using electromagnetic field simulation techniques.

Vertical cavity surface emitting laser (VCSEL) is selected as the first research example due to the promising features in the application of many areas [1]. The electromagnetic field inside the laser cavity satisfies Maxwell's equations, which gives the fundamentals of the laser research. To derive the microcavity model of vertical cavity surface emitting lasers, the electromagnetic wave theory is combined with the transmission line theory to obtain the equivalent circuit of microcavities and to estimate the value of each circuit element. The distributed Bragg reflector (DBR)

of a one dimensional cavity is modeled using the concept of reflection coefficient in electromagnetic theory and the concept of load resistance in transmission line theory. The optical gain in the microcavity is modeled by a negative nonlinear resistance which is derived from wave theory and transmission line theory. Such a microcavity model completely describes the wave propagation in the microcavity of a VCSEL. In order to investigate the dynamic properties of VCSEL using wave theory, a dynamic equivalent circuit model is developed to acquire the response of carrier number, photon number, optical field, phase, and frequency chirping in one simulation. To develop the dynamic model, rate equations are coupled to the microcavity model and coupling relationships are found using both electromagnetic wave theory and corpuscular concept. To implement the full wave modeling of the three-dimensional optical gain region in the microcavity, finite-difference transmission line matrix (FD-TLM) method is modified to simulate the optical gain in the simplified microcavity model with effective mirrors applied instead of the quarter-wave stacks. All the simulation results show that the wave theory is effective in the modeling of laser devices.

$LiTaO_3$ electro-optic (E-O) high-speed probes for external electro-optic sampling measurements are selected as the second research example because the birefringence of E-O crystals is best described by the wave theory. $LiTaO_3$ probes are widely used in E-O sampling measurements due to its high sensitivity and transverse sampling configuration matched to the high-bandwidth coplanar waveguide (CPW) test structure. A three-port electrical and optical model of the $LiTaO_3$

probe with CPW test structure is extremely important to the calibration of E-O measurements. The full wave simulation of the probe test structure with different CPW configurations lays the foundation of the three-port model. With the aid of neural network techniques, the field based three-port electrical and optical model is constructed for the fast and accurate calibration of E-O measurement which moves the E-O sampling technique further towards the quantitative measurement.

1.2 Organization of the Thesis

As a brief introduction of the thesis, Chapter 1 presents the purpose of the research and the organization of the thesis.

At the beginning of each following chapter, an introductory review is given on the topic of the chapter including its previous research, current status and the problems to be studied in the chapter. The introductory review is followed by a detailed description of the techniques conducted in each chapter and the relative results. Each chapter is concluded with a discussion regarding the topic of the chapter.

Chapter 2 starts with a detailed introduction of vertical cavity surface emitting lasers and their advantages and applications. The transmission line microcavity model is then developed and circuit parameters are estimated using wave theory and transmission line theory. The emphasis is the estimation of the negative resistance

for optical gain in the middle of the cavity. The state-space technique is used to simulate the microcavity model.

Chapter 3 presents the full wave modeling of microcavities. The FD-TLM method for the modeling of the three-dimensional distributed optical gain region is derived in this chapter. The effective mirror and the simplified microcavity model are also developed in the chapter. The full wave simulation result gives the near-field and far-field intensity distribution of the laser beam.

Chapter 4 develops a dynamic equivalent circuit model for VCSEL by coupling the microcavity model with rate equations. The model gives carrier number, photon number, optical field, output power, and frequency chirping of a VCSEL in one simulation. The important relationship between the photon number and the standing wave in the cavity is derived and the spontaneous emission noise source is developed in this chapter. Several important laser features are studied through the simulation, and the step response and modulation response are obtained through simulations.

Chapter 5 starts with a brief introduction of electro-optic sampling systems and the theory of E-O sampling. The new contributions to the full wave electromagnetic modeling of $LiTaO_3$ probes with CPW test structures of different configurations are addressed in the chapter. Variable grid size of the FD-TLM method is used to investigate the characteristics of the probe test structure. A new system transfer function for the probe with CPW test structure is defined in the chapter

for the direct signal sampling on the sampling spot.

Chapter 6 develops a three-port electrical and optical model of the $LiTaO_3$ probe with CPW test structure. The definition of the three-port model is discussed first. Then the fundamentals of neural network techniques are briefly introduced. The full wave simulations for the interested input range are carried out to obtain the corresponding output data. The three-port model is constructed by the input-output mapping of full wave simulation results using neural network techniques. The application of the three-port model in the calibration of E-O measurements for integrated circuits is also discussed.

Finally Chapter 7 completes the thesis with conclusions, contributions of the thesis, and recommendations for future research on laser modeling and E-O sampling measurement.

Chapter 2

Microcavity Model for Vertical Cavity Surface Emitting Lasers

Vertical cavity surface emitting lasers (VCSEL) and their advantages and applications are introduced and a new microcavity model for VCSEL is developed in this chapter. The model is based on optical wave equations and implemented with state-space techniques to predict the characteristics of microcavities. The results demonstrate the steady state of the single longitudinal mode of a VCSEL and decay properties of different microcavities. The model can be used to analyze microcavities in both time and frequency domains in terms of material parameters and physical parameters of the lasers and provides a simple and fast way to optimize cavity length, reflective mirror and material parameters. The model is also for the CAD of optoelectronic integrated circuits (OEIC).

2.1 Introduction

2.1.1 Introduction of Vertical Cavity Surface Emitting Lasers

Vertical cavity surface emitting lasers (VCSEL) are a new generation of semiconductor devices. The structure of a typical vertical cavity surface emitting laser is shown in Fig. 2.1. Surface emitting lasers have their optical cavities normal to the surfaces of the wafer [1] to form the Fabry-Perot (FP) cavity of the laser where the active region is sandwiched between the two n and p type Bragg mirrors [2]. The mirrors which provide the optical feedback are grown into the laser structure and composed of paired layers of two different materials, such as GaAs and AlAs. One material has a high refractive index and the other a low index. The mirrors can reflect approximately 99 percent of the optical power at the laser's emission wavelength and are known as quarter-wave stacks because each layer's thickness is equal to one-quarter of the wavelength of the light inside the material. Each quarter-wave stack serves two functions: as a highly reflecting mirror for the photons, and as a current path for the electrons and holes.

When a voltage is applied to the contacts, electrons and holes are injected through the opposing mirrors and collect in the laser's active region (or cavity). An electron and a hole can recombine at a random time to generate a photon. A photon is likely to stimulate a new electron and hole to recombine, issuing a new photon. The photon population in the cavity multiplies rapidly, and some of the photons

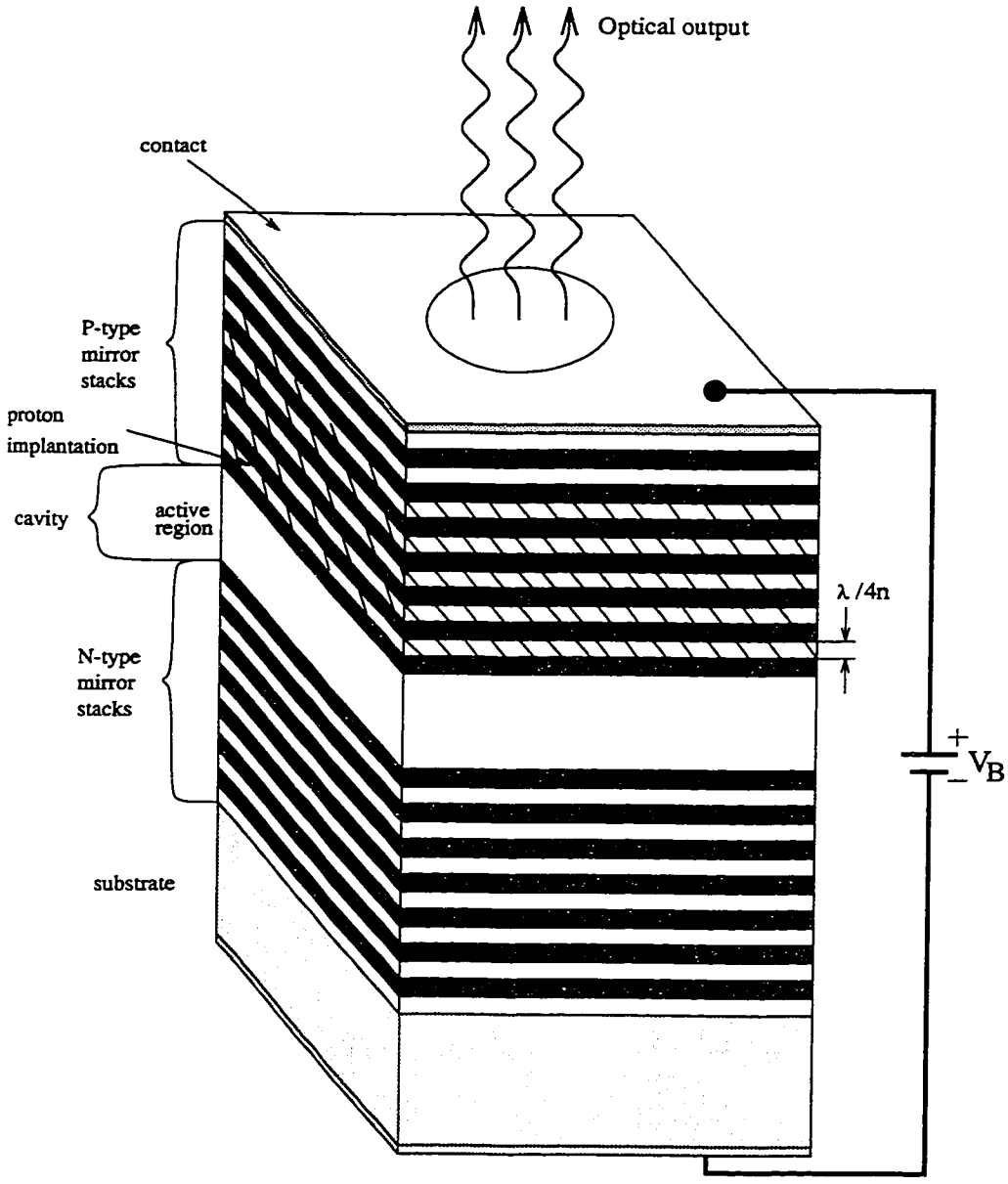

Figure 2.1: The structure of surface emitting laser. n is the refractive index of the material and V_B is the bias voltage source.

leak out through the circular aperture in the contact on one mirror, producing an intense beam of coherent light.

Two conditions are required to operate a laser: (i) a gain medium that can amplify the electromagnetic wave propagating inside the cavity and provide the spontaneous-emission noise input and (ii) a feedback mechanism that can confine the electromagnetic field through the well defined optical modes.

2.1.2 Advantages of Vertical Cavity Surface Emitting Lasers

The ultralow threshold current density of VCSEL is promising because of the high reflectivity of mirrors, the effective current confining structure, and the increased coupling of spontaneous emission into the cavity mode [3].

The ultrashort cavity of VCSEL allows only single longitudinal mode to lase which is expected in fiber communication systems.

Surface emitting lasers can be integrated on chip with transistors and other devices. There is no need to wire each of them individually to a circuit, as is done with edge emitters, and they can be optically linked to overhead elements.

The coupling efficiency of optical interconnections also benefits from a VCSEL. The beam of light that issues from an edge-emitter, typically through a 1-by-2μm aperture, is usually both elliptical and divergent. In contrast, the VCSEL aperture can be shaped to give the beam the ideal circular cross section and its

diameter can be made large enough, at $5\mu m$, to minimize the divergence of the light rays.

VCSEL can form a two-dimensional array whose power and direction can be controlled. The geometry of edge-emitters restricts them to one-dimensional arrays.

Wafer level testing can be done before packaging so that the packaging cost can be reduced. In contrast, a wafer of edge-emitters must be cleaved at least into separate laser bars - one-dimensional arrays - to create the mirrors before the devices can be tested.

2.1.3 Applications of Vertical Cavity Surface Emitting Lasers

Surface emitting approaches allow combining the power of hundreds or thousands of low power devices into a monolithic, coherent high power array of semiconductor lasers while maintaining the efficiency and spectral properties of the individual cleaved-facet semiconductor lasers.

A phase-locked two-dimensional array is attractive for high power and narrow circular beam operation. When phase-locked, all the lasers in the array operate in unison to create a narrow, coherent beam.

A promising application is multichannel optical-fiber communications. The technology is being used over short distances to link systems in local-area networks. Present surface-emitter performance and attributes are well matched to multichan-

nel systems of this kind. They can be easily fabricated into multi-emitter arrays, have the power and modal properties to propagate over a few hundred meters, and can be modulated at rates of up to a gigabit per second, while their circular beams are easily coupled into fibers.

As surface-emitters appear with 1.3— and $1.5 - \mu m$ wavelengths, they may replace the distributed-feedback edge-emitting lasers used today in long-haul optical-fiber communication systems. In these systems, the laser sources must emit light in a single mode within a narrow frequency range in order to minimize dispersion and noise. Now the ultrashort cavity of surface-emitters makes them lase in a single longitudinal mode.

2.2 Microcavity Model

In conventional cases, the lasing mode occurs at the gain peak. For the VCSEL the lasing wavelength is restrained by cavity design. In a typical surface-emitter laser design, the space between the two mirrors is very short. The lasing wavelength separation of the longitudinal optical modes is inversely proportional to the cavity length. Accordingly, the modes are separated by a wavelength which is wider than the spectrum of gain required for light amplification. It follows that in a surface-emitting laser, only one longitudinal mode should lase [1]. Optical microcavities and layered media are sensitive to the characteristics of optical fields, and slight changes in the cavity optical length or layer thickness and the optical properties of the

media can substantially change cavity resonant properties [4]. The FD-TD modeling of nonlinear Fabry-Perot cavities has been reported previously [4], the modeling method can be applied to VCSEL microcavities but uses excessive computational time and memory. There is a need to develop a simple equivalent circuit model which is suitable for the design and optimization of microcavities and the optical-electronic integration CAD. In this chapter, we introduce a new transmission line microcavity model by combining optical, electromagnetic, and transmission line theory.

Since the electromagnetic field inside the laser cavity satisfies Maxwell's equations, it is appropriate to investigate the microcavity using electromagnetic theory. Transmission line theory bridges the gap between field analysis and basic circuit theory. It is usually much easier to apply the simple and intuitive ideas of circuit analysis to a microwave problem than it is to solve Maxwell's equations for the same problem. It is then easy to modify the original problem, or combine several elements together and find the response, without having to analyze in detail the behavior of each element in combination with its neighbors.

Fig. 2.2 shows the various cavity modes in the one dimensional (vertical) microcavity. There may exist not only a Bragg resonant mode, but also leaky wave and propagation modes. By neglecting the leaky wave and propagation mode, only the Bragg resonant mode in the one-dimensional cavity is taken into account as a lasing mode [5]. Since the length of the vertical cavity is short, only a single longitudinal mode can exist in the cavity [6]. This property is the foundation of the microcavity model introduced in this chapter.

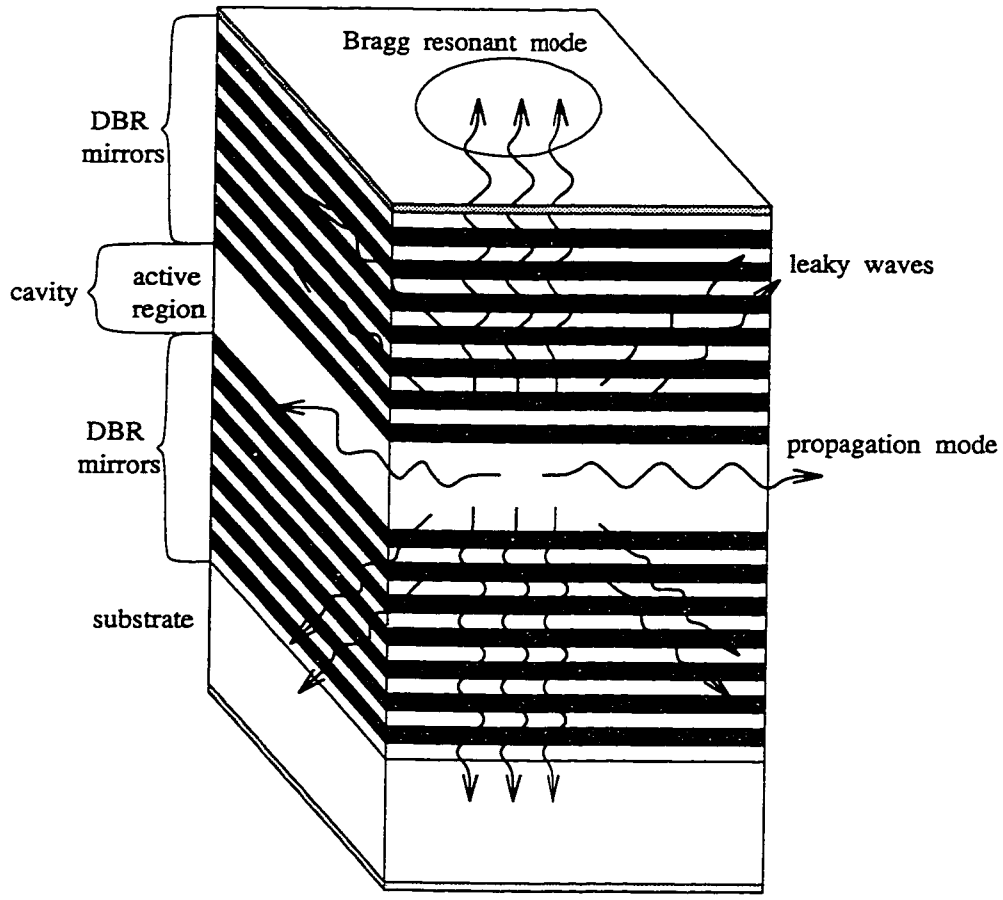

Figure 2.2: One-dimensional (vertical) microcavity. By neglecting the leaky wave and propagation mode, only the Bragg resonant mode in the one-dimensional cavity is taken into account as a lasing mode.

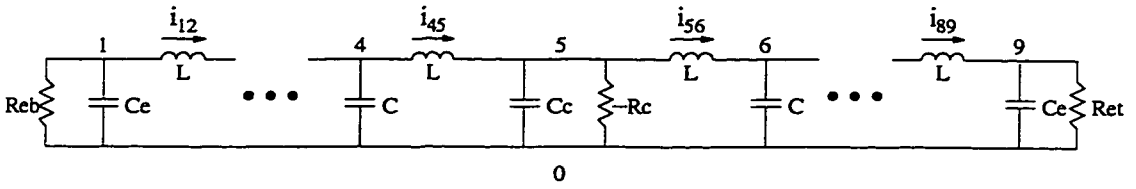

Figure 2.3: Transmission line microcavity model.

Based on the mode analysis, a simple transmission line microcavity model (Fig. 2.3) is developed to study the microcavities and steady-state properties of VCSELs by using the combination of transmission line and microwave networks. Generally speaking, the overall microcavity (Fig. 2.2) can be divided into active and Bragg regions. In the circuit model, a section of transmission line is used to model microcavities by assuming that the internal loss is negligible compared to the mirror loss of the cavity [6], and a negative resistance in the middle of the transmission line is used to model the optical gain of the active region. In steady state, the gain is constant corresponding to a fixed injection current flowing through the cavity. A resistance at each end of the transmission line is used to model Bragg mirror loss. The following section will give the detailed development procedure of the microcavity model.

2.3 Development of the Microcavity Model and Estimation of Circuit Parameters

2.3.1 Estimation of Inductances and Capacitances

It is assumed that the wave propagating inside a microcavity is a plane wave as a first-order approximation [7, 8, 9]. A transmission line is a distributed-parameter network, where voltages and currents can vary in magnitude and phase over its length. A short section of the transmission line of length Δz of Fig. 2.4 (a) can be modeled as a lumped-element circuit, as shown in Fig. 2.4 (b), where L_0 is the series inductance per unit length, C_0 is the shunt capacitance per unit length, R_0 is the series resistance per unit length which represents the resistance due to the finite conductivity of the conductors, G_0 is the shunt conductance per unit length which represents the dielectric loss in the material. R_0 and G_0, therefore, represent loss. A finite length of transmission line can be viewed as a cascade connection of sections in the form of Fig. 2.4 (b).

From the circuit of Fig. 2.4 (b), the wave equations for $V(z)$ and $I(z)$ can be written as [10]:

$$\frac{d^2V(z)}{dz^2} - \gamma^2 V(z) = 0 \tag{2.1a}$$

$$\frac{d^2I(z)}{dz^2} - \gamma^2 I(z) = 0 \tag{2.1b}$$

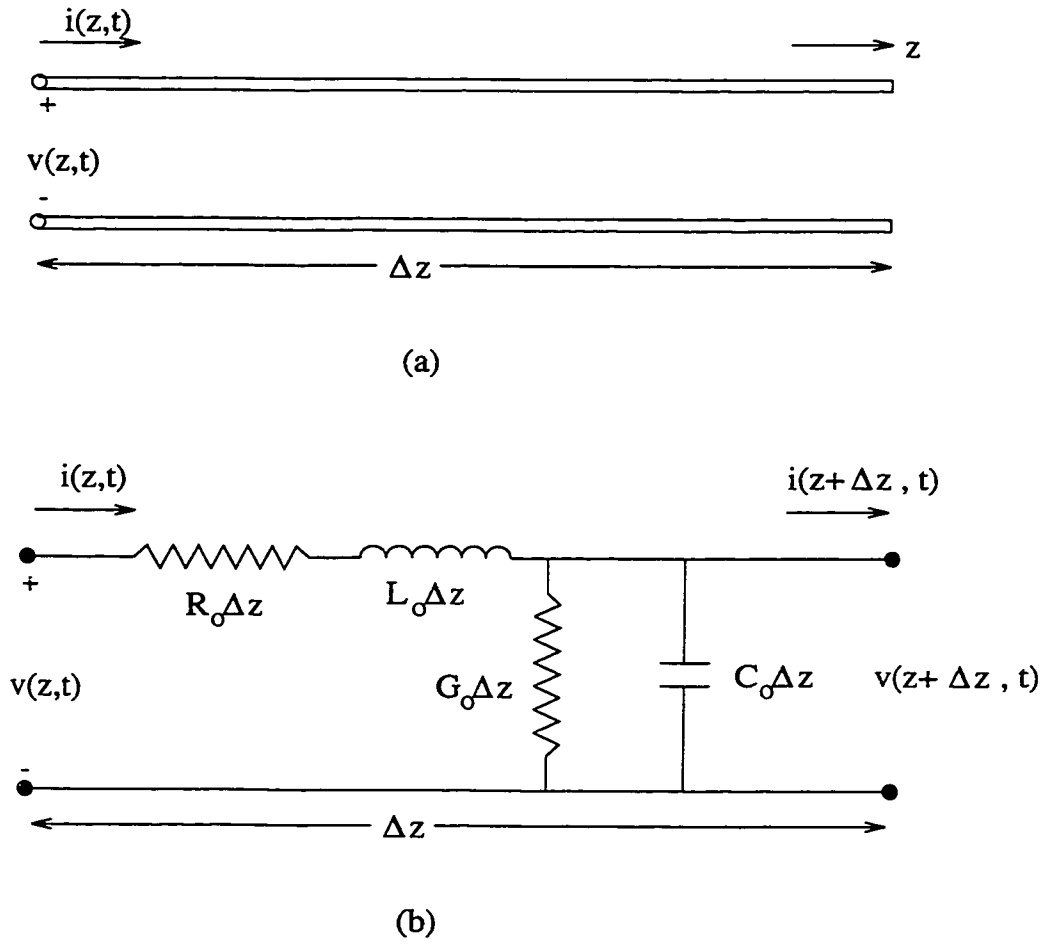

Figure 2.4: Voltage and current definitions and equivalent circuit for an incremental length of transmission line [10]. (a) Voltage and current definitions. (b) Lumped-element equivalent circuit.

where

$$\gamma = \alpha_a + j\beta = \sqrt{(R_0 + j\omega L_0)(G_0 + j\omega C_0)} \tag{2.2}$$

is the complex propagation constant, which is a function of frequency. α_a is the attenuation constant and β is the phase constant. The characteristic impedance Z_c can be related to the voltage and current on the line as

$$\frac{V^+}{I^+} = Z_c = -\frac{V^-}{I^-} \tag{2.3}$$

and defined as

$$Z_c = \sqrt{\frac{R_0 + j\omega L_0}{G_0 + j\omega C_0}} \tag{2.4}$$

The transmission line for the microcavity model is assumed to be lossless, therefore, R_0 and G_0 in the cavity are equal to zero.

The cavity is modeled using a plane wave approximation [7]. From the transmission line theory and the wave impedance for the plane wave [10], we have

$$Z_c = \sqrt{\frac{L_0}{C_0}} = \frac{120\pi}{n} \tag{2.5}$$

$$v_g = \frac{1}{\sqrt{L_0 C_0}} = \frac{c}{n} \tag{2.6}$$

where the characteristic impedance of the transmission line Z_c is assumed to be equal to the intrinsic impedance of a lossless dielectric medium [10]. n is the refractive index of the dielectric medium. v_g is the wave velocity in dielectric medium [10] and c is the wave velocity in free space. Solving (2.5) and (2.6), we get

$$C_0 = \frac{1}{Z_c v_g} \tag{2.7a}$$

$$L_0 = \frac{Z_c}{v_g}. \tag{2.7b}$$

The simplest approach to fabricating an optical microcavity is to shrink the spacing between the mirrors of an FP cavity to a wavelength inside the cavity material [2]. This structure provides a single dominant longitudinal mode that radiates into a narrow range of angles around the cavity axis. Based on this structure, the total length of the transmission line representing the cavity equals to a wavelength inside the material. In the circuit model, the transmission line consists of eight sections, and the length of each section is

$$dz = \lambda_g/8 \tag{2.8}$$

where the guided wavelength λ_g is related to the free-space wavelength λ by

$$\lambda_g = \lambda/n \tag{2.9}$$

The capacitance C and inductance L in the circuit can be calculated as

$$C = C_0 dz \tag{2.10a}$$

$$L = L_0 dz \tag{2.10b}$$

The capacitance C_c in the middle of the cavity equals to C and the capacitance C_e at each end of the cavity equals to $C/2$.

2.3.2 Estimation of Resistances

The resistances R_{et} and R_{eb} representing the Bragg mirror loss at the top and bottom of the cavity can be estimated by using the relationship between the load impedance and reflection coefficient of the transmission line [10]

$$R_{et} = R_{eb} = Z_c \frac{1+\Gamma_m}{1-\Gamma_m} = Z_c \frac{1+\sqrt{R_m}}{1-\sqrt{R_m}} \tag{2.11}$$

where Γ_m is the voltage reflection coefficient of the mirror, R_m is the optical power reflectivity of the mirror.

The most critical work for the microcavity model is the estimation of the negative resistance which represents the optical gain of the cavity. The negative resistance in the microcavity model is estimated by combining optical wave theory, electromagnetic theory, and transmission line theory. The combining of the above theories for the estimation of the circuit parameters which are related to the optical gain is first significantly reported in this chapter.

The discussion starts from optical wave theory. The mathematical description of all optical phenomena is based on Maxwell's equations which are used to obtain the wave equations that describe the propagation of an optical field inside the medium. Using the complex notation, we write a time-varying optical field as [6]

$$\mathcal{E}(x,y,z,t) = Re[\mathbf{E}(x,y,z)\exp(-j\omega t)] \tag{2.12}$$

where $\omega = 2\pi c/\lambda$. The time-independent wave equation for the electric field $\mathbf{E}$ is

derived from Maxwell's equations using classical method and is written as

$$\nabla^2 \mathbf{E} + \epsilon k_0^2 \mathbf{E} = 0 \tag{2.13}$$

where we have introduced the complex dielectric constant ϵ and $k_0 = 2\pi/\lambda$ is the vacuum wave number.

The wave equation (2.13) can be solved to obtain the spatial mode structure of the optical field. In place of using the complex dielectric constant in (2.13), the propagation characteristics of a plane wave in a medium are conveniently described in terms of two optical constants, the refractive index of the medium n and the power absorption coefficient α. Consider a plane wave propagating in the positive z direction such that [6]

$$\mathbf{E} = \hat{\mathbf{x}} E_0 \exp(j\tilde{\beta} z) \tag{2.14}$$

where $\hat{\mathbf{x}}$ is the polarization unit vector, E_0 is the constant amplitude. The complex propagation constant $\tilde{\beta}$ is determined by substituting Eq. (2.14) in Eq. (2.13) and is given by

$$\tilde{\beta} = k_0 \sqrt{\epsilon} = k_0 \tilde{n} \tag{2.15}$$

where $\tilde{n}$ is the complex index of refraction and can be written as [6]

$$\tilde{n} = n + j\frac{\alpha}{2k_0} \tag{2.16}$$

Substituting (2.16) in (2.15), we get the complex propagation constant

$$\tilde{\beta} = nk_0 + j\frac{\alpha}{2} \tag{2.17}$$

Substituting (2.17) into (2.14), we get the optical field in the plane-wave approximation

$$\begin{aligned} \mathbf{E} &= \hat{\mathbf{x}} E_0 \exp[j(nk_0 + j\frac{\alpha}{2})z] \\ &= \hat{\mathbf{x}} E_0 \exp(-\frac{\alpha z}{2} + jnk_0 z) \end{aligned} \tag{2.18}$$

The absorption coefficient can be written as [6]

$$\alpha = -\Gamma g + \alpha_{int}. \tag{2.19}$$

The confinement factor Γ [6] is introduced here. g is the optical gain and α_{int} is the internal loss coefficient. Substituting (2.19) into (2.18), we have

$$\mathbf{E} = \hat{\mathbf{x}} E_0 \exp\left(\frac{\Gamma g - \alpha_{int}}{2} z\right) \exp(jnk_0 z). \tag{2.20}$$

Substituting (2.20) into (2.12), we obtain the time-varying optical field

$$\begin{aligned} \mathcal{E}(x,y,z,t) &= Re\left[\hat{\mathbf{x}} E_0 \exp\left(\frac{\Gamma g - \alpha_{int}}{2} z\right) \exp(jnk_0 z) \exp(-j\omega t)\right] \\ &= \hat{\mathbf{x}} E_0 \exp\left(\frac{\Gamma g - \alpha_{int}}{2} z\right) \cos(\omega t - nk_0 z) \end{aligned} \tag{2.21}$$

Next, the expression of the electric field using electromagnetic theory will be derived. In most text books on electromagnetic theory, the time-varying electric field is written as

$$\mathcal{E}(x,y,z,t) = Re[\mathbf{E}(x,y,z)\exp(j\omega t)] \tag{2.22}$$

The time-independent wave equation for $\mathbf{E}$ in a general lossy medium can be derived as [10]

$$\nabla^2 \mathbf{E} + \omega^2 \mu \epsilon \mathbf{E} = 0 \tag{2.23}$$

where ϵ is complex dielectric constant and μ is permeability. The complex propagation constant for the medium is defined as

$$\gamma = \alpha_a + j\beta = j\omega\sqrt{\mu\epsilon} \tag{2.24}$$

If we again assume an electric field with only an x component, and uniform in x and y directions,

$$\mathbf{E} = \hat{\mathbf{x}} E_x(z) \tag{2.25}$$

the wave equation of (2.23) reduces to

$$\frac{d^2 E_x(z)}{dz^2} - \gamma^2 E_x(z) = 0 \tag{2.26}$$

which has the solution

$$E_x(z) = E_0^+ \exp(-\gamma z) + E_0^- \exp(\gamma z) \tag{2.27}$$

Combining (2.25) and (2.27), the positive travelling wave then has the form

$$\begin{aligned} \mathbf{E} &= \hat{\mathbf{x}} E_0^+ \exp(-\gamma z) \\ &= \hat{\mathbf{x}} E_0^+ \exp(-\alpha_a z) \exp(-j\beta z) \\ &= \hat{\mathbf{x}} E_0^+ \exp(-\alpha_a z) \exp(-jnk_0 z) \end{aligned} \tag{2.28}$$

Substituting (2.28) in (2.22), we obtain the time-varying electric field

$$\begin{aligned} \mathcal{E}(x,y,z,t) &= Re[\hat{\mathbf{x}} E_0^+ \exp(-\alpha_a z) \exp(-jnk_0 z) \exp(j\omega t)] \\ &= \hat{\mathbf{x}} E_0^+ \exp(-\alpha_a z) \cos(\omega t - nk_0 z) \end{aligned} \tag{2.29}$$

Since the optical wave is an electromagnetic wave, (2.21) and (2.29) must be equal. Comparing (2.21) and (2.29), we obtain the attenuation constant

$$\alpha_a = \frac{\alpha_{int} - \Gamma g}{2}. \tag{2.30}$$

Eq. (2.30) gives the relationship between the attenuation constant of electromagnetic waves and the optical gain and cavity internal loss.

Transmission line theory has been introduced in the previous section. For low-loss transmission lines, some approximations can be made that simplify the expressions for the general transmission line parameters of $\gamma = \alpha_a + j\beta$. The general expression for the complex propagation constant of (2.2) can be rearranged as

$$\begin{aligned} \gamma &= \sqrt{(R_0 + j\omega L_0)(G_0 + j\omega C_0)} \\ &= \sqrt{(j\omega L_0)(j\omega C_0)\left(1 + \frac{R_0}{j\omega L_0}\right)\left(1 + \frac{G_0}{j\omega C_0}\right)} \\ &= j\omega\sqrt{L_0 C_0}\sqrt{1 - j\left(\frac{R_0}{\omega L_0} + \frac{G_0}{\omega C_0}\right) - \frac{R_0 G_0}{\omega^2 L_0 C_0}} \end{aligned} \tag{2.31}$$

If the transmission line is low-loss we can assume that $R_0 << \omega L_0$ and $G_0 << \omega C_0$. Then, $R_0 G_0 << \omega^2 L_0 C_0$ and (2.31) reduces to

$$\gamma = j\omega\sqrt{L_0 C_0}\sqrt{1 - j\left(\frac{R_0}{\omega L_0} + \frac{G_0}{\omega C_0}\right)} \tag{2.32}$$

If we were to ignore the $(R_0/\omega L_0 + G_0/\omega C_0)$ term, we would obtain the result that γ was purely imaginary (no loss), so we will instead use the first two terms of the Taylor series expansion for $\sqrt{1+x} \simeq 1 + x/2 + \cdots$, to give the first high-order real term for γ:

$$\gamma \simeq j\omega\sqrt{L_0 C_0}\left[1 - \frac{j}{2}\left(\frac{R_0}{\omega L_0} + \frac{G_0}{\omega C_0}\right)\right] \tag{2.33}$$

so that

$$\alpha_a = \frac{1}{2}\left(R_0\sqrt{\frac{C_0}{L_0}} + G_0\sqrt{\frac{L_0}{C_0}}\right) = \frac{1}{2}\left(\frac{R_0}{Z_c} + G_0 Z_c\right) \tag{2.34a}$$

$$\beta = \omega\sqrt{L_0 C_0} \tag{2.34b}$$

Now, we combine three theories and estimate the negative resistance. Comparing (2.30) and (2.34a), we have

$$\alpha_{int} - \Gamma g = \frac{R_0}{Z_c} + G_0 Z_c. \tag{2.35}$$

Straightforwardly, cavity internal loss and optical gain are spacially discretized by using series resistance and shunt conductance, respectively, i.e.,

$$\alpha_{int} = \frac{R_0}{Z_c} \tag{2.36a}$$

$$-\Gamma g = G_0 Z_c. \tag{2.36b}$$

R_0 and G_0 are obtained as

$$R_0 = \alpha_{int} Z_c \tag{2.37a}$$

$$G_0 = -\frac{\Gamma g}{Z_c} \tag{2.37b}$$

In the microcavity model, $R_0 = 0$ is assumed because α_{int} is neglected.

A negative resistance in the middle of the cavity is used to model the optical gain. The negative resistance is found by equating the time-independent powers generated from whole active region and from the negative resistance. It is noticed that the cavity length L_c of VCSEL is rather short and is equal to the integer times of the guided wavelength [5, 11],

$$L_c = m\lambda_g, \quad m = 1, 2, 3, \cdots \tag{2.38}$$

The spacial distribution of the voltage standing wave along the cavity length is written as $v(l) = V_m \cos(\beta l)$, where V_m is the time-independent peak voltage of the standing wave. The time-independent power generated from a small section of transmission line dl is

$$dp_g = v^2(l) G_0 dl = G_0 V_m^2 \cos^2(\beta l) dl \tag{2.39}$$

The time-independent power generated from the whole active region is

$$\begin{aligned} P_g &= \int_{-\frac{L_c}{2}}^{\frac{L_c}{2}} dp_g \\ &= \int_{-\frac{L_c}{2}}^{\frac{L_c}{2}} G_0 V_m^2 \cos^2(\beta l) dl \\ &= G_0 V_m^2 \frac{L_c}{2} \end{aligned} \tag{2.40}$$

which must be equal to the time-independent power generated from the negative conductance in the middle of the cavity

$$P_g = G_c V_m^2 \tag{2.41}$$

From above two equations, the negative conductance for the optical gain is obtained as

$$G_c = G_0 \frac{L_c}{2} = -\frac{L_c \Gamma g}{2 Z_c} \tag{2.42}$$

The negative resistance $-R_c = 1/G_c$,

$$R_c = -\frac{1}{G_c} = \frac{2 Z_c}{L_c \Gamma g} \tag{2.43}$$

In the steady state near threshold, the material gain must compensate for the mirror loss where the mirror loss is considered dominant and has a reflectivity R_m for each

mirror [6], i.e.,

$$\Gamma g = \frac{1}{L_c} \ln\left(\frac{1}{R_m}\right) \tag{2.44}$$

Then, R_c for the steady-state can be written as

$$R_c = \frac{2Z_c}{\ln\left(\frac{1}{R_m}\right)}. \tag{2.45}$$

This result is directly used in the microcavity model.

2.4 State-Space Simulation

The state-space technique comes from linear system theory [12, 13]. It is a systematic approach for analyzing a linear time-invariant differential system. The dynamics of the system are determined by the rate of the change of the capacitance voltages and the inductance currents in the circuit and can be obtained by solving state-space equations. Since the microcavity model is a linear force-free system, the state equation takes the form

$$\dot{\mathbf{x}} = \mathbf{A}\mathbf{x} \tag{2.46}$$

where $\mathbf{x}$ is the vector of state variables of dimension N, $\mathbf{A}$ is the characteristic matrix of system of dimension $N \times N$, $\cdot$ represents the time derivative. The solution

of the vector differential equation is

$$\mathbf{x}(t) = e^{\mathbf{A}t}\mathbf{x}_0 = \mathbf{S}\begin{bmatrix} e^{\lambda_1 t} & 0 & 0 & \cdots & 0 \\ 0 & e^{\lambda_2 t} & 0 & \cdots & 0 \\ & & \cdot & & \\ & & & \cdot & \\ & & & & \cdot \\ 0 & 0 & 0 & \cdots & e^{\lambda_N t} \end{bmatrix}\mathbf{S}^{-1}\mathbf{x}_0 \tag{2.47}$$

where $\mathbf{x}_0$ is the initial condition of the system, the eigenvalues $\lambda_1, \lambda_2, \cdots, \lambda_N$ of $\mathbf{A}$ are determined by the characteristic equation

$$\det(\mathbf{A} - \lambda\mathbf{I}) = 0 \tag{2.48}$$

and the corresponding eigenvectors $\mathbf{u}_1, \mathbf{u}_2, \cdots, \mathbf{u}_N$ of $\mathbf{A}$ are determined by the equation

$$[\mathbf{A} - \lambda\mathbf{I}]\mathbf{u} = 0 \tag{2.49}$$

the matrix $\mathbf{S}$ is formed by taking the eigenvectors of $\mathbf{A}$ as its columns

$$\mathbf{S} = [\mathbf{u}_1\mathbf{u}_2\cdots\mathbf{u}_N]. \tag{2.50}$$

According to Kirchhoff's voltage and current laws, the state equations for the microcavity model in Fig. 2.3 are written as

$$\begin{aligned} \frac{dv_{10}}{dt} &= -\frac{v_{10}}{R_{eb}C_e} - \frac{i_{12}}{C_e} \\ \frac{dv_{20}}{dt} &= \frac{i_{12}}{C} - \frac{i_{23}}{C} \end{aligned}$$

$$
\begin{aligned}
\frac{dv_{30}}{dt} &= \frac{i_{23}}{C} - \frac{i_{34}}{C} \\
\frac{dv_{40}}{dt} &= \frac{i_{34}}{C} - \frac{i_{45}}{C} \\
\frac{dv_{50}}{dt} &= \frac{v_{50}}{R_c C_c} + \frac{i_{45}}{C_c} - \frac{i_{56}}{C_c} \\
\frac{dv_{60}}{dt} &= \frac{i_{56}}{C} - \frac{i_{67}}{C} \\
\frac{dv_{70}}{dt} &= \frac{i_{67}}{C} - \frac{i_{78}}{C} \\
\frac{dv_{80}}{dt} &= \frac{i_{78}}{C} - \frac{i_{89}}{C} \\
\frac{dv_{90}}{dt} &= -\frac{v_{90}}{R_{et} C_e} + \frac{i_{89}}{C_e} \\
\frac{di_{12}}{dt} &= \frac{v_{10}}{L} - \frac{v_{20}}{L} \\
\frac{di_{23}}{dt} &= \frac{v_{20}}{L} - \frac{v_{30}}{L} \\
\frac{di_{34}}{dt} &= \frac{v_{30}}{L} - \frac{v_{40}}{L} \\
\frac{di_{45}}{dt} &= \frac{v_{40}}{L} - \frac{v_{50}}{L} \\
\frac{di_{56}}{dt} &= \frac{v_{50}}{L} - \frac{v_{60}}{L} \\
\frac{di_{67}}{dt} &= \frac{v_{60}}{L} - \frac{v_{70}}{L} \\
\frac{di_{78}}{dt} &= \frac{v_{70}}{L} - \frac{v_{80}}{L} \\
\frac{di_{89}}{dt} &= \frac{v_{80}}{L} - \frac{v_{90}}{L}
\end{aligned}
\tag{2.51}
$$

where the first subscript denotes the starting point of a voltage v or a current i, the second subscript denotes the ending point of the voltage or current, the state vector is

$$
\begin{aligned}
\mathbf{x} = [&v_{10}\ v_{20}\ v_{30}\ v_{40}\ v_{50}\ v_{60}\ v_{70}\ v_{80}\ v_{90} \\
&i_{12}\ i_{23}\ i_{34}\ i_{45}\ i_{56}\ i_{67}\ i_{78}\ i_{89}]'
\end{aligned}
\tag{2.52}
$$

The eigenvector corresponding to the lasing mode is used as the initial condition $\mathbf{x}_0$ in the simulation. The parameters for the model are selected as [3]: $\lambda = 0.85\mu m$, $R_m = 0.98$, $n = 3.55$.

First, the state equations for steady state are solved and the cavity modes are determined, the voltages on each capacitance being obtained directly from the solution. The voltages on the nodes within the first quarter of the cavity have the same phase as shown in Fig. 2.5. The voltages on the nodes in the middle and at the end of the cavity are out of phase as shown in Fig. 2.6. The standing wave properties can be seen clearly from Fig. 2.7, where the voltage reaches the peak when the current reaches zero, which indicates a 90 degree phase shift between them.

Second, the state equations are solved for the transparency condition inside the cavities by taking $-R_c$ away from the circuit. The lasing mode then becomes the decay mode shown in Fig. 2.8. The photon decay rate $\gamma_p = 1/\tau_p$ [6] taken from the real parts of the eigenvalues versus cavity length and reflectivity (Fig. 2.9) shows that the bigger the reflectivity and the longer the cavity, the smaller the decay rate.

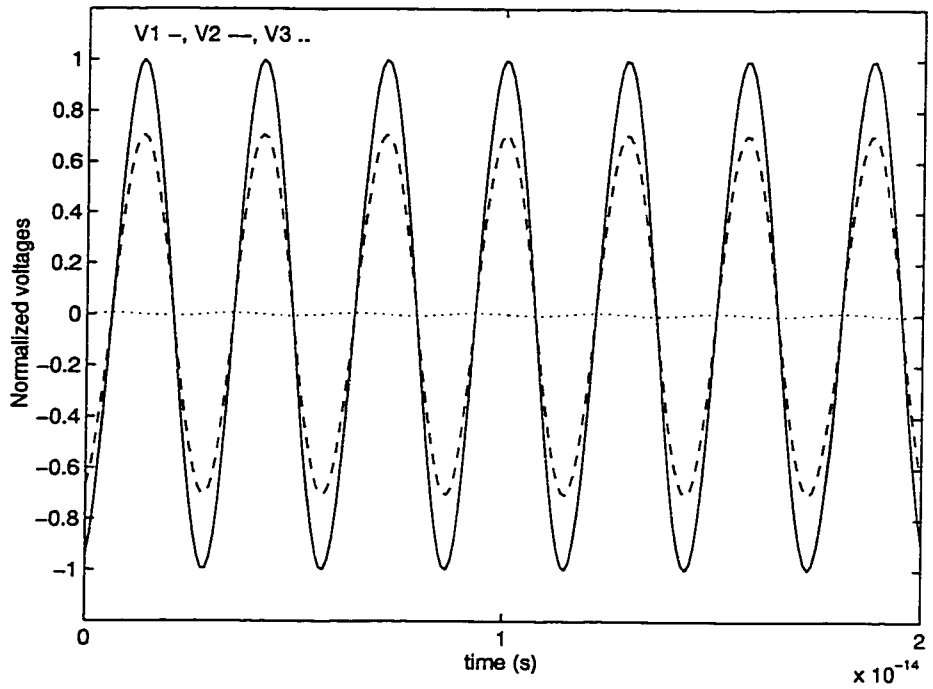

Figure 2.5: The voltage waveforms on node 1, 2, 3.

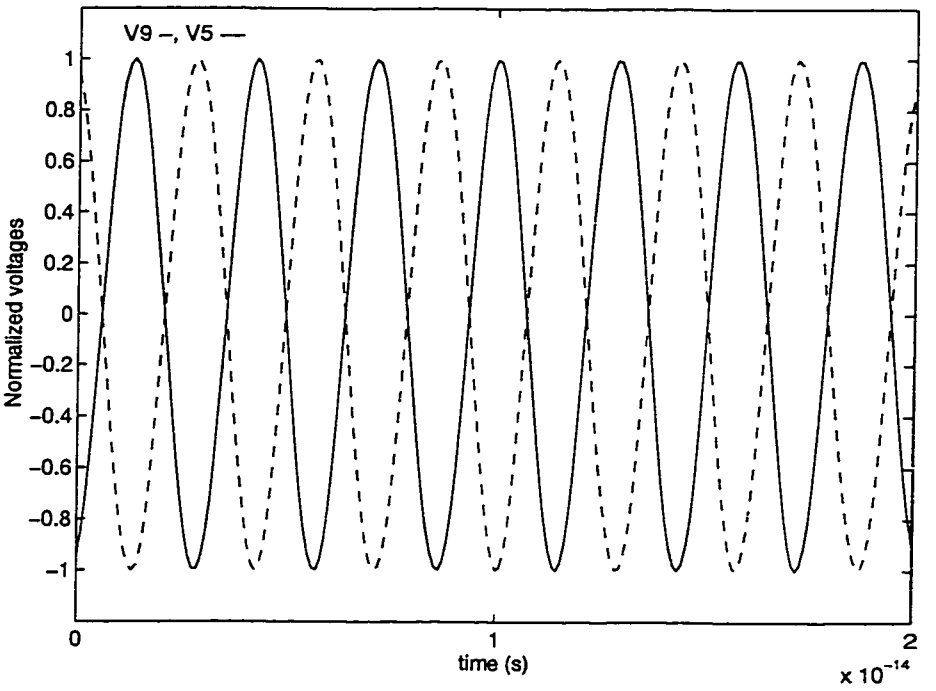

Figure 2.6: The voltage waveforms on node 5 and 9.

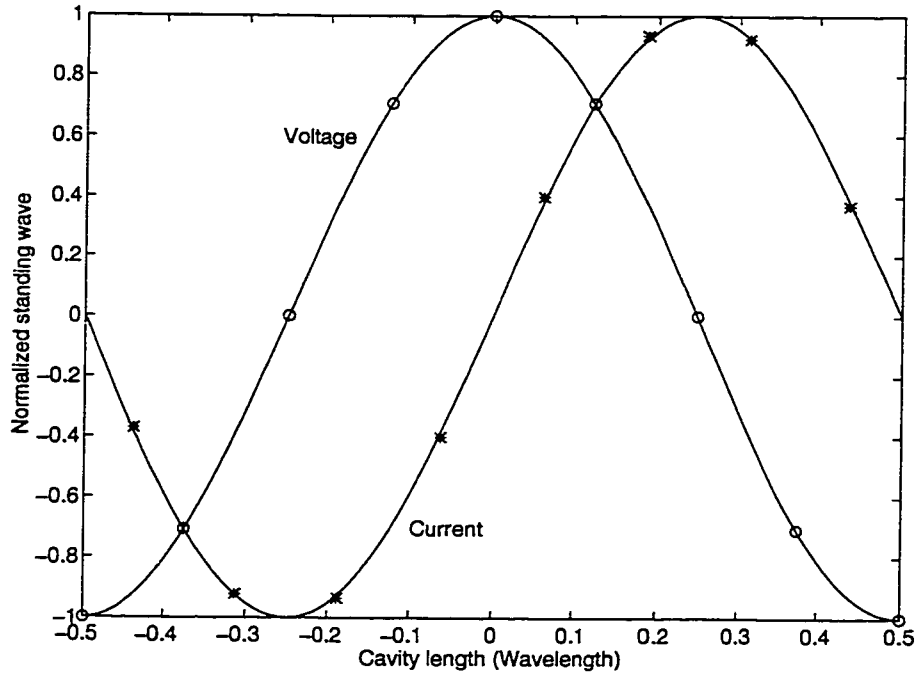

Figure 2.7: The standing wave in the cavity.

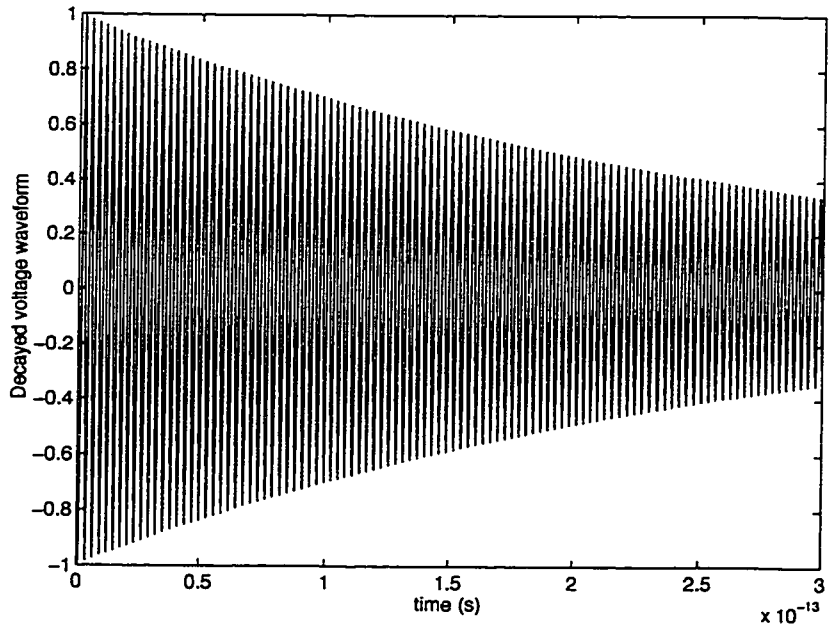

Figure 2.8: The waveform of the decay mode.

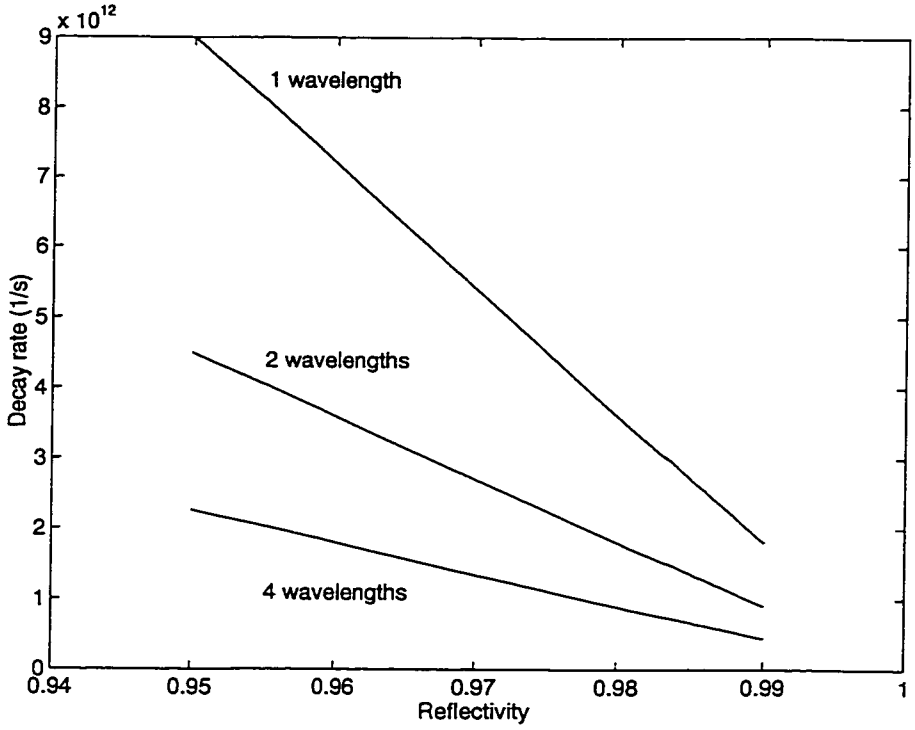

Figure 2.9: Decay rate versus reflectivity and cavity length.

2.5 Concluding Remarks

The microcavity model can be used to analyze microcavities in terms of the material and physical parameters of lasers. The results demonstrate the steady state of the single longitudinal mode of a microcavity and the decay rates of different cavities. The technique described in this section provides a simple and fast way to optimize the cavity length, reflective mirror and material parameters [14, 15].

Chapter 3

Full Wave Modeling of Microcavities

In this chapter, the discrete time-domain full wave modeling of microcavities is addressed. A simple three-dimensional microcavity model is developed to include three-dimensional distributed optical gain region and the effective mirror which is derived in this chapter to replace the quarter-wave stacks. The near-field and far-field distributions of VCSEL are obtained from the full wave simulation.

3.1 Introduction

In recent years, semiconductor lasers have been widely used in fiber communication, optical sensors, and optical measurements. In almost all of these applications, the

maximum available power of a diode laser is determined not only by its maximum output but also by its beam shape. An understanding of the beam shape has been considered desirable for evaluating the diode-fiber coupling efficiency and designing the optical connecting elements. Although the beam propagation method [16] has been used to obtain near and far field patterns, it is difficult to apply this method to the simulation of optical and electronic integrated circuits. Finite-difference transmission line matrix method (FD-TLM) [17] is an excellent candidate to simulate integrated systems with electronic devices, microwave passive components and active devices, and optical devices. In this chapter we present a three-dimensional full-wave FD-TLM model for microcavities. The distributed optical gain region in the microcavity is implemented in the FD-TLM method for the first time. Standing wave properties as well as near and far field patterns are obtained from simulations. The model can be used in the modeling of OEIC systems having complex engineered inhomogeneities and also provides a guide for the design of surface emitting lasers and optical systems.

3.2 Finite-Difference Transmission-Line Matrix (FD-TLM) Method

The transmission-line matrix (TLM) method was pioneered by Johns and Beurle [19] as a two-dimensional time-domain electromagnetic field solution technique. Later,

Akhtarzad and Johns developed a three-dimensional TLM method that greatly expanded the capability of the TLM method to new applications. Finite-difference time-domain (FD-TD) method [20] has been in use for solving time-domain electromagnetic problems [21], [22]. There are similarities between the TLM method and the FD-TD method [23], [24]. The finite-difference transmission-line matrix (FD-TLM) method [17] is a combination of the TLM method and FD-TD method, offering a physical basis for wave propagation and the numerical stability of the TLM method and the computational efficiency of the FD-TD method. The three-dimensional variable-mesh TLM method is based on transmission lines having different impedances. The TLM method is transformed into the FD-TLM method by rewriting the TLM scattering matrices as finite differences.

The three-dimensional TLM method is based on pulses which travel along transmission lines interconnected as a three-dimensional matrix and then scatter at the intersections (nodes) into other connecting lines. Figure 3.1 shows a cell of six nodes that is repeated throughout the structure to be simulated. In the uniform-mesh case, the mesh size $u = v = w = \Delta l$ and the lines all have length $\Delta l/2$ and the impedance of free space. There are two types of nodes: shunt nodes, where the voltage corresponds to an electric field; and series nodes, where the circulating current corresponds to a magnetic field. By calculating the voltage at a shunt node and the current through a series node from the scattering matrices, the electric and magnetic fields are found, respectively. Typically, a simulation of a structure is performed by applying a series of pulses to an electric field node and monitoring the

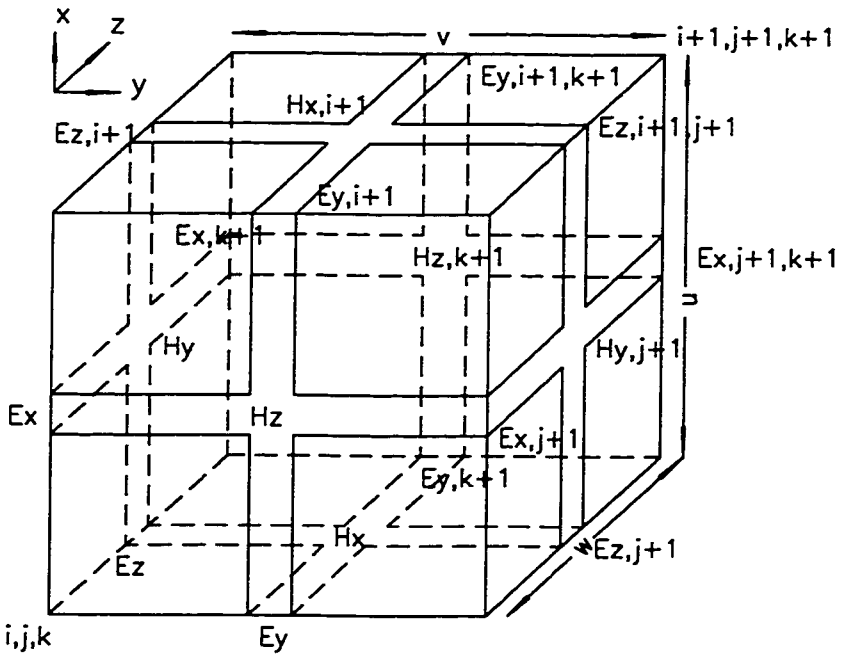

Figure 3.1: Variable mesh TLM cell.

voltages at other shunt nodes. The computer program simulates wave propagation by performing scattering operations at all the shunt nodes at one time step and at all the series nodes half a time step later.

The variable-mesh TLM method uses the same interconnection of lines as the uniform-mesh TLM method. Cells represented by six nodes can have sides of different length and are stacked together to fill the entire space being simulated. Fig. 3.2 is an example of several variable-mesh cells filling a region of space.

The details of a series node and a shunt node are sketched in Fig. 3.3 and Fig. 3.4. The algorithm of the three-dimensional variable-mesh FD-TLM method has been discussed in [17, 18, 55] and will not be repeated in this thesis.

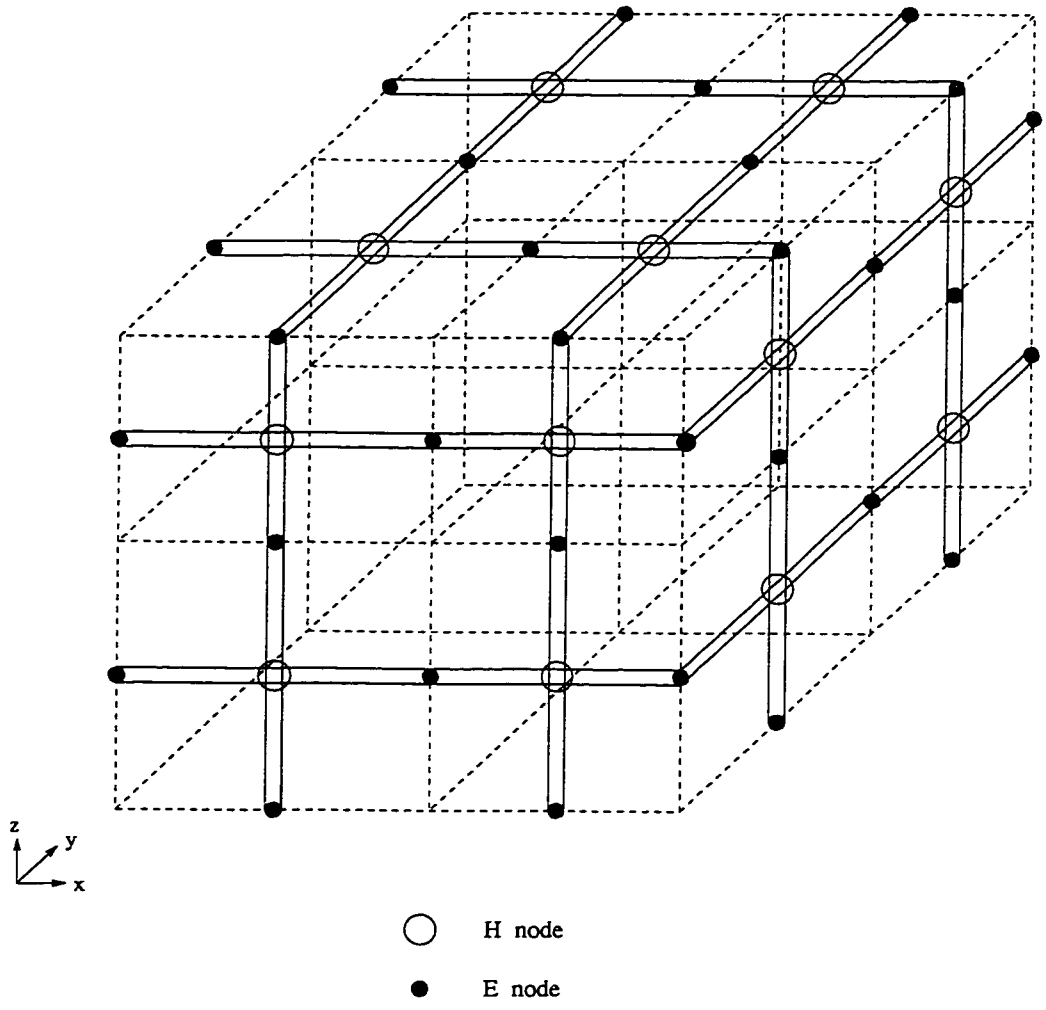

Figure 3.2: An example of variable-mesh TLM cells stacked together. H nodes (H_x, H_y, H_z) and E nodes (E_x, E_y, E_z) are interconnected to fill with the entire computation domain.

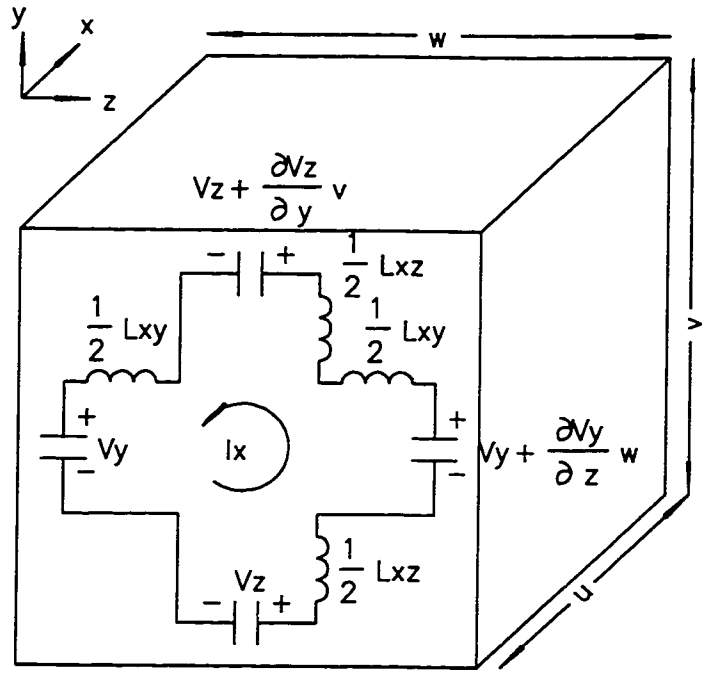

Figure 3.3: Equivalent circuit for the H_x series node

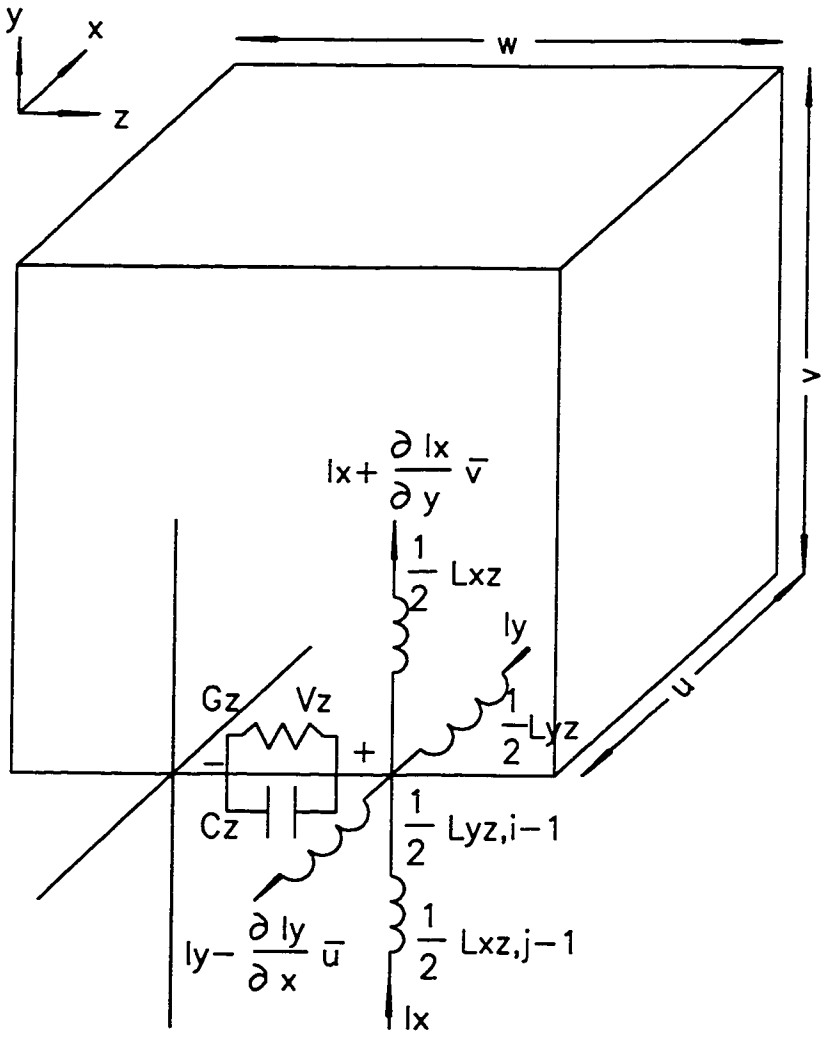

Figure 3.4: Equivalent circuit for the E_z shunt node

3.3 Implementation of the Distributed Active Region of Optical Gain in the FD-TLM Method

The FD-TLM method has been successfully used to model lumped nonlinear devices [17] and the negative conductivity region in the two-dimensional problem [25]. It has been proved to be a powerful method to simulate systems with active regions. But this numerical method has not been applied to the system with a three-dimensional distributed active region of optical gain medium. In this chapter, a distributed active region of optical gain is implemented in three dimensions using FD-TLM method based on the one-dimensional transmission line microcavity model.

To simplify the discrete time-domain three-dimensional modeling of the microcavity, the optical gain medium is assumed to fill with the microcavity [2, 3]. From the wave point of view, the effect of the gain medium is to amplify electromagnetic travelling waves. In steady-state operation of the laser, optical gain is a constant in terms of a fixed injection current.

Since the internal loss of the microcavity is not taken into account, the loss stubs G_x, G_y, and G_z (Fig. 3.4) on the shunt nodes in the active region should serve as gain stubs to include the optical gain into the FD-TLM method by considering the gain as the negative loss.

Eq. (2.37) in the one-dimensional microcavity model gives

$$G_0 = -\frac{\Gamma g}{Z_c} \tag{3.1}$$

where optical gain and characteristic impedance have been related to the shunt conductance per unit length.

Considering the E_z shunt node shown in Fig. 3.4, the gain stub G_z in Fig. 3.4 must be equal to the sum of the gain from four connecting transmission line segments,

$$\begin{aligned} G_z(i,j,k) &= \frac{-\Gamma g}{z_0 Z_{xzn}(i,j-1,k)} \frac{v(j-1)}{2} + \frac{-\Gamma g}{z_0 Z_{xzn}(i,j,k)} \frac{v(j)}{2} \\ &\quad + \frac{-\Gamma g}{z_0 Z_{yzn}(i-1,j,k)} \frac{u(i-1)}{2} + \frac{-\Gamma g}{z_0 Z_{yzn}(i,j,k)} \frac{u(i)}{2} \\ &= \frac{-\Gamma g}{2z_0} [\frac{v(j-1)}{Z_{xzn}(i,j-1,k)} + \frac{v(j)}{Z_{xzn}(i,j,k)} \\ &\quad + \frac{u(i-1)}{Z_{yzn}(i-1,j,k)} + \frac{u(i)}{Z_{yzn}(i,j,k)}] \end{aligned} \tag{3.2}$$

where the concept of the normalized impedance $Z_n = Z_c/z_0$ in FD-TLM method is applied. Because the gain medium is isotropic, the same derivation is directly used with the E_x and E_y shunt nodes,

$$\begin{aligned} G_x(i,j,k) &= \frac{-\Gamma g}{2z_0} [\frac{w(k-1)}{Z_{yxn}(i,j,k-1)} + \frac{w(k)}{Z_{yxn}(i,j,k)} \\ &\quad + \frac{v(j-1)}{Z_{zxn}(i,j-1,k)} + \frac{v(j)}{Z_{zxn}(i,j,k)}] \end{aligned} \tag{3.3}$$

$$\begin{aligned} G_y(i,j,k) &= \frac{-\Gamma g}{2z_0} [\frac{u(i-1)}{Z_{zyn}(i-1,j,k)} + \frac{u(i)}{Z_{zyn}(i,j,k)} \\ &\quad + \frac{w(k-1)}{Z_{xyn}(i,j,k-1)} + \frac{w(k)}{Z_{xyn}(i,j,k)}] \end{aligned} \tag{3.4}$$

where $z_0 = \sqrt{\mu_0/\epsilon_0}$ is the impedance of free space, Z_{xzn}, Z_{yzn}, Z_{yxn}, Z_{zxn}, Z_{zyn}, and Z_{xyn} are the normalized transmission line impedances, and u, v, and w are the mesh sizes in the computational network [17].

By neglecting the cavity internal loss, the net change of the amplitude of the electric field after one round trip along the cavity length must be equal to unity at the laser steady-state near threshold, which leads to the condition [6]

$$(R_1 R_2)^{1/2} \exp(\Gamma g L_c) = 1 \tag{3.5}$$

where R_1 and R_2 are the top and bottom mirror reflectivity and equal to R_m when the cavity is symmetric. Then (3.5) is written as

$$R_m \exp(\Gamma g L_c) = 1 \tag{3.6}$$

$$\Gamma g = \frac{1}{L_c} \ln\left(\frac{1}{R_m}\right) \tag{3.7}$$

Eq. (3.7) can be used in (3.2), (3.3), (3.4) to calculate the gain according to cavity properties for all the shunt nodes inside the active region.

When a shunt node is on the boundary between active region and passive region, the four connecting transmission line segments must be considered separately. Each segment inside the active region should be counted and each segment outside of the active region should not be counted into the gain stub. Each segment on the boundary plane should be counted into the gain stub by half.

The distributed negative conductance region in the cavity model serves as a travelling wave amplifier. The existence of negative conductances may cause the

numerical simulation unstable. Fortunately, the gain and loss in the steady state of lasers compensate each other and the numerical stability is maintained in the simulation.

3.4 Effective Mirror and Simplified Microcavity Model

Gain stubs in the FD-TLM discrete time-domain full wave model of microcavities have been derived, which makes the full wave electromagnetic simulation of the microcavity realizable. However, the structure of the microcavity is complex and our computer resource is limited so that it is necessary to build up a simplified model for simulation. Since the major concern is the three dimensional electromagnetic simulation of the distributed active region in the microcavity, the high reflectivity Bragg mirror which usually consists of about 20 pairs of semiconductor material layers [2] is simplified for the simulation. Because the mirror has alternating index layers, the simulation of the mirror takes a very large computer memory and very long computational time. The idea to simplify the mirror is to use a pair of quarter-wave layers with a large index difference between them to maintain the same reflectivity at the lasing wavelength as the quarter-wave stacks.

For normal incidence, the reflectivity of the quarter-wave stacks is given by

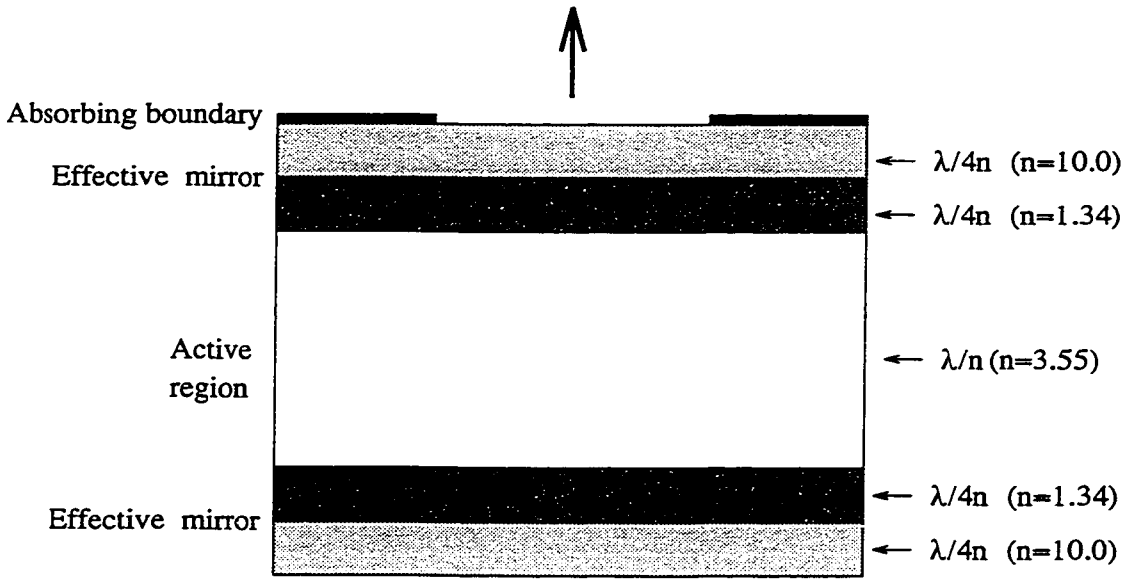

Figure 3.5: Cross-sectional view of the simplified microcavity model for simulation. n is the refractive index of the material.

[6, 26, 27]

$$R_m = \left[\frac{1 - \frac{n_l}{n_1} \left(\frac{n_2}{n_3} \right)^{2N}}{1 + \frac{n_l}{n_1} \left(\frac{n_2}{n_3} \right)^{2N}} \right]^2 \tag{3.8}$$

where n_2 and n_3 are the refractive indices of the alternating layer pairs, n_l and n_1 are the refractive indices of the medium on the transmitted and incident sides of the mirror, and N is the number of pairs. For a given N, R_m is larger if the ratio n_2/n_3 is smaller. For the desired reflectivity of $R_m = 0.98$, $n_2 = 1.34$ and $n_3 = 10.0$ are selected in terms of $n_1 = 3.55$ and $n_l = 1$. The simplified microcavity model for simulation is shown in Fig. 3.5.

3.5 Numerical Simulation

The simulation parameters are given as follows. The length of the cavity is $\lambda_g = \lambda/n$ [2], where $\lambda = 0.85\mu m$ for AlGaAs-GaAs laser and the index of the active region is 3.55 for GaAs material. The lateral dimensions of the cavity are selected as $10 \times 10\mu m$. The diameter of the radiation aperture is $4\mu m$ where the absorbing boundary condition is applied at the top of the microcavity to form the aperture. The variable mesh of the FD-TLM method makes the discretization of the microcavity easier by using less computer resource.

At the beginning of the simulation, a plane sinusoidal wave is applied to the microcavity as the excitation of the simulation. Then the excitation is removed and the traveling wave propagates along the cavity axis back and forth through the reflection of top and bottom mirrors and the amplification of the gain medium. The amount of the amplification compensates for the amount of the mirror loss in each round trip. The standing wave property of the steady-state operation of surface emitting lasers can be observed through the simulation of the microcavity.

The spatial-intensity distribution of the emitted light near the laser facet is known as the near field intensity distribution [6, 28]. From the numerical simulation, the optical field near the facet can be directly sampled on the top of the laser using

$$|E| = \sqrt{E_x^2 + E_y^2 + E_z^2} \tag{3.9}$$

the near field intensity distribution takes the squared value of the optical field dis-

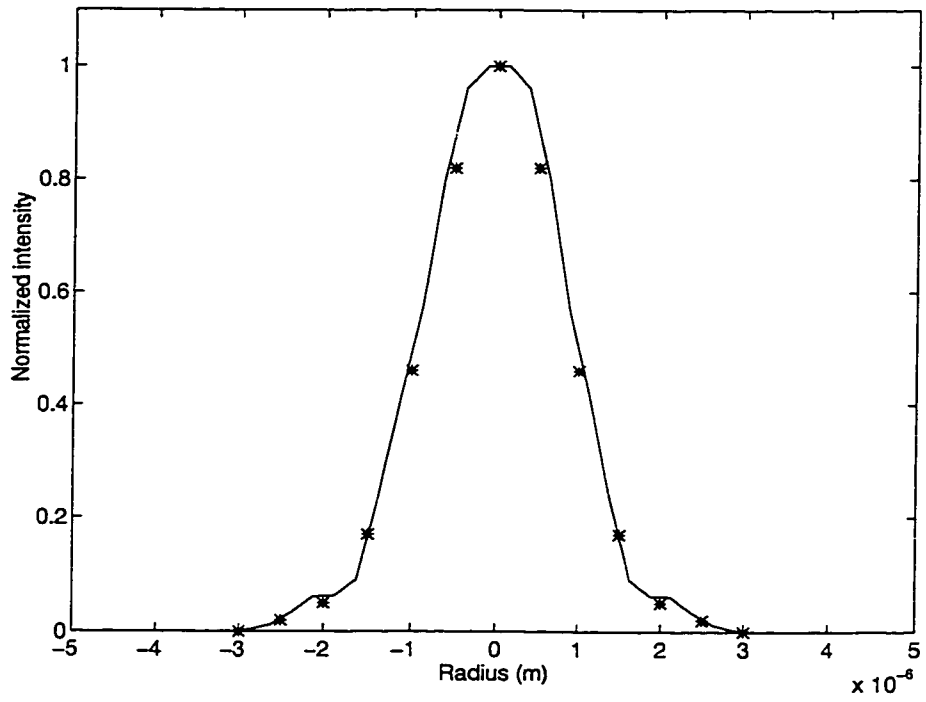

Figure 3.6: Near-field intensity pattern of $4\mu m$ diameter VCSEL. — FD-TLM simulation, * — results from the beam propagation model.

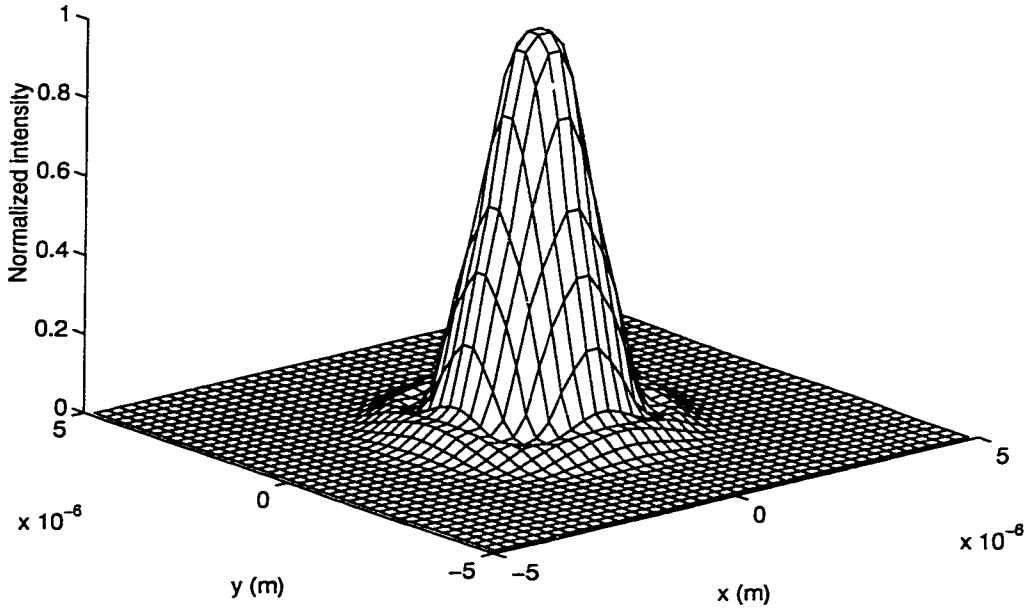

Figure 3.7: Three-dimensional near-field intensity pattern of $4\mu m$ diameter VCSEL.

tribution [28]

$$I = |E|^2 \tag{3.10}$$

Fig. 3.6 shows the near-field intensity pattern of $4\mu m$ diameter VCSEL. FD-TLM simulation results match the results of the beam propagation model in [16]. The full-width at half-maximum (FWHM) of the intensity profile is measured approximately $2\mu m$. The three dimensional near-field intensity pattern is drawn in Fig. 3.7.

As the optical component located nearest to the diode usually lies in the far field, the far-field intensity pattern is important in determining the coupling efficiency between a semiconductor laser and a fiber. The angular intensity distri-

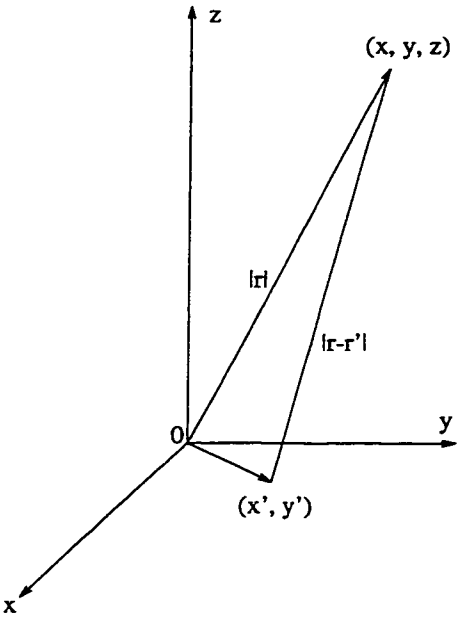

Figure 3.8: The coordinate system for the far-field solution.

bution far from the laser facet is known as the far field intensity distribution [6, 28]. Mathematically, the far field is obtained by taking the Fourier transform of the near field as [28]

$$E(x,y,z) = -\frac{jz}{\lambda r}\frac{\exp(jkr)}{r}\int_{-\infty}^{\infty}\int_{-\infty}^{\infty} e(x',y')\,\exp\left[-\frac{jk}{r}(xx'+yy')\right]dx'dy' \quad (3.11)$$

where $r = \sqrt{x^2+y^2+z^2}$. The coordinate system for the far-field solution is shown in Fig. 3.8. Then, the far-field intensity distribution is obtained by using Eq.(3.10) The far-field intensity pattern of $4\mu m$ diameter VCSEL is shown in Fig. 3.9. The simulation results in this chapter are in a good agreement with the results of the beam propagation model in [16]. The practically interested FWHM of the intensity profile is measured approximately 12 degrees. Three-dimensional far-field intensity pattern is drawn in Fig. 3.10.

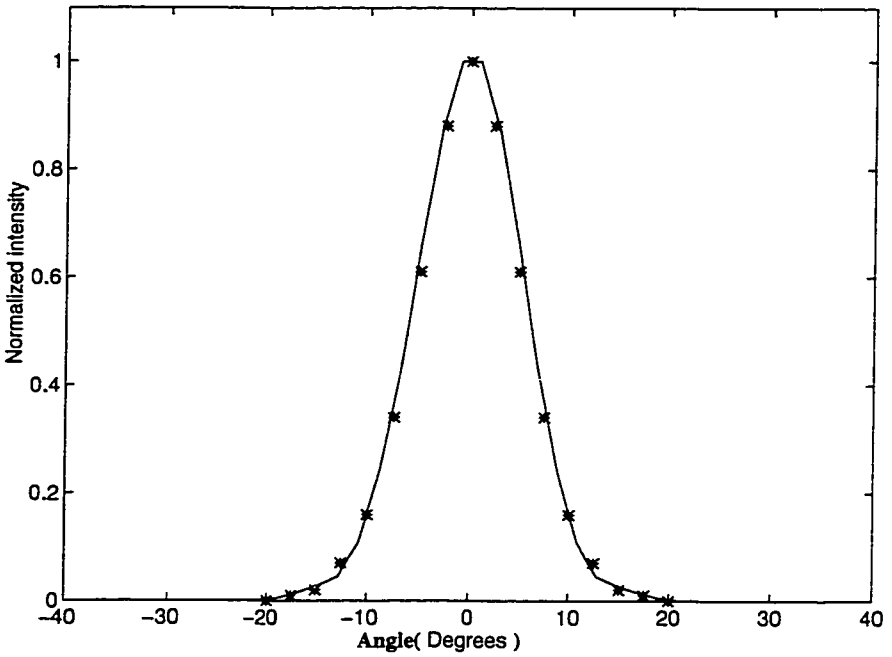

Figure 3.9: Far-field intensity pattern of $4\mu m$ diameter VCSEL. — FD-TLM simulation, * — results from the beam propagation model.

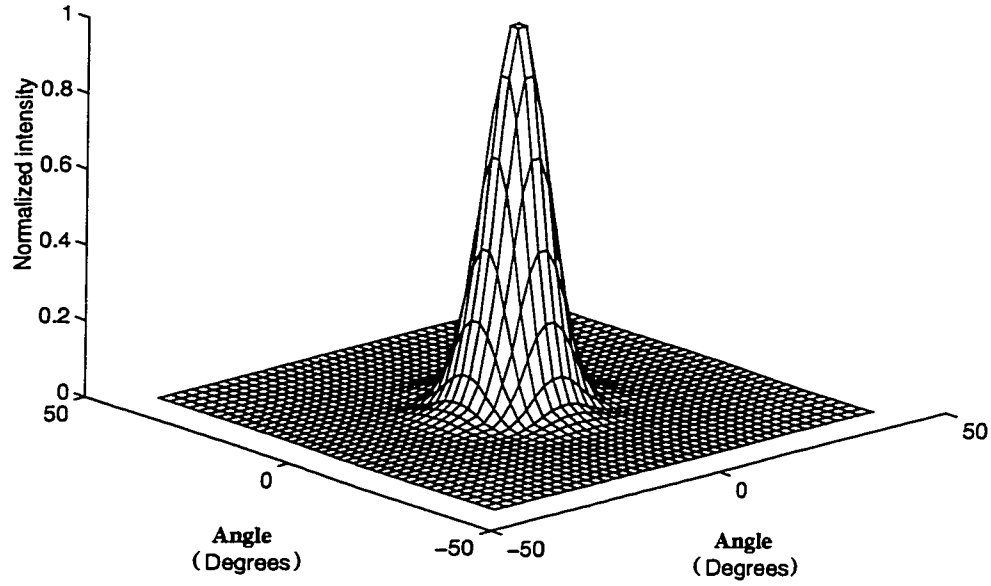

Figure 3.10: Three-dimensional far-field intensity pattern of $4\mu m$ diameter VCSEL.

3.6 Concluding Remarks

A three-dimensional discrete time-domain electromagnetic modeling method for microcavities is introduced in this chapter. FD-TLM method is modified to become capable of including the distributed optical gain region into the full wave simulation. The simplified microcavity model has been proved to be effective by the simulation conducted in this chapter and can be directly used in the full-wave modeling of optoelectronic integrated systems.

Chapter 4

Dynamic Equivalent Circuit Model for Vertical Cavity Surface Emitting Lasers

A new dynamic equivalent circuit model for vertical cavity surface emitting lasers (VCSEL) is developed to add to the family of laser equivalent circuit models. To describe the laser dynamics, the microcavity model developed in Chapter 2 is coupled to the rate equations. A nonlinear resistance is used to represent the optical gain in the cavity. A spontaneous emission noise source is added to the equivalent circuit model to simulate the noise process throughout the laser operation, which is favored in system modeling. Also, the step response and modulation response are addressed in this chapter. Simulation results are compared with the direct rate

equation solutions and show that the model is accurate and effective for providing the dynamic response of the optical field including frequency chirp, carrier and photon populations, and output power. The model enables the laser and its electrical driving circuit to be directly connected (Electronic driving current is directly applied to the injection current of lasers) and analyzed in a unified manner and can be easily implemented on general-purpose nonlinear circuit modeling software.

4.1 Introduction

Maxwell's equations have been used to explore the physics of devices having substantial commercial applications, especially ultrahigh-speed electronic, electrooptic, and all-optical devices, which are useful in advanced digital signal processors, computers [29], and fiber communication systems. These investigations are being conducted by combining the physics of the electromagnetic field and energy transport with the physics of electronic charge transport and volume-averaged quantum effects [30, 31, 32].

The operation of a semiconductor laser provides an extremely complex modeling problem. A complete model would include the solution of the optical field and carrier diffusion equations in a three-dimensional dielectric waveguide whose dimensions may be carrier dependent and the dielectric's refractive index would include real and imaginary components, both being functions of wavelength and carrier density. The limitation of computing power has made the above scenario impractical

to realize [8, 33].

However, many partially simplified laser models are available, such as traveling wave model [9], beam propagation model [16], transmission line laser model [8], and equivalent circuit models [7, 34, 35], because it is necessary to predict the dynamic behavior for applications using modulation, such as optical communication and optical signal processing. There is a need to develop a dynamic equivalent circuit model for surface emitting lasers. In the dynamic equivalent circuit model developed in this chapter, the microcavity model is used to model the optical wave propagation in the cavity, and the standing wave effect is taken into account because the spatial variation of the standing wave within the rather short cavity is substantial. A nonlinear resistor is developed to model the optical gain in the cavity and a spontaneous noise source is applied in the circuit to simulate the noise process throughout the laser operation. The rate equations are discretized in space to describe the laser dynamics and the frequency chirping is obtained from the nonlinear dynamics of the cavity resonant frequency.

There are several advantages with the dynamic equivalent circuit model.

1. The modeling of the optical field is retained in this approach. By retaining the optical field, fundamental quantities — the optical electric field (voltage) and magnetic field (current) in space and time — rather than a power envelope function is solved in the model, which allows the optical field, intensity, noise, phase, chirp, and frequency information to be extracted in one simulation.

2. Time domain models can save computational time and give computational

simplicity by automatically calculating the superposition of all the modes together and separating the modes only after Fourier analysis.

3. The cavity model is included in the dynamic equivalent circuit model which allows novel structures to be investigated.

4. Spatial inhomogeneities are included in the model without adding extra rate equations.

4.2 Dynamic Equivalent Circuit Model

In this section, the development of a new dynamic equivalent circuit model for the VCSEL is addressed by coupling the microcavity model to the rate equations. Fig. 4.1 shows the analytical model of the surface emitting laser. In this model, a GaAs bulk active region and two DBR mirrors are assumed, which closely resembles actual devices [5, 36, 37].

The rate equations for semiconductor lasers have been used extensively to investigate the dynamic characteristics of lasers. The single mode rate equations for the dynamic equivalent circuit model can be written as [6]

$$\frac{dP}{dt} = (G - \gamma_p)P + R_{sp} \tag{4.1a}$$

$$\frac{dN}{dt} = \frac{i_{inj}}{q} - \gamma_e N - GP \tag{4.1b}$$

where P is the photon number and N is the carrier number in the active region, i_{inj}

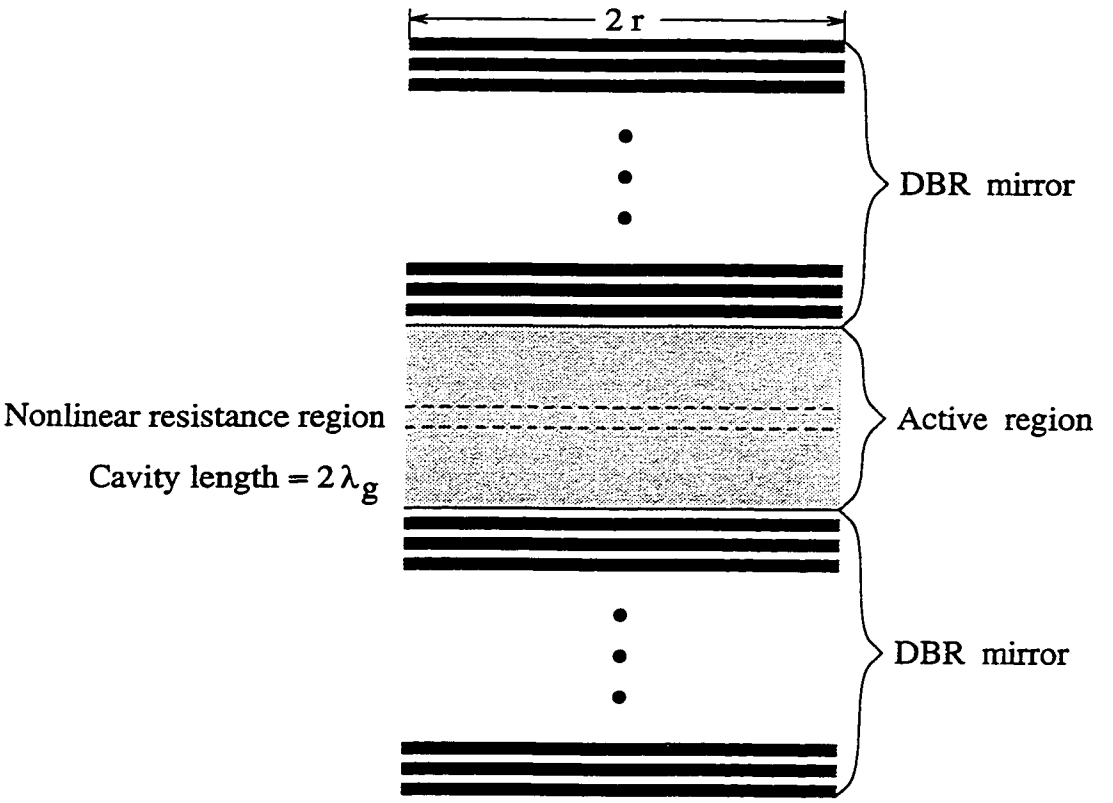

Figure 4.1: Schematic cross section of the analytical model of surface emitting lasers. The DBR mirror is quarter wave stacks, the active region is two wavelengths long in the material, and the radius of the laser aperture is r.

is the injection current and q is the electron charge.

$$\gamma_e = \tau_e^{-1} \tag{4.2}$$

is the carrier recombination rate that can be used to define the spontaneous carrier lifetime τ_e [6].

$$\gamma_p = v_g(\alpha_m + \alpha_{int}) = \tau_p^{-1} \tag{4.3}$$

is the photon decay rate that can be used to define the photon lifetime τ_p. The mirror loss α_m is given as [6]

$$\alpha_m = \frac{1}{L_c} \ln\left(\frac{1}{R_m}\right) \tag{4.4}$$

where L_c is the cavity length and R_m is the mirror reflectivity. The net rate of stimulated emission is [6]

$$G = \Gamma v_g g \tag{4.5}$$

where the linear gain model is give by [6]

$$g = a(N/V_a - n_0) \tag{4.6}$$

where a is the gain coefficient, V_a is the volume of the active region, and n_0 is the carrier density required to achieve transparency. The spontaneous emission rate is given by [6]

$$R_{sp} = \beta_{sp}\eta_{sp}\gamma_e N = \beta_{sp} B N^2 / V_a \tag{4.7}$$

where β_{sp} is the spontaneous emission factor, $\eta_{sp} = \frac{BN}{\gamma_e V_a}$ is the spontaneous quantum efficiency, B is the radiative recombination coefficient.

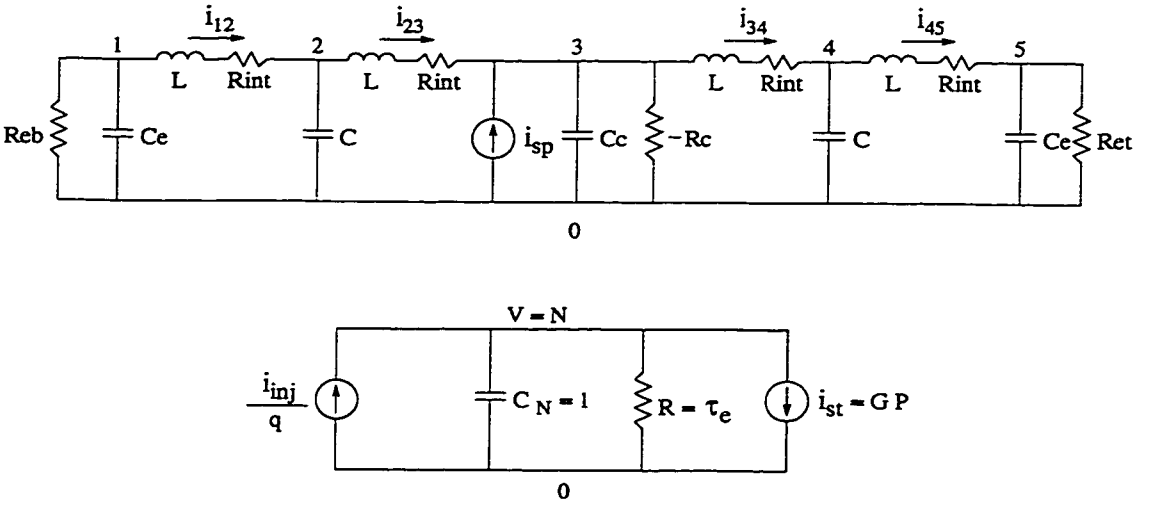

Figure 4.2: The dynamic equivalent circuit model for surface emitting lasers. The upper circuit is the microcavity model and the lower circuit is the carrier rate equation model. Two circuits are coupled each other.

Based on two coupled rate equations and the transmission line microcavity model developed in chapter 2, a dynamic equivalent circuit model for vertical cavity surface emitting lasers is constructed in Fig. 4.2. The carrier rate equation model is constructed in the lower part of the circuit model where the voltage V represents the carrier number N [8]. The capacitor $C_N = 1$ for the convenience of scaling. The circuit equation directly matches the carrier rate equation in (4.1). The photon rate equation in (4.1) is discretized in space and modeled in the form of the microcavity model.

Some modifications to the transmission line microcavity model are made by increasing the length of each transmission line section which results in less circuit nodes in the model for the consideration of both accuracy and computational

efficiency. In this research, each transmission line section is selected as a half wavelength long by considering the circuit simplicity and the model accuracy [8]. The capacitance and inductance of each transmission line section is calculated from the electric and magnetic energy point of view. The cavity length of VCSELs is the integer times of the guided wavelength,

$$L_c = m\lambda_g, \quad m = 1, 2, 3, \cdots \tag{4.8}$$

The spacial distribution of the voltage standing wave along the cavity length can be written as

$$v(l) = V_m \cos(\beta l) \tag{4.9}$$

where V_m is the time-independent peak voltage of the standing wave. Due to the standing wave property, each node is at the maximum of the standing wave voltage and at the minimum of the standing wave current.

The time-independent stored electric energy in a small section of transmission line dl is [10]

$$dw_e = \frac{1}{2}v^2(l)C_0 dl = \frac{1}{2}C_0 V_m^2 \cos^2(\beta l)dl \tag{4.10}$$

The time-independent stored electric energy in a $\lambda_g/2$ transmission line section is

$$\begin{aligned} W_e &= \int_0^{\frac{\lambda_g}{2}} dw_e \\ &= \int_0^{\frac{\lambda_g}{2}} \frac{1}{2}C_0 V_m^2 \cos^2(\beta l)dl \\ &= \frac{C_0 V_m^2 \lambda_g}{8} \end{aligned} \tag{4.11}$$

which is equal to the time-independent stored electric energy in the capacitance C of the $\lambda_g/2$ transmission line section

$$W_e = \frac{1}{2}CV_m^2 \tag{4.12}$$

From above two equations, the capacitance for each $\lambda_g/2$ transmission line section is obtained as

$$C = C_0\frac{\lambda_g}{4}. \tag{4.13}$$

Then, the capacitance in the middle of the cavity $C_c = C$ and the capacitance at the end of the cavity $C_e = C/2$.

The time-independent stored magnetic energy in a small section of the transmission line dl is

$$dw_m = \frac{1}{2}i^2(l)L_0dl = \frac{1}{2}L_0I_m^2\sin^2(\beta l)dl \tag{4.14}$$

where I_m is the time-independent peak current of the standing wave. The time-independent stored magnetic energy in a $\lambda_g/2$ transmission line section is

$$\begin{aligned} W_m &= \int_0^{\frac{\lambda_g}{2}} dw_m \\ &= \int_0^{\frac{\lambda_g}{2}} \frac{1}{2}L_0I_m^2\sin^2(\beta l)dl \\ &= \frac{L_0I_m^2\lambda_g}{8} \end{aligned} \tag{4.15}$$

which is equal to the time-independent stored magnetic energy in the inductance L of the $\lambda_g/2$ transmission line section

$$W_m = \frac{1}{2}LI^2 = \frac{1}{4}LI_m^2 \tag{4.16}$$

where the time-independent and space-average current I flowing through the inductance L of the $\lambda_g/2$ transmission line section is assumed to be the RMS value of the current standing wave. From above two equations, the inductance for each $\lambda_g/2$ transmission line section is obtained as

$$L = L_0 \frac{\lambda_g}{2}. \tag{4.17}$$

Instead of using the lossless transmission line in the microcavity model developed in Chapter 2, a lossy transmission line is used to include the cavity internal loss in the dynamic model. The series resistance R_{int} for each $\lambda_g/2$ transmission line section is used to represent internal loss α_{int}. From (2.37)

$$R_0 = \alpha_{int} Z_c \tag{4.18}$$

The resistance R_{int} for each $\lambda_g/2$ transmission line section can be calculated by using the method in the derivation of the inductance L,

$$R_{int} = R_0 \lambda_g/2 = \alpha_{int} Z_c \lambda_g/2. \tag{4.19}$$

Although the cavity internal loss is represented by R_{int} and is added to the circuit model, it is negligible compared with the inductive reactance $2\pi f_c L$ where f_c is optical frequency, the characteristic impedance of the transmission line can still be expressed by (2.5).

The resistances R_{eb}, R_{et}, and R_c keep the same expressions as those in Chapter 2. Resistances R_{eb} and R_{et} for Bragg mirrors have been given in (2.11). The

nonlinear resistance R_c represents the total gain of the active region for convenience. From (2.43) and (4.6),

$$R_c = \frac{2Z_c}{L_c \Gamma g} = \frac{2Z_c}{L_c \Gamma a(N/V_a - n_0)} \tag{4.20}$$

where $L_c = 2\lambda_g$ and $\Gamma = 1$ are assumed.

According to Kirchhoff voltage and current laws, the circuit equations for the dynamic equivalent circuit model in Fig. 4.2 are written as

$$\begin{aligned}
\frac{dv_{10}}{dt} &= -\frac{v_{10}}{C_e R_{eb}} - \frac{i_{12}}{C_e} \\
\frac{dv_{20}}{dt} &= \frac{i_{12}}{C} - \frac{i_{23}}{C} \\
\frac{dv_{30}}{dt} &= \frac{v_{30}}{C_c R_c} + \frac{i_{23}}{C_c} - \frac{i_{34}}{C_c} + \frac{i_{sp}}{C_c} \\
\frac{dv_{40}}{dt} &= \frac{i_{34}}{C} - \frac{i_{45}}{C} \\
\frac{dv_{50}}{dt} &= -\frac{v_{50}}{C_e R_{et}} + \frac{i_{45}}{C_e} \\
\frac{di_{12}}{dt} &= \frac{v_{10}}{L} - \frac{v_{20}}{L} - \frac{i_{12} R_{int}}{L} \\
\frac{di_{23}}{dt} &= \frac{v_{20}}{L} - \frac{v_{30}}{L} - \frac{i_{23} R_{int}}{L} \\
\frac{di_{34}}{dt} &= \frac{v_{30}}{L} - \frac{v_{40}}{L} - \frac{i_{34} R_{int}}{L} \\
\frac{di_{45}}{dt} &= \frac{v_{40}}{L} - \frac{v_{50}}{L} - \frac{i_{45} R_{int}}{L} \\
\frac{dN}{dt} &= \frac{i_{inj}}{q} - \gamma_e N - GP
\end{aligned} \tag{4.21}$$

In above equations, the photon number P and the spontaneous emission noise source i_{sp} have not been defined yet and will be discussed in the following two sections.

4.3 Relationship between photon number and standing wave in the cavity

The photon rate equation in (4.1) has been discretized in terms of electromagnetic wave theory. For the coupling of the two subcircuits, we must find the relationship between the photon number and the standing wave in the cavity which is necessary to solve the circuit equations. The relationship is derived in this section.

By neglecting the wave attenuation caused by the cavity internal loss, the standing wave on the transmission line can be written as [10]

$$\mathbf{V} = \mathbf{V}_1 e^{j\beta z} + \mathbf{V}_2 e^{-j\beta z} \tag{4.22}$$

where the first term represents the incident wave onto the mirror, the second term represents the reflected wave from the mirror, and $\mathbf{V}$ is the phasor notation of the wave. The amplitude of the standing wave can be written as

$$\begin{aligned} |\mathbf{V}| &= |\mathbf{V}_1 e^{j\beta z} + \mathbf{V}_2 e^{-j\beta z}| \\ &= |V_1 e^{j(\beta z+\phi_1)} + V_2 e^{-j(\beta z-\phi_2)}| \\ &= \sqrt{V_1^2 + V_2^2 + 2V_1 V_2 \cos(\theta_0 - 2\beta z)} \end{aligned} \tag{4.23}$$

where V_1 is the amplitude of the incident wave, V_2 is the amplitude of the reflected wave, ϕ_1 is the initial phase of the incident wave, ϕ_2 is the initial phase of the reflected wave, $\theta_0 = \phi_2 - \phi_1$ is the phase difference between incident and reflected

waves. The reflection coefficient at the end of the cavity

$$\Gamma_m = \sqrt{R_m} e^{j\theta_0} \tag{4.24}$$

In the microcavity, we have

$$\frac{V_2}{V_1} = \sqrt{R_m}, \qquad \theta_0 \approx 0 \tag{4.25}$$

Substituting (4.25) into (4.23) and considering the locations of the maximum voltage, the maximum value, i.e. amplitude, of the standing wave voltage can be obtained as

$$\begin{aligned} V_{max} &= |\mathbf{V}| \\ &= \sqrt{V_1^2 + V_2^2 + 2V_1V_2} \\ &= \sqrt{V_1^2 + R_m V_1^2 + 2\sqrt{R_m} V_1^2} \\ &= V_1\sqrt{1 + R_m + 2\sqrt{R_m}} \\ &= V_1(1 + \sqrt{R_m}) \end{aligned} \tag{4.26}$$

The incident power from the active region to the mirror is written as [10]

$$P_1 = \frac{|\mathbf{V}_1|^2}{2Z_c} = \frac{V_1^2}{2Z_c} = \frac{V_{max}^2}{2Z_c(1 + \sqrt{R_m})^2} \tag{4.27}$$

The output power from the mirror is [8, 6]

$$\begin{aligned} P_{out} &= P_1(1 - R_m) \\ &= \frac{V_{max}^2(1 - R_m)}{2Z_c(1 + \sqrt{R_m})^2} \\ &= \frac{V_{max}^2(1 - \sqrt{R_m})}{2Z_c(1 + \sqrt{R_m})} \\ &= \frac{1}{2} h f_c v_g \alpha_m P \end{aligned} \tag{4.28}$$

where h is Planck constant. The photon number in the cavity is obtained from the above equation and is written as

$$P = \frac{V_{max}^2(1-\sqrt{R_m})}{Z_c h f_c v_g \alpha_m (1+\sqrt{R_m})} \tag{4.29}$$

(4.29) gives the relationship between the photon number and the amplitude of the standing wave in the cavity and is used in the circuit for carrier rate equation to represent the coupling.

4.4 Spontaneous Emission Noise Source

The spontaneous emission power into the lasing mode is expressed as [8]

$$P_{sp} = R_{sp} h f_c. \tag{4.30}$$

This power may be injected into the model at each node or, to save on computing time, may be localized to one node [8]. For symmetry and simplicity, a current source is assigned in the middle of the cavity to model spontaneous emission noise which is considered as a white noise process with a Gaussian probability distribution [9, 38].

The optical frequency is large compared to the width of the noise spectrum which must at least show a white spectrum up to the relaxation resonant frequency [38]. The spontaneous emission noise source i_{sp} is considered as a narrow band bandpass Gaussian noise source [39]

$$i_{sp}(t) = n_c(t)\cos(2\pi f_c t) - n_s(t)\sin(2\pi f_c t) \tag{4.31}$$

where $n_c(t)$ and $n_s(t)$ are the in-phase and quadrature component of $i_{sp}(t)$ [39], f_c is the optical frequency. $i_{sp}(t)$, $n_c(t)$, and $n_s(t)$ are all zero mean, Gaussian, ergodic, and have the same variance [39]. For the simulation purpose, sampled values of Gaussian white noise are generated using a Gaussian white noise generator [39]. The samples in time domain are uncorrelated and independent [39]. The variance of the samples is derived as follows.

The noise power delivered to Z_c load can be written as [39]

$$P_{Z_c} = E\{(\frac{i_{sp}(t)}{2})^2 Z_c\} = \frac{Z_c}{4} E\{i_{sp}^2(t)\} \tag{4.32}$$

where E denotes the expectation of the random process. Since $i_{sp}(t)$ is a Gaussian noise, $E\{i_{sp}^2(t)\} = \sigma^2$, where σ^2 is the variance of the Gaussian sequence $i_{sp}(t)$, i.e., $n_c(t)$ and $n_s(t)$ have the same variance of σ^2. Then, (4.32) can be written as

$$P_{Z_c} = \frac{Z_c \sigma^2}{4} \tag{4.33}$$

It has been proved that the spontaneous emission fields coupled to the forward and reverse waves have equal amplitude [40]. Equating P_{Z_c} and $P_{sp}/2$, we have

$$\frac{Z_c \sigma^2}{4} = \frac{R_{sp} h f_c}{2} \tag{4.34}$$

then,

$$\sigma^2 = \frac{2 R_{sp} h f_c}{Z_c} \tag{4.35}$$

Therefore, $n_c(t)$ and $n_s(t)$ can be generated by multiplying the output of zero mean, unit variance Gaussian random number generator by σ. The noise period of $n_c(t)$ and $n_s(t)$ is taken as $10ps$ to cover the relaxation oscillation frequency [38].

4.5 Simulation Using Runge-Kutta Method

A numerical approach for solving the nonlinear ordinary differential equations is generally required because of the nonlinear nature of the circuit equations. Eq. (4.21) is a set of ordinary differential equations [41, 42] which take the general form of

$$\frac{dy}{dt} = f(y,t) \tag{4.36}$$

The ordinary differential equations can be solved using Runge-Kutta method [41, 42]. The classical fourth-order Runge-Kutta method is given by

$$y_{n+1} = y_n + \frac{1}{6}(k_0 + 2k_1 + 2k_2 + k_3) \tag{4.37}$$

where

$$\begin{aligned} k_0 &= hf(y_n, t_n), \\ k_1 &= hf(y_n + \frac{k_0}{2}, t_n + \frac{h}{2}), \\ k_2 &= hf(y_n + \frac{k_1}{2}, t_n + \frac{h}{2}), \\ k_3 &= hf(y_n + k_2, t_n + h). \end{aligned}$$

Four evaluations of the function $f(y,t)$ are required for each time step h which changes frequently in the computation by the adaptive step size control algorithm [41, 42]. Runge-kutta method has several advantages. They are numerically stable for a large class of problems. Since only one solution value y_n is needed to calculate y_{n+1}, the method is self-starting. The step size h may be changed at any step in the calculation.

PARAMETER	SYMBOL	VALUE
Optical wavelength	λ	$0.85\mu m$
Refractive index in dielectric medium	n	3.55
Carrier lifetime at threshold	τ_e	$5ns$
Confinement factor	Γ	1
Spontaneous emission factor	β_{sp}	0.02
Radiative recombination coefficient	B	$1 \times 10^{-10} cm^3/s$
Gain coefficient	a	$3.5 \times 10^{-16} cm^2$
Internal loss	α_{int}	$10 cm^{-1}$
Carrier density at transparency	n_0	$0.6 \times 10^{18} cm^{-3}$
Radius of aperture	r	$2\mu m$
Mirror reflectivity	R_m	0.97

Table 4.1: Laser parameters for simulation.

The laser parameters for simulation [3, 6] are listed in Table 4.1.

Several critical and important features with VCSEL are investigated and shown in Fig. 4.3 and Fig. 4.4. Fig. 4.3 shows the output power and turn-on delay versus laser injection current with different mirror reflectivities. The turn-on delay is a characteristic of lasers and indicates that the stimulated emission does not occur until the carrier concentration has reached its threshold value N_{th}. The delay time is determined by the carrier dynamics alone. Fig. 4.4 shows the turn-on delay, carrier number at threshold, and output power versus the cavity length with fixed injection current and different mirror reflectivities.

The step response and modulation response of the carrier population, optical field, frequency chirping, photon population and the output power of the surface emitting laser are simulated in this chapter. To verify the operation of the dynamic

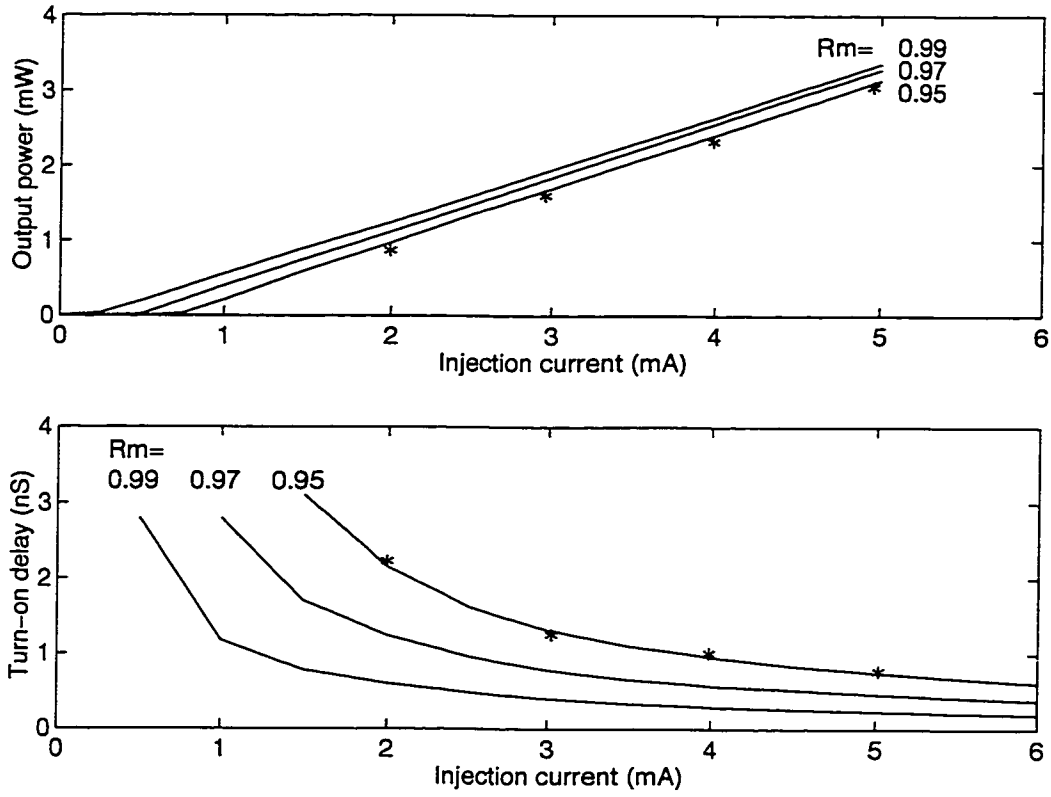

Figure 4.3: Output power and turn-on delay versus injection current. ($L_c = 2\lambda_g$, $\beta = 0.01$.) Solid line — dynamic equivalent circuit model, * — rate equation solution for $R_m = 0.95$.

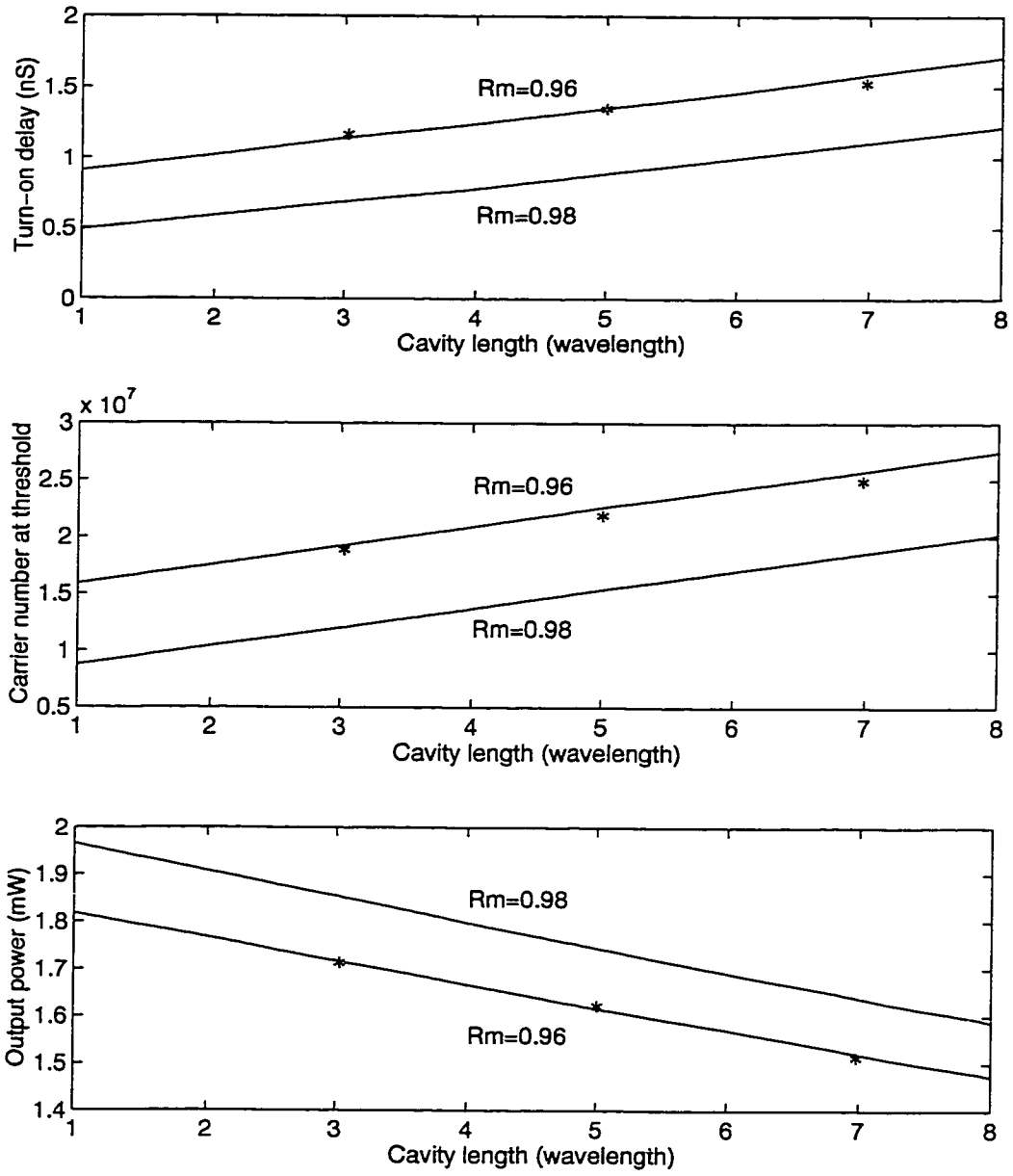

Figure 4.4: Turn-on delay, carrier number at threshold, and output power versus cavity length. ($i_{inj} = 3mA$, $\beta = 0.01$.) Solid line — dynamic equivalent circuit model, * — rate equation solution for $R_m = 0.96$.

equivalent circuit model, the direct solution of rate equations (4.1) is used to compare the results with the dynamic equivalent circuit model.

Fig. 4.5 shows the step response of the surface emitting laser. The injection current is chosen as a step function shown in Fig. 4.5 (a). The detail of the voltage waveform in Fig. 4.5 (d) is a sinusoidal waveform with the optical frequency. The time evolution of the nonlinear resistance R_c is plotted in Fig. 4.5 (c). It is interesting to note that the relaxation oscillation starts when R_c approaches to $R_{et}/2$ or $R_{eb}/2$, *i.e.* the optical gain approaches to the optical loss. The simulation result from the dynamic equivalent circuit model is compared with the rate equation solution.

Several features are noteworthy from the simulation results. The laser current is abruptly increased from its initial value 0 to the final value i_{inj}, which is greater than the threshold value i_{th}, a time period elapses before the steady state is reached. The photon population remains zero for the turn-on delay time t_d, after which it increases rapidly. The important feature of the step response shown in Fig. 4.5 is that the electron and photon populations oscillate before attaining their steady-state values. This damped oscillation, referred to as relaxation oscillation [6], is an intrinsic resonance in which energy stored in the system oscillates back and forth between the electron and photon populations. The natural frequency of the relaxation oscillation is in the gigahertz range and plays an important role in determining device response.

One of the important advantages of semiconductor lasers is that they can be directly modulated for optical communications by modulating the device current. There is always considerable interest in the optical pulse response of directly modulated injection lasers. The pulsed method of driving the laser is suitable for pulse-code modulation schemes [43] which is widely used in fiber communication systems. The laser is generally biased close to threshold so as not to turn off the laser completely during the period of low current level. Fig. 4.6 shows the square wave modulation response of the laser model and exhibits features related to relaxation oscillation. The frequency chirping related with the square wave modulation (Fig. 4.6(c)) is obtained through the Fourier transform of the optical field response which is directly from the simulation of the dynamic equivalent circuit model. Even though the optical pulse is far from being an exact replica of the electrical pulse, it can be used to transmit information over optical fibers.

4.6 Concluding Remarks

The results given in this chapter show that the concept and derivation of the dynamic equivalent circuit model are sound. The model is able to predict the dynamic response of not only carrier and photon populations, but also optical field and frequency chirping of surface emitting lasers. Also the physical process of the laser noise and modulation can be easily modeled using this model [44].

One of the important qualities of numerical models is that they allow results

to be gained faster than from experimental work. Certainly this model allows parameters to be adjusted more quickly than in real devices. Therefore, the model is a useful design tool because it is such a close analogue to the laser device which may be easily modified and enhanced.

The dynamic equivalent circuit model is a powerful computer CAD model to be incorporated into nonlinear circuit modeling software for system modeling since it is easily connected to other electronic driving component models as a load component model in optoelectronic integrated circuits (OEIC) for fiber communication systems.

Fig. 4.5 (a), (b)

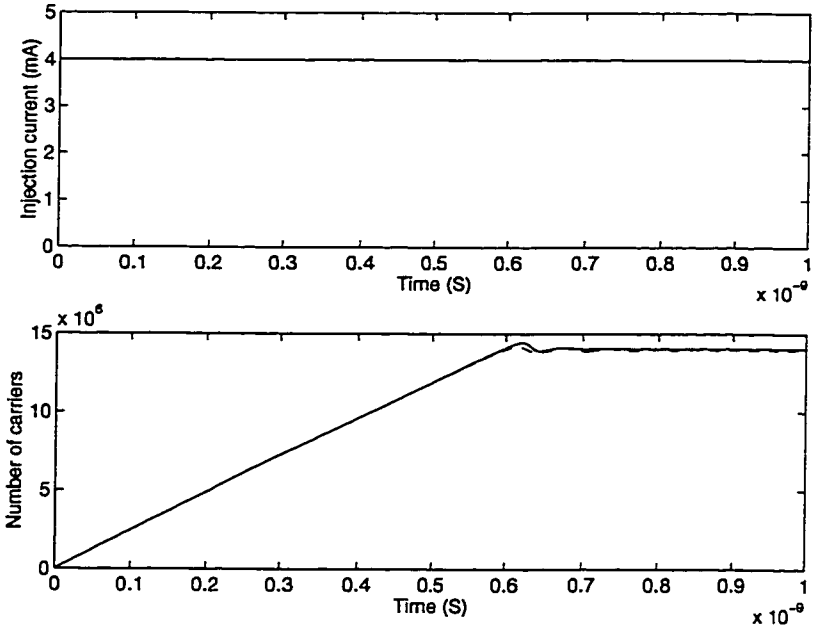

Fig. 4.5 (c)

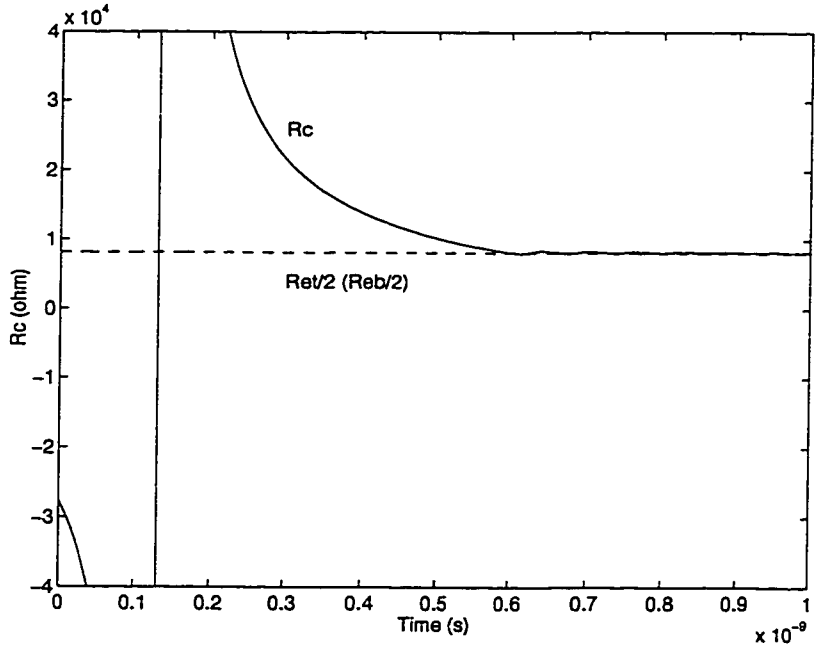

Fig. 4.5 (d)

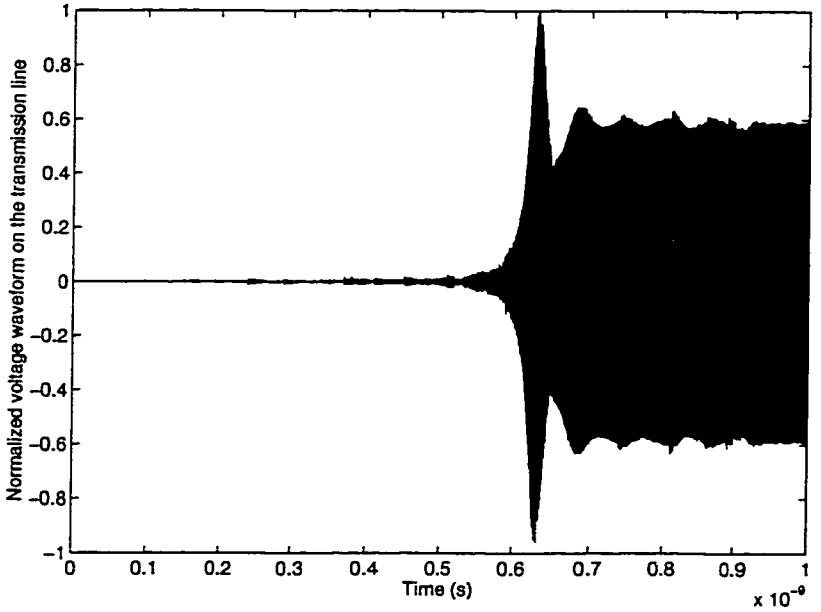

Fig. 4.5 (e)

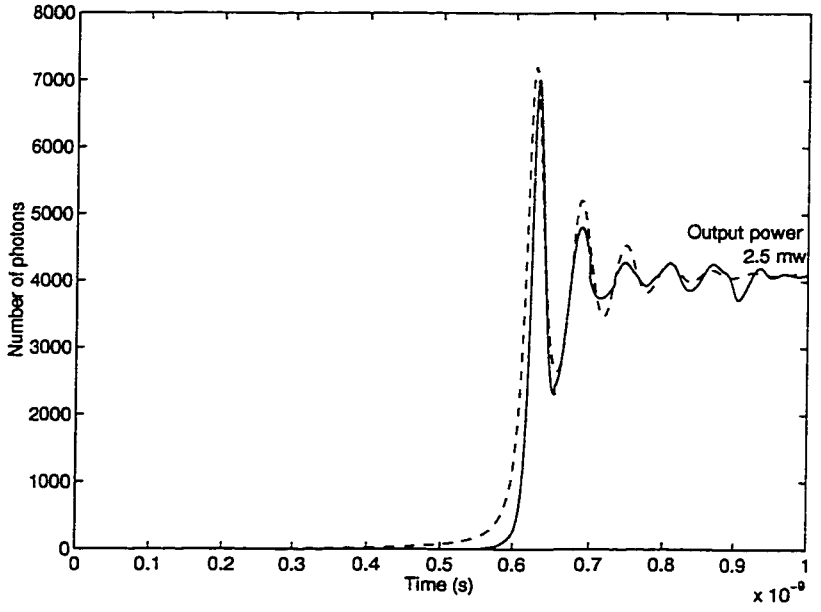

Figure 4.5: Step response of the surface emitting laser. (a) Input step current. (b) Response of carrier population. (c) Time evolution of the nonlinear resistance. (d) Response of the normalized voltage at node 5 on the transmission line. (e) Response of photon population. Solid line — dynamic equivalent circuit model, dashed line — rate equation solution.

Fig. 4.6 (a)

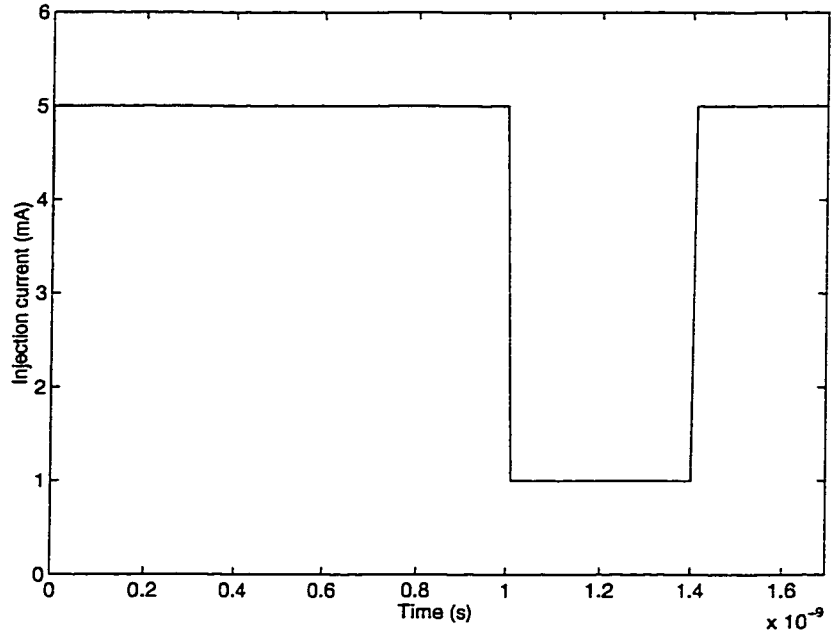

Fig. 4.6 (b)

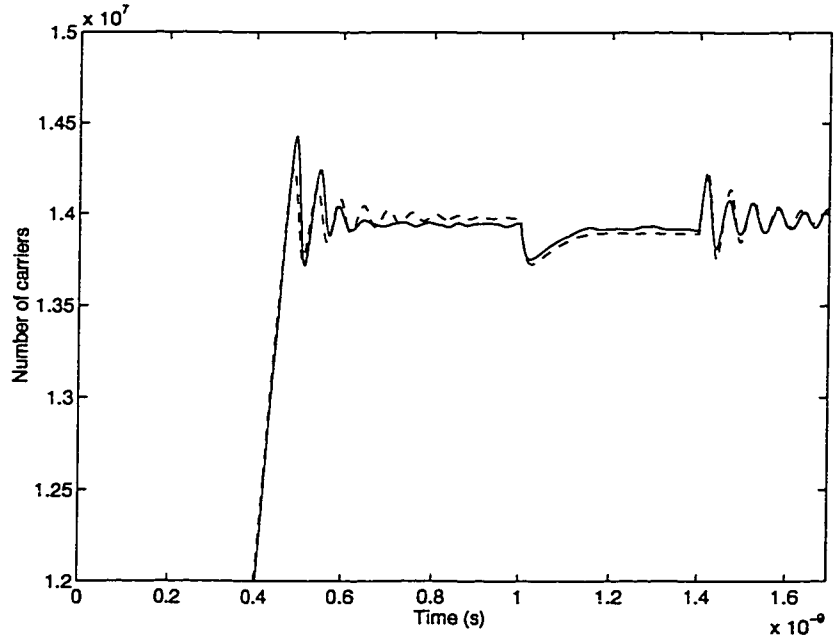

Fig. 4.6 (c)

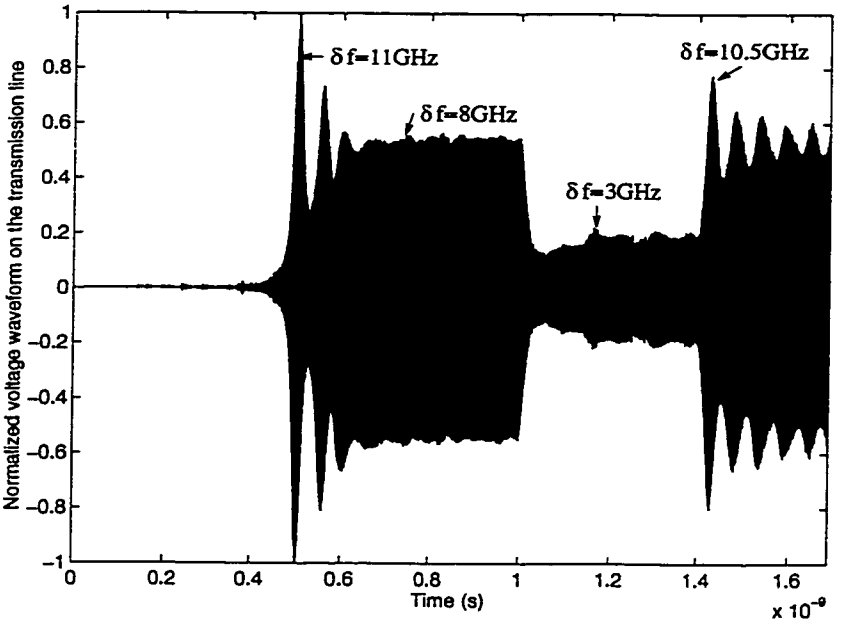

Fig. 4.6 (d)

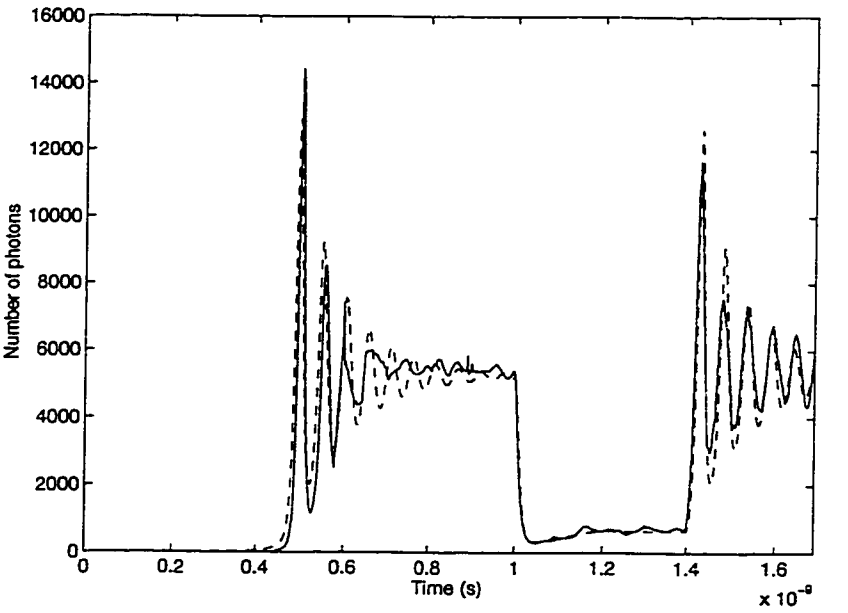

Figure 4.6: Modulation response of the surface emitting laser. (a) Modulation current. (b) Response of carrier population. (c) Response of the normalized voltage at node 5 on the transmission line. Frequency chirp $\delta f = f - f_c$ is indicated at specified points. (d) Response of photon population. Solid line — dynamic equivalent circuit model, dashed line — rate equation solution.

Chapter 5

Full Wave Electromagnetic Modeling of Electro-Optic High-Speed Probes

The foundation of the full wave electromagnetic modeling of external electro-optic (E-O) probes has been laid by X. Wu in [45]. Following his pioneering work, this chapter makes new contributions to the topic which are listed here.

1. Finite-Difference Transmission-Line Matrix method (FD-TLM) is used in the full wave electromagnetic modeling of E-O probes. The method is featured by the variable grid size which is extremely important in the full wave modeling of $LiTaO_3$ E-O probe since the electromagnetic field is mostly confined in the space around the probe tip and the air gap between probe tip and CPW [45] which is

approximately $3\mu m$ with a step size change of $0.1\mu m$ in an automated E-O probing system [46]. Variable grid size for the simulation of the $LiTaO_3$ probe is first reported here (Fig. 5.4 and Fig. 5.5). FD-TLM simulation results are compared to the previous FD-TD simulation results and the consistency between the two methods is demonstrated in Figure 5.7 and 5.12. More accurate results from variable grid size FD-TLM simulation are given in Figure 5.6, 5.8, and 5.13.

2. Full wave simulation for the $LiTaO_3$ E-O probe with high-bandwidth coplanar waveguides with different configurations is addressed in this chapter, which lays the significant foundation of the three-port electrical and optical model for $LiTaO_3$ high-speed electro-optic probe with CPW test structure since the probe is used to sample the signals on different CPW configurations. The scattering parameters with respect to various CPW configurations are first reported here (Figure 5.9, 5.10, and 5.11) for the development of the three-port model in the following chapter.

3. A new system transfer function for the E-O probe with CPW test structure is defined in this chapter and shown in Figure 5.14. The input port of the transfer function is defined at the sampling spot on the CPW rather than the input reference plane defined in [45]. The new definition of the transfer function eliminates the phase difference between the sampling spot and the reference plane so that it directly characterizes the signal waveform on the sampling spot.

5.1 Introduction

The development of very high-speed electro-optic (E-O) sampling systems is now well established. Recently, M. Shinagawa and T. Nagatsuma [46] reported an automatic sampling system based on external E-O sampling for measuring ultra-high-speed integrated circuits (IC). Their workstation controlled sampling system obtained a voltage sensitivity of $1mv/\sqrt{Hz}$ at frequencies up to 70 GHz. Most previous E-O sampling systems were developed for feasibility studies following the pioneering work of J.A. Valdmanis, G.A. Mourou and C.W. Gabel [47].

Conventional, purely electronic measurement instruments such as vector network analyzers, spectrum analyzers and sampling oscilloscopes are not very effective at high frequencies, the major limitation being imposed by the connectors and waveguides needed for signal coupling between the instrument and the device under test.

There are two significant advantages that E-O sampling techniques possess over conventional, purely electronic ones. First, optoelectronic signal generation and measurement bandwidths far exceed those achievable electronically. Second, both the stimulus-generation site and response-measurement planes are physically close to the device under test, so that it is possible to completely eliminate interconnection discontinuities.

External E-O probes do not require that the material being measured exhibit

electro-optic properties while the direct method [48] of probing requires the use of an electro-optic material such as GaAs. Instead, an electro-optic probe tip usually made from $LiTaO_3$ or GaAs is used to sample the electric field being measured. The primary usefulness of $LiTaO_3$ lies in its ability to sample the transverse components of the electric field, a standard requirement of many systems. If the direct electro-optic measurement method is used, the back side of the semiconductor wafer must be polished if an internal reflection system is used, a definite disadvantage in some engineering applications.

There are still several problems associated with external probe tips. The probe tips, while small, are invasive. That is, like all electronic probing systems, they disturb the system being tested. They cause pulse distortion/dispersion, pulse reflections, transmission loss, cross-talk between lines, and have a non-ideal system transfer function [49]. The probes are also difficult to fabricate and position accurately over the devices being tested. Fabrication and positioning problems have been well addressed by M. Shinagawa *et al.* [46].

5.2 Electro-Optic Sampling System

Fig. 5.1 is the optical scheme of an external E-O sampling system which utilizes a $LiTaO_3$ or GaAs probe above the circuit being tested. A crystal probe of an electro-optic material, such as $LiTaO_3$ or GaAs, is placed above the device, so that the electric fields from the device penetrate into the sampling crystal probe. Laser

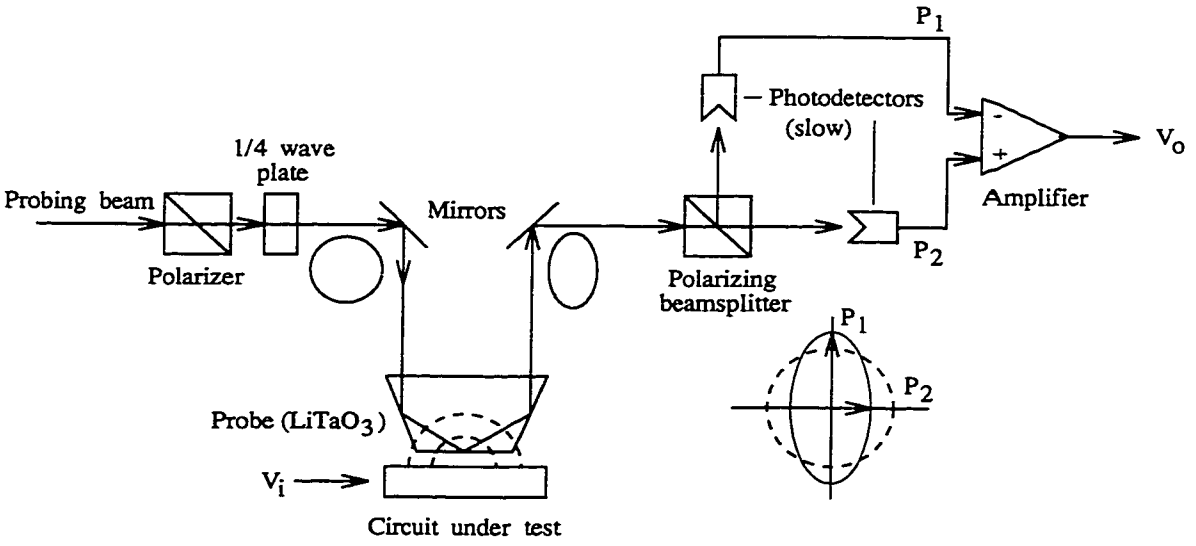

Figure 5.1: Optical scheme of the external E-O sampling. The change in polarization ellipticity of the probing beam can be detected by two low speed photodetectors.

beam pulses, at a sampling repetition rate, probe the electric field induced by the unknown signal as electrical signal pulses propagate across the crystal probe.

The sampling system can be grouped into three sections: the laser system for optical pulse generation, the microwave instrumentation for driving the circuit under test, and the receiver system for data acquisition and signal processing. The laser beam passes through a linear polarizer and a waveplate to get a circularly polarized wave. Then it is focused through the fused silica probe support down to the electro-optic probe tip with a microscope objective to a few-microns spot on the probe facet. The polarization of the probing beam is deformed to ellipsoidly polarized wave due to the birefringence caused by the electric field in the probe tip. The reflected light, *i.e.* the probing beam output, is separated into horizontally and

vertically polarized components by a polarizing beam splitter and detected by two photodiodes connected to a differential amplifier. These signals are then processed by a lock-in amplifier, and a signal averager. By means of a compensator, the modulator is optically biased at its quarter wave point in order to achieve linear E-O response and maximum sensitivity [47].

5.3 Theory of Electro-Optic Sampling

The electro-optic sampling measurement technique, based on the linear electro-optic effect, was first studied by F. Pockels more than 100 years ago in 1893 [50]. In certain types of crystals, the application of an electric field results in a change in polarization of an optical beam which goes through this crystal. This is referred to as the electro-optic effect. Electro-optic sampling employs the E-O effect to measure high speed devices and circuits.

Polarization of a plane wave refers to the orientation of the electric field vector, which may be in a fixed direction, or may change with time. Many crystals, $LiTaO_3$ and GaAs, can affect the polarization of incident light without absorbing or reflecting one of the components. Birefringence of a crystal refers to different refractive indices for separate polarization components of the electric field, one for polarization along and one for polarization perpendicular to the optic axis.

Figure 5.2 shows the basic principle of electro-optic sampling. A circularly

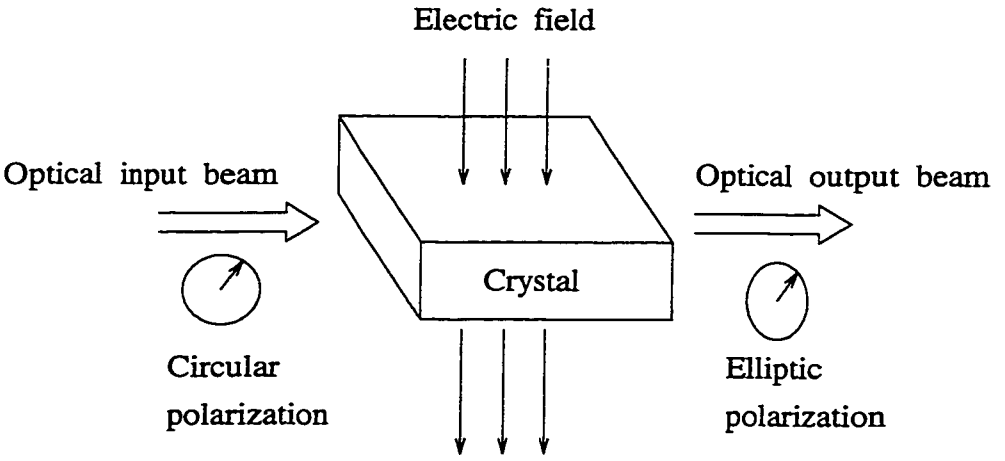

Figure 5.2: Principle of E-O sampling. The polarization of the probing beam is changed after passing through the crystal due to the birefringence which is related to the applied electric field.

polarized optical probing beam is directed through a piece of birefringent crystal where an electric field is imposed. The electric field, that is proportional to the signal measured, induces birefringence in the crystal. The polarization of the probing beam is changed when the beam emerges from the crystal due to its birefringence. This change can be detected by a polarization analyzer and photodetectors. The magnitude of the optical signal produced for a given electric field and probing configuration defines the probe's E-O response. This is the basic principle of E-O sampling for the measurement of high-speed signals.

The birefringent crystals may be either uniaxial ($n_x = n_y, n_z$) or biaxial ($n_x \neq n_y \neq n_z$). $LiTaO_3$, GaAs and most other commonly used E-O crystals are

uniaxial [51]. In isotropic material [51]

$$v_g = \frac{c}{\sqrt{\epsilon_r}} = \frac{c}{n} \tag{5.1}$$

$$\epsilon_r = \frac{\epsilon}{\epsilon_0} \tag{5.2}$$

where ϵ_r is the relative dielectric constant of the material and ϵ is the dielectric constant of the material, ϵ_0 is the permittivity. From above two equations, we have,

$$\frac{\epsilon_0}{\epsilon} = \frac{1}{n^2} \tag{5.3}$$

In an anisotropic crystal, the polarization induced by an electric field and the field itself are not necessarily parallel. The electric displacement vector $\mathbf{D}$ and the electric field $\mathbf{E}$ are consequently related by [51]

$$\begin{bmatrix} D_1 \\ D_2 \\ D_3 \end{bmatrix} = \begin{bmatrix} \epsilon_{11} & \epsilon_{12} & \epsilon_{13} \\ \epsilon_{21} & \epsilon_{22} & \epsilon_{23} \\ \epsilon_{31} & \epsilon_{32} & \epsilon_{33} \end{bmatrix} \begin{bmatrix} E_1 \\ E_2 \\ E_3 \end{bmatrix} \tag{5.4}$$

where $1, 2, 3 = x, y, z$. The 3×3 matrix with elements ϵ_{ij} in (5.4) is called the dielectric tensor.

Similar to (5.3), in anisotropic material we have [51]

$$\frac{\epsilon_0}{\epsilon_{ij}} = \frac{1}{n_{ij}^2} \tag{5.5}$$

which can be expressed as a matrix form

$$\begin{bmatrix} \frac{\epsilon_0}{\epsilon_{11}} & \frac{\epsilon_0}{\epsilon_{12}} & \frac{\epsilon_0}{\epsilon_{13}} \\ \frac{\epsilon_0}{\epsilon_{21}} & \frac{\epsilon_0}{\epsilon_{22}} & \frac{\epsilon_0}{\epsilon_{23}} \\ \frac{\epsilon_0}{\epsilon_{31}} & \frac{\epsilon_0}{\epsilon_{32}} & \frac{\epsilon_0}{\epsilon_{33}} \end{bmatrix} = \begin{bmatrix} \frac{1}{n_{11}^2} & \frac{1}{n_{12}^2} & \frac{1}{n_{13}^2} \\ \frac{1}{n_{21}^2} & \frac{1}{n_{22}^2} & \frac{1}{n_{23}^2} \\ \frac{1}{n_{31}^2} & \frac{1}{n_{32}^2} & \frac{1}{n_{33}^2} \end{bmatrix} \tag{5.6}$$

The 3×3 matrix with elements n_{ij} is called the refractive index tensor of the crystal which is a symmetrical matrix represented by

$$\begin{aligned}
\left(\frac{1}{n^2}\right)_1 &= \frac{1}{n_{11}^2} \\
\left(\frac{1}{n^2}\right)_2 &= \frac{1}{n_{22}^2} \\
\left(\frac{1}{n^2}\right)_3 &= \frac{1}{n_{33}^2} \\
\left(\frac{1}{n^2}\right)_4 &= \frac{1}{n_{23}^2} = \frac{1}{n_{32}^2} \\
\left(\frac{1}{n^2}\right)_5 &= \frac{1}{n_{13}^2} = \frac{1}{n_{31}^2} \\
\left(\frac{1}{n^2}\right)_6 &= \frac{1}{n_{12}^2} = \frac{1}{n_{21}^2}
\end{aligned} \tag{5.7}$$

The propagation characteristics of a light beam in birefringent crystals are fully described by means of the index ellipsoid [51]. Hence, the effect of an electric field on the light wave propagation is expressed most conveniently by giving the change in the index ellipsoid constants.

If we choose x, y and z to be parallel to the principal dielectric axes of the crystal, then with zero applied field, we have [51]

$$\begin{aligned}
\left(\frac{1}{n^2}\right)_1 |_{E=0} &= \frac{1}{n_x^2} \\
\left(\frac{1}{n^2}\right)_2 |_{E=0} &= \frac{1}{n_y^2} \\
\left(\frac{1}{n^2}\right)_3 |_{E=0} &= \frac{1}{n_z^2} \\
\left(\frac{1}{n^2}\right)_4 |_{E=0} &= \left(\frac{1}{n^2}\right)_5 |_{E=0} = \left(\frac{1}{n^2}\right)_6 |_{E=0} = 0
\end{aligned} \tag{5.8}$$

The linear electrooptic effect is the change in the indices of the ordinary

and extraordinary rays that is caused by and is proportional to an applied electric field. The electric field changes the coefficients in the index ellipsoid due to the birefringence. The linear change of these coefficients $\left(\frac{1}{n^2}\right)_i$ $(i = 1, 2, \cdots, 6)$ due to an electric field $\boldsymbol{E}$ is defined by

$$\Delta\left(\frac{1}{n^2}\right)_i = \sum_{j=1}^{3} \boldsymbol{r}_{ij} E_j \tag{5.9}$$

where in the summation over j we use the convention $1 = x, 2 = y$, and $3 = z$. Equation (5.9) can be expressed in a matrix form as

$$\begin{vmatrix} \Delta\left(\frac{1}{n^2}\right)_1 \\ \Delta\left(\frac{1}{n^2}\right)_2 \\ \Delta\left(\frac{1}{n^2}\right)_3 \\ \Delta\left(\frac{1}{n^2}\right)_4 \\ \Delta\left(\frac{1}{n^2}\right)_5 \\ \Delta\left(\frac{1}{n^2}\right)_6 \end{vmatrix} = \begin{vmatrix} r_{11} & r_{12} & r_{13} \\ r_{21} & r_{22} & r_{23} \\ r_{31} & r_{32} & r_{33} \\ r_{41} & r_{42} & r_{43} \\ r_{51} & r_{52} & r_{53} \\ r_{61} & r_{62} & r_{63} \end{vmatrix} \begin{vmatrix} E_1 \\ E_2 \\ E_3 \end{vmatrix} \tag{5.10}$$

The 6×3 matrix with elements r_{ij} is called the electrooptic tensor which linearly relates E_j applied to a crystal to the resultant change in the coefficients $\left(\frac{1}{n^2}\right)_i$. Therefore,

$$\left(\frac{1}{n^2}\right)_i = \left(\frac{1}{n^2}\right)_i \Big|_{E=0} + \Delta\left(\frac{1}{n^2}\right)_i . \tag{5.11}$$

From Eqs. (5.9) and (5.11), a field dependent index ellipsoid is obtained. The principal axes and their corresponding refractive indices of the resultant index ellipsoid

can be obtained by finding the eigenvalues of the matrix

$$\begin{bmatrix} \left(\frac{1}{n^2}\right)_1 & \left(\frac{1}{n^2}\right)_6 & \left(\frac{1}{n^2}\right)_5 \\ \left(\frac{1}{n^2}\right)_6 & \left(\frac{1}{n^2}\right)_2 & \left(\frac{1}{n^2}\right)_4 \\ \left(\frac{1}{n^2}\right)_5 & \left(\frac{1}{n^2}\right)_4 & \left(\frac{1}{n^2}\right)_3 \end{bmatrix}$$

The three eigenvalues correspond to the new values

$$\left(\frac{1}{n^2}\right)_{x'}$$
$$\left(\frac{1}{n^2}\right)_{y'}$$
$$\left(\frac{1}{n^2}\right)_{z'}$$

which determine the new directions of the principal axes of the index ellipsoid. The velocities of propagation of the polarized wave along the new principal axes are also expressed by

$$\begin{aligned} v_{x'} &= \frac{c}{n_{x'}} \\ v_{y'} &= \frac{c}{n_{y'}} \\ v_{z'} &= \frac{c}{n_{z'}} \end{aligned} \tag{5.12}$$

The relative phase change of the polarized wave is the phase retardance given by

$$\Gamma = \frac{2\pi(n_{z'} - n_{x'})L}{\lambda} \tag{5.13}$$

The retardance Γ is caused by the different velocities or different indices of refraction in z' and x' directions. Then, the polarization of the probing beam is changed due to the retardance, typically from circular polarization to ellipsoidal polarization in E-O sampling.

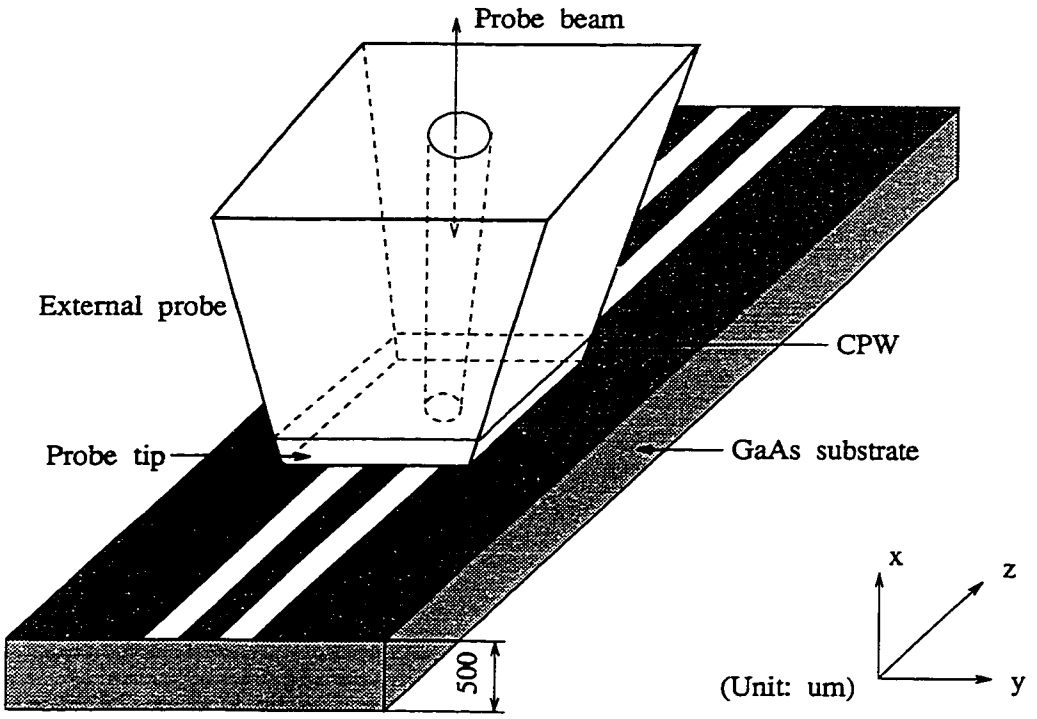

Figure 5.3: External E-O sampling configuration. The CPW is the device under test. The probe beam is ideally a few microns in diameter. The optical axis of the $LiTaO_3$ probe is parallel to the y-axis.

5.4 Full Wave Modeling of Electro-Optic High-Speed Probes

The external E-O sampling configuration is shown in Fig. 5.3 where a small probe tip is mounted over a CPW [52, 53, 54]. The probe is a truncated square pyramid of silica with a thin layer of birefringent material ($LiTaO_3$ or GaAs) at its tip. The tip face, typically a fraction of a millimeter in size, is centered on and parallel to the CPW metalization.

There are two types of the field disturbance in external E-O sampling. One is the probing invasiveness to the operation of the device under test, which is caused by the high dielectric constant material of the external probe. The other is the measured signal distortion in the E-O probe, which is determined primarily by the probe material and dimensions.

The full wave time domain field analysis technique is chosen to address the above problems for the following reasons:

1. Full wave time domain modeling technique is most suitable for this problem since we are studying high-speed pulse propagation on transmission lines as compared with the problem of narrow band high Q system analysis.

2. E-O sampling measures high-speed signals, therefore requiring transient response and full wave analysis. The full wave time domain method makes it possible to conduct this analysis, which can efficiently address dispersive and high-speed signal effects.

3. A complex three dimensional structure is involved in E-O sampling. The electromagnetic field of a high-speed signal is mostly confined in the discontinuity region between the probe tip and the transmission line. The FD-TLM full wave time domain method [17] is particularly efficient for handling three dimensional discontinuities with special interested areas.

4. To investigate the E-O response at the sampled output signal in E-O sampling, a detailed temporal field information along the probe beam path is required for the calculation of optical signals. The FD-TLM method offers this entire

information and especially gives the more detailed resolution of the field around the probe tip.

5. Frequency domain information over the entire range of interest, such as scattering parameters, may be obtained by a Fourier transform of the response to a broadband pulse.

Hence, the FD-TLM method is well suited to the external E-O sampling problem.

5.4.1 Field Simulation Using FD-TLM Method

The FD-TLM method has been introduced in Chapter 3. An example of the mesh structure for the simulation is shown in Fig. 5.4 and Fig. 5.5. The total size is $990\mu m$ in the x-direction, $260\mu m$ in the y-direction, and $800\mu m$ in the z-direction. The total number of grids is 80 in the x-direction, 45 in the y-direction, and 160 in the z-direction. Absorbing boundary conditions [55] are applied to the outer surface of the computational domain. The time-domain results are transformed into the frequency-domain characteristics of probes through the Fourier transform.

5.4.2 Simulation of Optical Signals

Birefringence in the E-O probe is a function of the electric field which penetrates the crystal and is fully described by the crystal's electro-optic tensor. Having obtained the field distribution in the probe using full wave analysis, the birefringence along the path of the probing beam (*i.e.* a double vertical path) can be integrated to

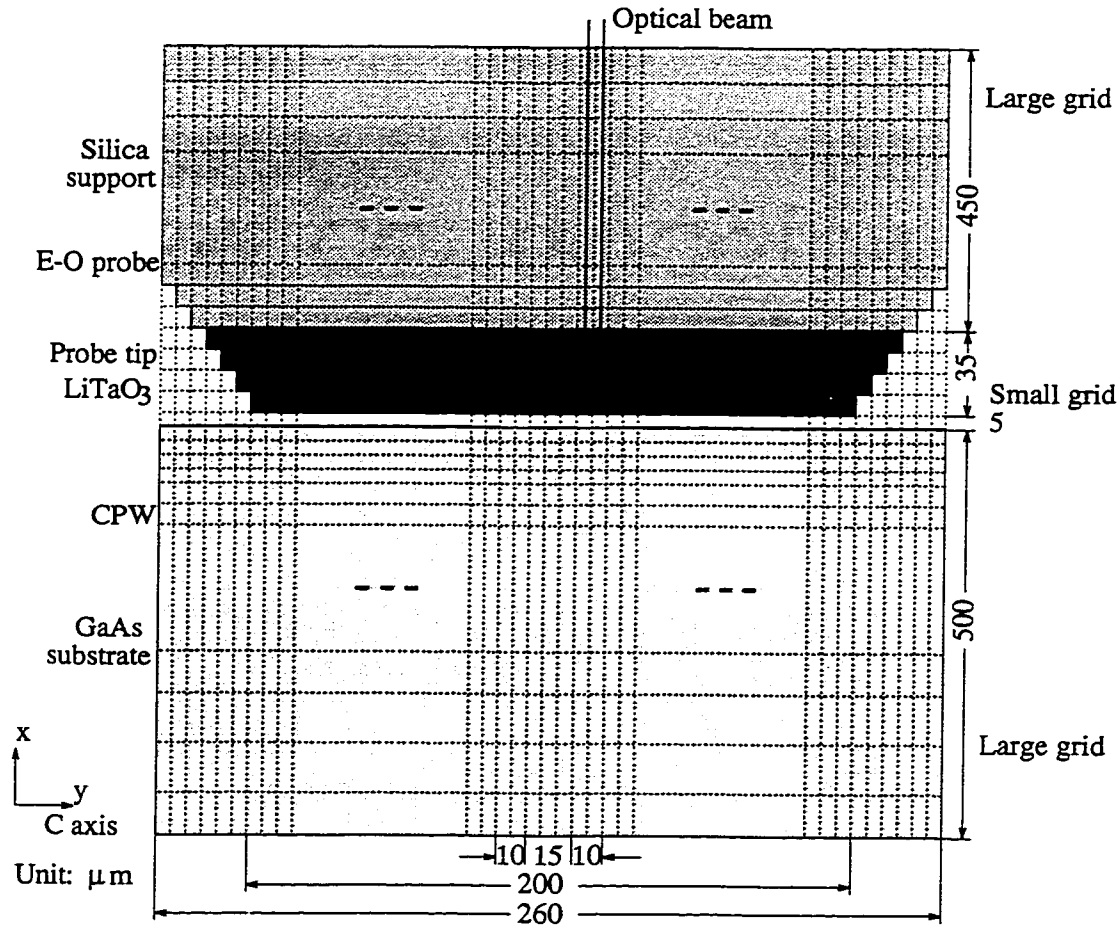

Figure 5.4: Mesh structure for the $x-y$ plane at the center of the probe. The total size is $260\mu m$ in the y-direction and $990\mu m$ in the x-direction.

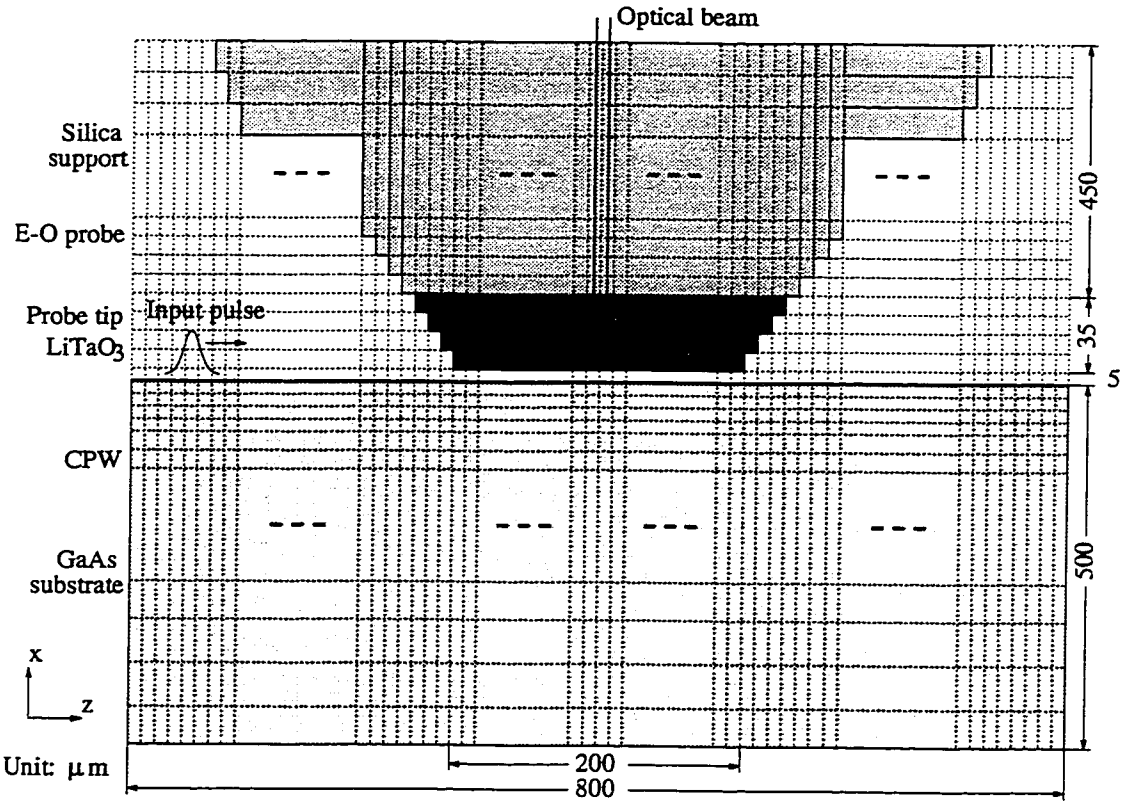

Figure 5.5: Mesh structure for the $x-z$ plane at the center of the probe. The total size is $990\mu m$ in the x-direction and $800\mu m$ in the z-direction.

give a predicted change in the beam polarization. This change, when analyzed and detected, yields the optical signal.

There are two arrangements for external probing, transverse and longitudinal. Transverse probing reacts to field components that are parallel to the surface of the circuit. Longitudinal probing interacts with the field components normal to the surface of the circuit plane. In the simulation, the optical probing beam is in the x-direction as shown in Fig. 5.3. Since the $LiTaO_3$ probe is used for transverse probing, the sampling-beam position within the crystal is just above the center of the CPW spacing.

Considering the spatially distributed electric field which can be obtained from the full wave simulation, the phase retardation Γ of a probing beam along the x-direction is given by the following discretized form in radians

$$\Gamma(E_x, E_y, E_z) = d\phi_c + \sum_{i=i1}^{i2} \frac{4\pi}{\lambda}[n_{y_i'}(E_x, E_y, E_z) - n_{z_i'}(E_x, E_y, E_z)]\Delta x_i \qquad (5.14)$$

where λ is the optical wavelength, Δx_i is the mesh size at ith node in the x-direction, and i_1 and i_2 are mesh indices which indicate the bottom and top mesh of the probe tip in the full wave analysis to define the probing light path in the probe tip. In the example shown in Fig. 5.4 and Fig. 5.5, i_1 and i_2 are taken to be 39 and 42, respectively. The new refractive indices $n_{y_i'}$ and $n_{z_i'}$ due to the E-O effect are the functions of the electric field at ith node. Combined with a static birefringence in the crystal, if applicable, $d\phi_c$ is introduced by an optical compensator which is used to supply an optical bias of $\pi/2$ for a maximal and linear measurement response

[47, 51].

Practically, an optical polarization analyzer is used to measure the degree of the birefringence induced in the probe. The retardation Γ yields a normalized optical analyzer output as [51]

$$\frac{I_o}{I_i} = \sin^2\left(\frac{\Gamma(E_x, E_y, E_z)}{2}\right) \tag{5.15}$$

where I_o/I_i has been explicitly written as a function of the electric field. The optical signal power is detected by a photodetector to yield an electrically measurable voltage.

5.4.3 Characterization of Electro-Optic Probing

The characteristics of external $LiTaO_3$ E-O probes are investigated in both time domain and frequency domain by full-wave simulation and the Fourier transform.

The field disturbance is investigated first. Several perturbations in a propagating electrical waveform can result from the interaction of the electrical signal with the probe tip which is the reflections at the points where the guided waveform enter and exit the E-O probe input and output discontinuities and the boundary between the $LiTaO_3$ and the fused silica support. Three interfaces create reflection sources that direct part of the electrical signal back to the excitation point. Fig. 5.6 shows the field distribution of E_y, which is the dominant component of the electric field on the CPW, $5\mu m$ above the CPW with and without the $LiTaO_3$ probe. The

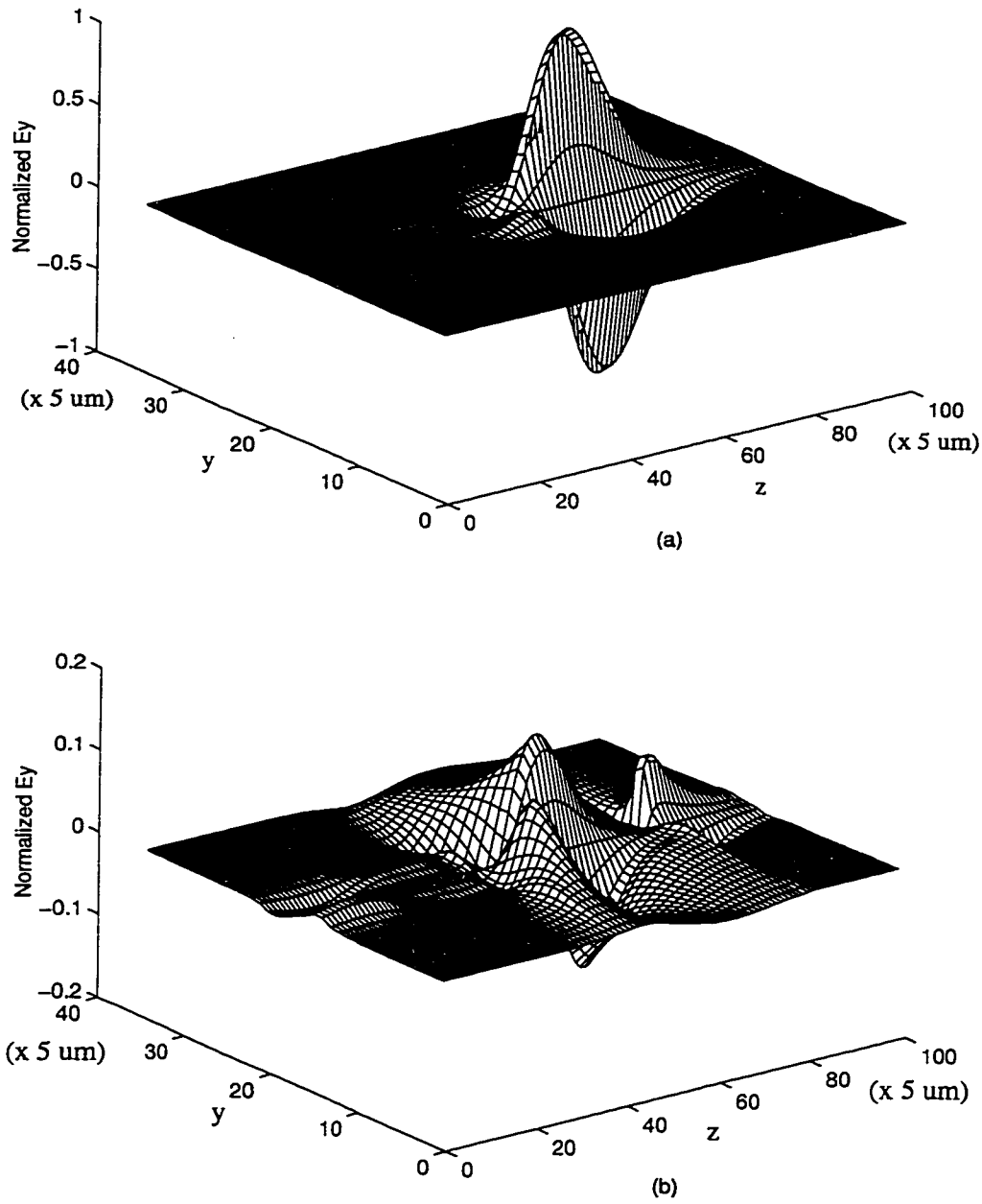

Figure 5.6: The spatial waveform of E_y $5\mu m$ above the CPW. The pulse propagates in the z-direction. The field values are normalized to the maximum value without probe. (a). Without probe. (b). With probe, probe thickness = $20\mu m$, probe length and width = $200 \times 200\mu m$.

pulse propagates in the z-direction. Field values are normalized to the maximum value without the probe. The field disturbances, as seen in Fig. 5.6, are attributed to the probing discontinuities, dispersive effects and surface waves on and above the CPW. Two peaks in Fig. 5.6(b) occur exactly at the edges of the probe. The surface waves observed in Fig. 5.6(b) spread much further away from the CPW central conductor than that in Fig. 5.6(a), implying that the close placement of the probe may produce significant cross-talk between adjacent devices or elements on the circuit board, but the E-O sensitivity increases.

Due to the high dielectric constant of the probe material and its close placement above the CPW, the field in the probe and surrounding regions must satisfy new boundary conditions which require phase matches at both CPW-air and air-probe tip interfaces. The speed of the electromagnetic wave is lower in a high dielectric material. This difference in speed results in refractions in wave propagation. Therefore the quasi-TEM mode, which is essentially the same as the static case, is disturbed in the probe where the field is sampled.

E-O probe invasiveness to the operation of the device under test can be evaluated in terms of the device scattering parameters. S-parameters of the probe with the CPW extracted from the field simulation serve to quantitatively describe invasiveness induced by external probing. Figures 5.7 - 5.10 show the magnitude of S_{11} on the CPW with $LiTaO_3$ probe which produces significant invasiveness.

Fig. 5.7 shows S_{11} as a function of frequency in terms of different probe

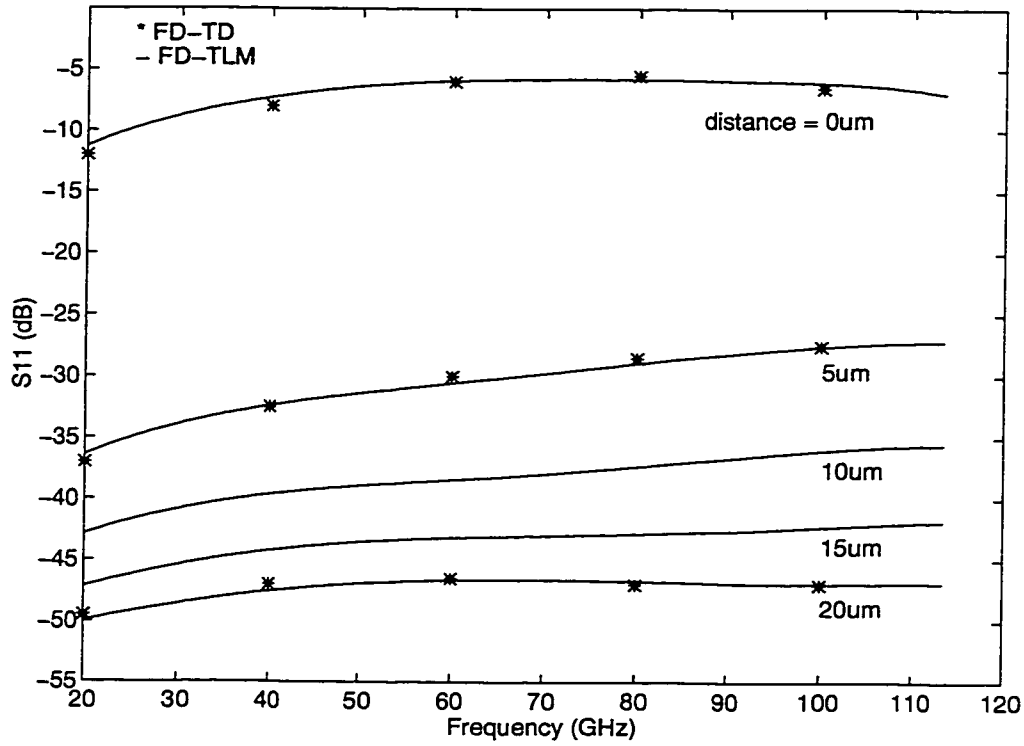

Figure 5.7: Magnitude of the reflection coefficient S_{11} on the CPW for different probe distance. Probe thickness = $20\mu m$, CPW center conductor = $15\mu m$, CPW spacing = $10\mu m$. FD-TD results are from [45].

distance. The FD-TLM simulation results are compared with the FD-TD simulation results [56] and the discrepancy is within 5%. The invasiveness increases (S_{11} increases) as the frequency increases and the probe distance decreases. As the frequency increases, the electromagnetic field radiates further into the probe than at low frequencies, which generates more discontinuity effect, therefore more electromagnetic field is reflected back by the high dielectric constant material of the $LiTaO_3$ probe. For probe distance less than $5\mu m$, it is observed that the invasiveness increases dramatically as the probe approaches the CPW.

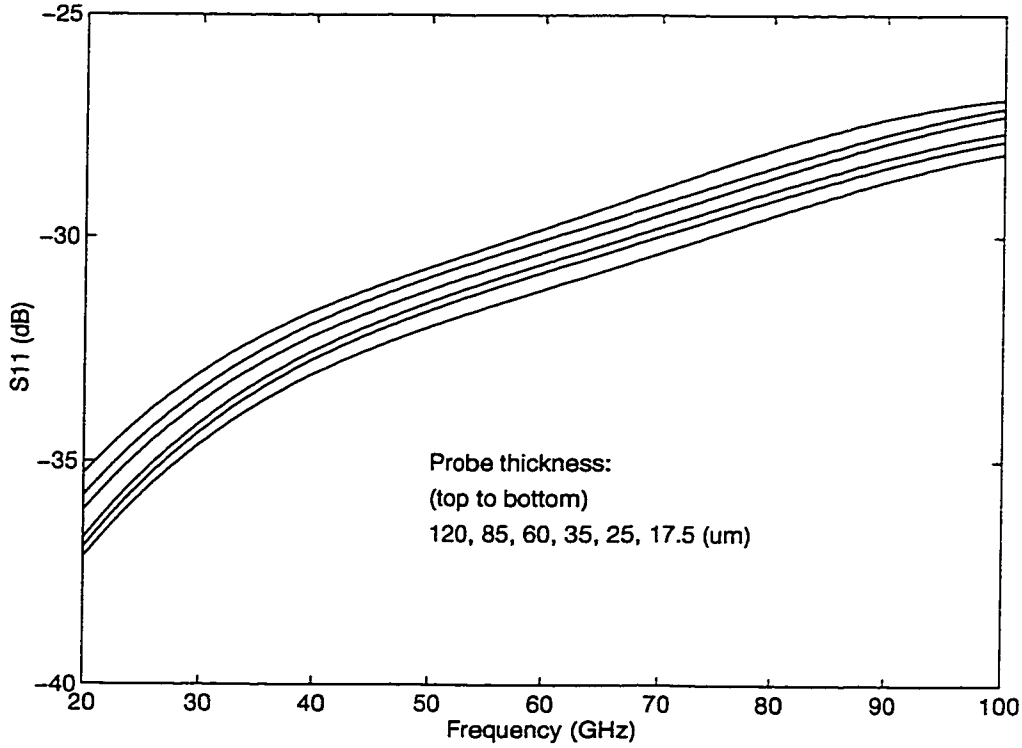

Figure 5.8: Magnitude of the reflection coefficient S_{11} on the CPW for different probe thickness. Probe distance = $5\mu m$, CPW center conductor = $15\mu m$, CPW spacing = $10\mu m$.

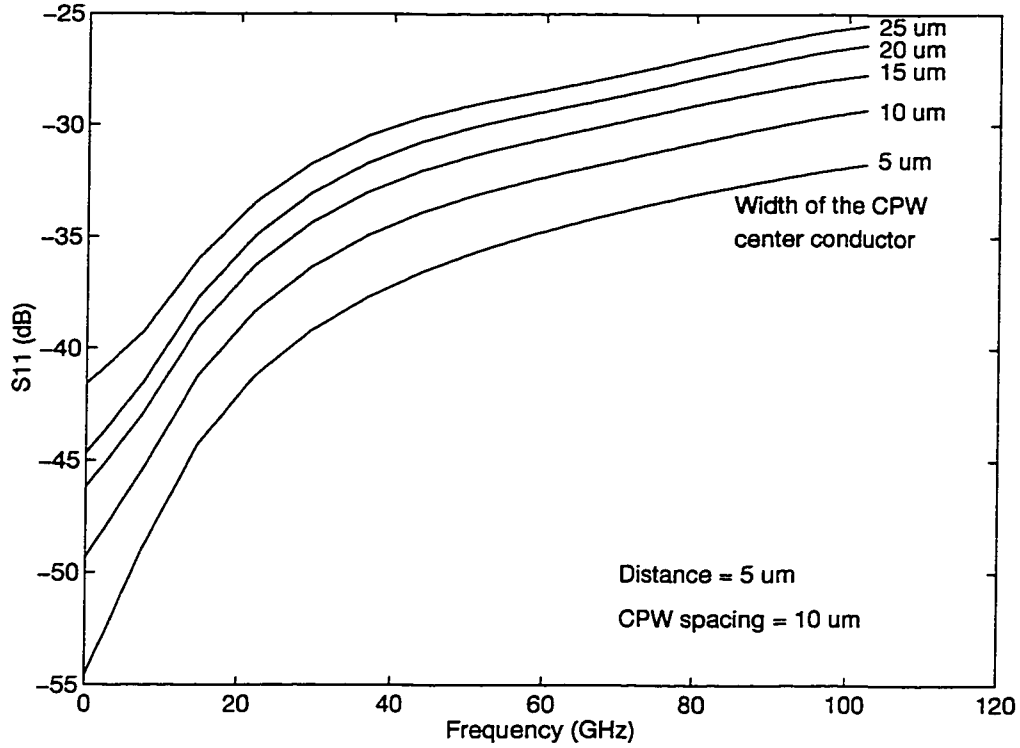

Figure 5.9: Magnitude of the reflection coefficient S_{11} on the CPW for different width of the CPW center conductor. Probe thickness $= 20\mu m$. A constant electric field is assumed on the CPW spacing.

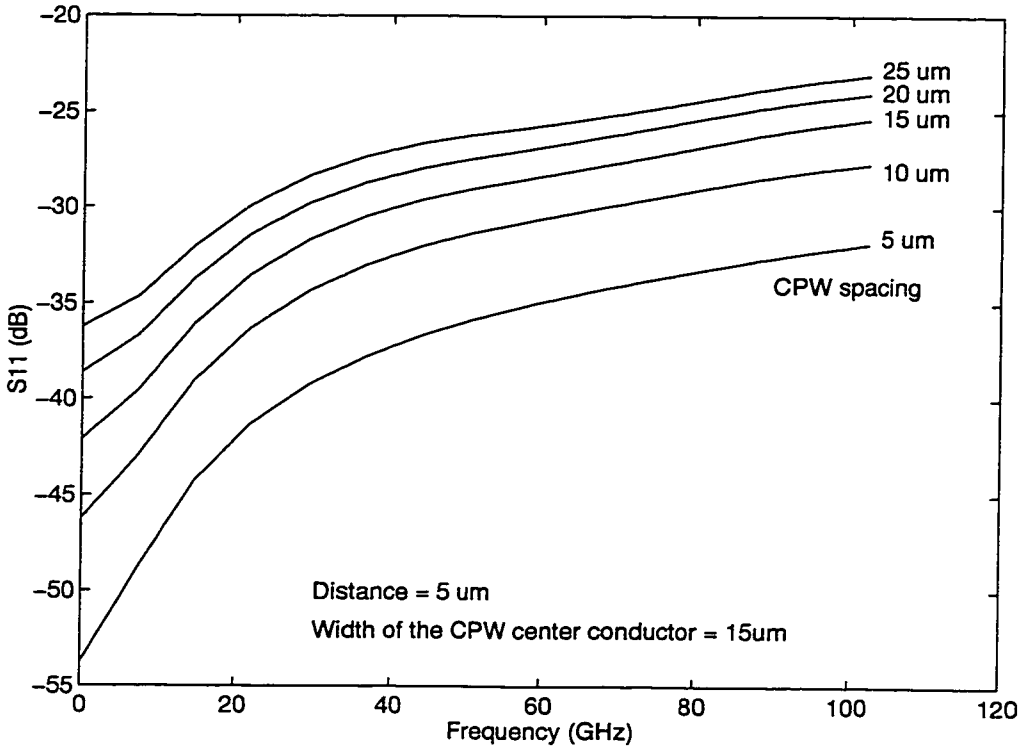

Figure 5.10: Magnitude of the reflection coefficient S_{11} on the CPW for different CPW spacing. Probe thickness $= 20\mu m$. A constant electric field is assumed on the CPW spacing.

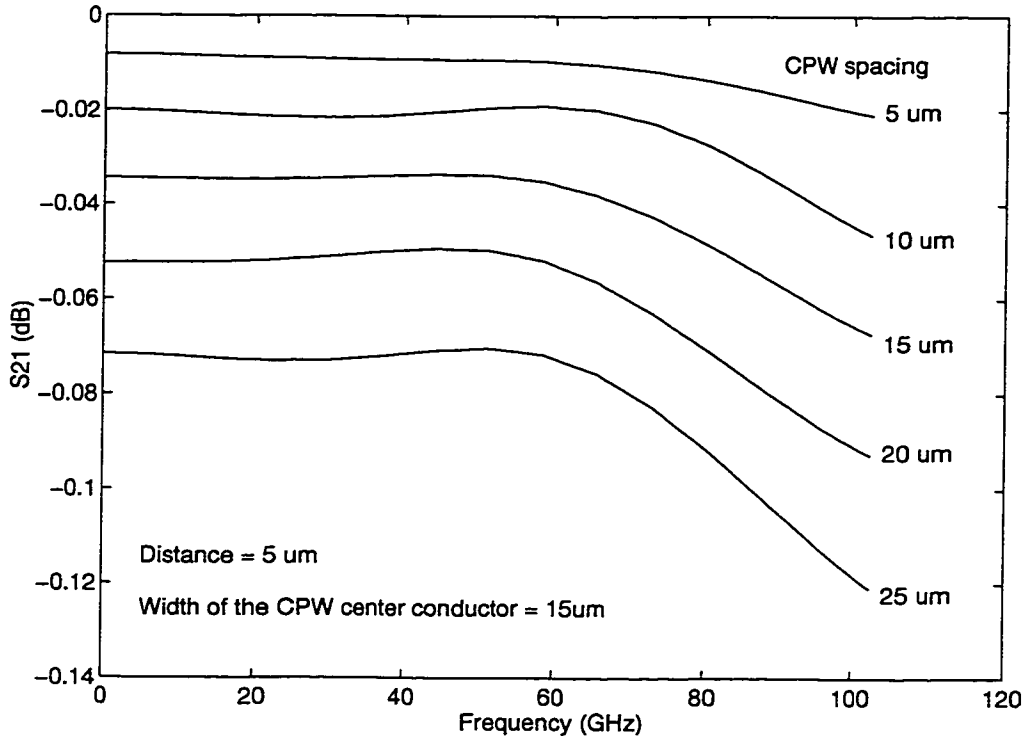

Figure 5.11: Magnitude of the transmission coefficient S_{21} on the CPW for different CPW spacing. Probe thickness = $20\mu m$. A constant electric field is assumed on the CPW spacing.

Fig. 5.8 shows S_{11} versus frequency and $LiTaO_3$ probe thickness. The thicker the probe tip, the larger the invasiveness, which is due to the slightly different discontinuities generated by the different probe thickness.

Fig. 5.9 shows S_{11} versus the width of the CPW center conductor, where the constant electric field is assumed on the CPW spacing. The wider the CPW center conductor, the weaker the cancellation of the transverse field components in the middle of the CPW, which leads to more transverse field reflection and more invasiveness consequently. Fig. 5.10 shows S_{11} versus the CPW spacing. The wider the spacing, the more transverse field is reflected, therefore more invasiveness.

The transmission coefficient S_{21} on the CPW with a $LiTaO_3$ probe is also a function of the frequency, the probe distance, the width of the CPW center conductor, and the CPW spacing. As an example, we show S_{21} versus frequency and CPW spacing in Fig. 5.11 where S_{21} decreases (invasiveness increases) as the frequency increases after $60GHz$ and as the spacing increases. This analysis is in accordance with the analysis for S_{11} in Fig. 5.10.

It is also necessary to examine the optical signal for invasiveness. When the probe is in contact with the CPW, the signal's electric field threads almost completely into the crystal. When the probe is placed a finite distance from the CPW, most of the field is confined to the air gap due to the high dielectric constant of the crystal. As the probe approaches the CPW, a rapid increase in the optical signal is expected, as is confirmed in Fig. 5.12. Compared to Shinagawa's result for

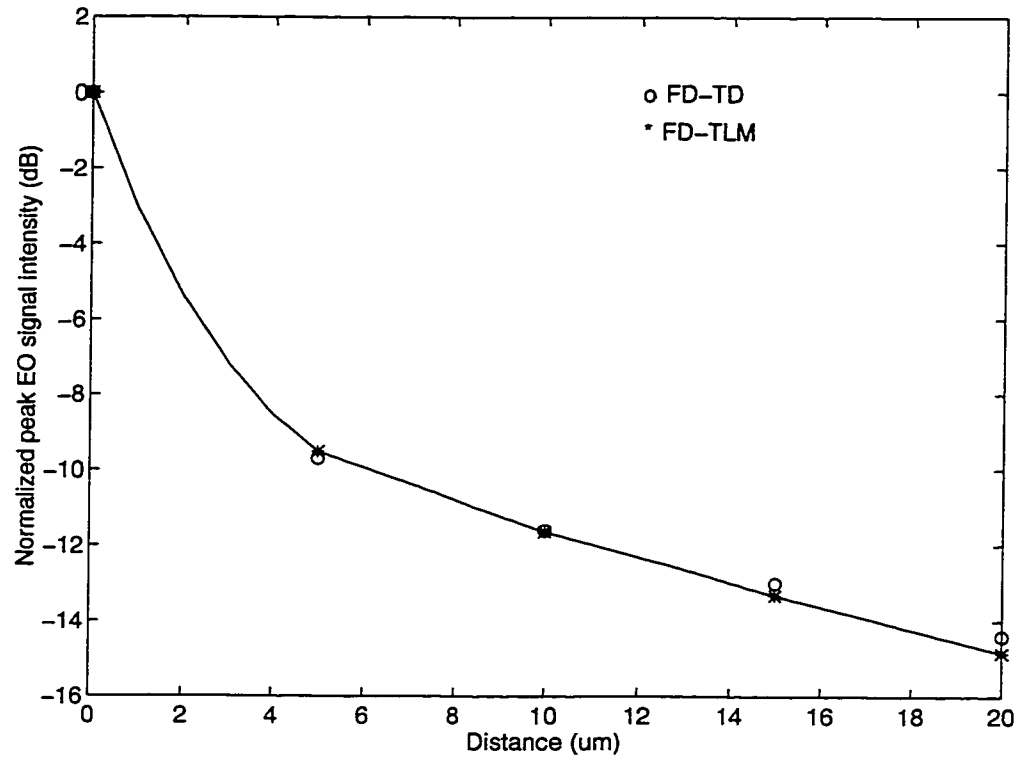

Figure 5.12: Normalized peak value of optical signal generated in the $LiTaO_3$ probe versus probe distance. Symbols denote the simulation points. Exponential curves are fitted to the simulation. Probe thickness = $20\mu m$, CPW center conductor = $15\mu m$, CPW spacing = $10\mu m$. FD-TD results are from [45].

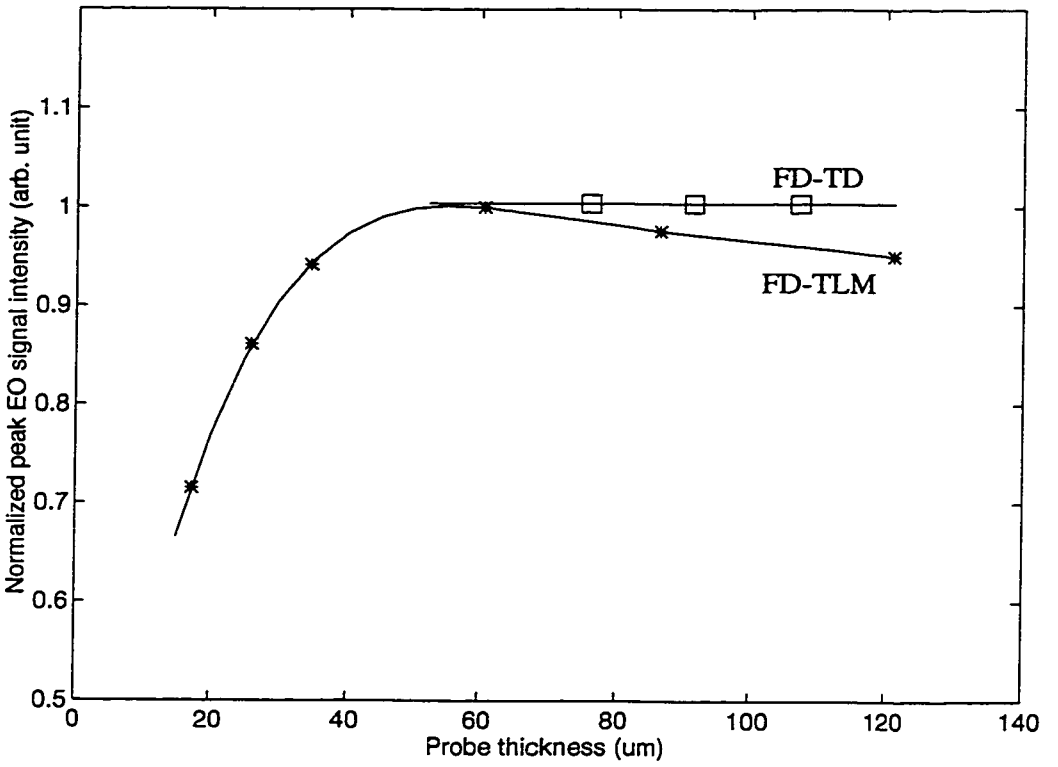

Figure 5.13: Normalized peak optical signal intensity versus probe tip thickness. The signal intensity decreases when the probe tip is thicker than $60\mu m$, the effect of which is attributed to the increased reflection caused by thicker probes. Probe distance = $5\mu m$, CPW center conductor = $15\mu m$, CPW spacing = $10\mu m$. FD-TLM simulation result is compared with FD-TD result from [45].

a GaAs probe [57] and Valdmanis's for a $LiTaO_3$ probe [58], the fullwave simulation results basically agree with the experimental data. The optical signal shown in this figure is normalized to the signal intensity generated when the $LiTaO_3$ probe is in contact with the CPW. At distances larger than $3\mu m$, the optical signal does not decrease substantially when the probe is moved away from the CPW. This agrees qualitatively with Heutmaker's measurement results (See Figure 1 in [59]).

The probe thickness is a trade-off factor which can be achieved between the performance and the measurement sensitivity. High measurement sensitivity is expected for thicker probes because of a longer sampling path along which the overall optical signal is integrated in proportion to the electric field in the probe tip, but thicker probes generate more invasiveness as discussed before. The electric field is mostly confined in a very limited region near the probe facet. Consequently, the sensitivity is attributed dominantly to the field in that limited region. This result is illustrated clearly in Fig. 5.13. There is not only a saturation-like phenomenon (FD-TD result) in the relation of the optical signal intensity versus the probe tip thickness, but also the optical signal intensity decreases a small amount when the probe tip is thicker than $60\mu m$, the effect of which is attributed to the increased reflection caused by thicker probes discussed in Fig. 5.8. It suggests that there is an optimum probe thickness for maximum sensitivity.

In order to investigate the measurement error caused by the temporal waveform distortion, the information in the frequency domain is extracted from the field simulation results in the time domain by Fourier transform. The distortion, there-

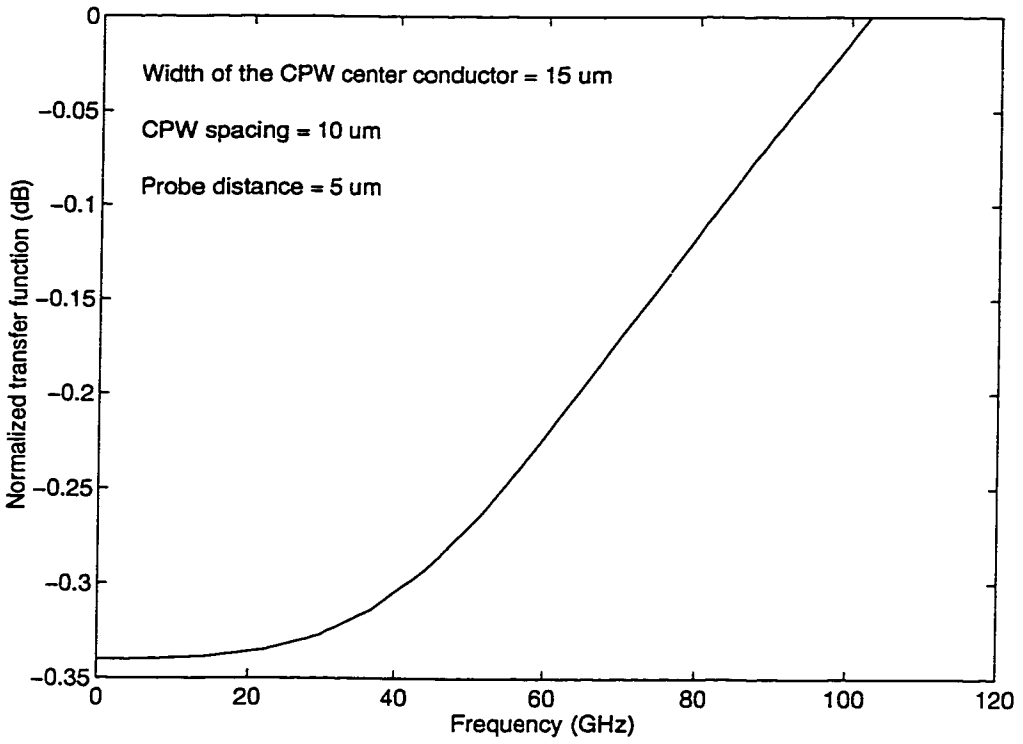

Figure 5.14: The magnitude of the normalized system transfer function of the external E-O sampling for the $LiTaO_3$ probe thickness of $20\mu m$.

fore, can be evaluated by characterizing the system transfer function in the frequency domain [45, 60].

In this full wave simulation, the E-O probe system is a three-port system. The optical output should be able to show the electric input waveform as accurately as possible. To characterize the properties of the E-O system, a new transfer function is reasonably associated with the input port defined as a sampling spot on the CPW rather than the input reference plane in [45] in order to directly sample the signal on the measurement point without the phase effect of the reference plane. The output port is defined as the optical retardance $\Gamma(t)$ since the optical retardance is linearly proportional to the signal voltage output from the photo diodes. Based on the above analysis, the transfer function $H(\omega)$ can be defined in the frequency domain by

$$H(\omega) = \frac{\Gamma(\omega)}{E_D(\omega)} \tag{5.16}$$

where $\omega = 2\pi f$, $E_D(\omega)$ is the Fourier transform of the time domain input electric field $e_D(t)$ at the sampling point on the CPW where the probe will be in position and the laser beam will focus on in measurement, and $\Gamma(\omega)$ is the Fourier transform of the time domain optical retardance of $\Gamma(t)$. Fig. 5.14 shows the magnitude of the normalized system transfer function for the $LiTaO_3$ probe with thickness of $20\mu m$. It is seen that, from this figure, the magnitude of the probe transfer function is not constant for all frequencies, which indicates some signal waveform distortion existing in the E-O sampling system.

5.5 Concluding Remarks

In summary, the variable grid size FD-TLM modeling for analyzing the effects of external electro-optic probes with CPW test structure is demonstrated by the simulation of external E-O probes with different CPW configurations. The important simulation results are presented in this chapter along with the actual performance of the $LiTaO_3$ probe with CPW test structure in both time and frequency domains. Finally, the new transfer function of the electro-optic sampling system is defined and examined for the characterization of the measurement accuracy.

Chapter 6

Three-Port Electrical and Optical Model for $LiTaO_3$ High-Speed Electro-Optic Probe with CPW Test Structure

In this chapter, a three-port electrical and optical model for $LiTaO_3$ E-O probe with the high-bandwidth CPW test structure is developed by combining full wave FD-TLM modeling technique and neural network techniques. The model weighting parameters are obtained and can be used in high-speed electro-optic measurements.

6.1 Introduction

The external $LiTaO_3$ electro-optic probe is widely used in electro-optic sampling measurements because of its higher sensitivity than the GaAs probe. The invasiveness and signal distortion of the $LiTaO_3$ probe with respect to different probe positions and the different dimensions of the high-bandwidth CPW test structure have been evaluated systematically in the previous chapter. To diagnose integrated circuits, it is desirable to measure signal waveforms on internal circuits. The E-O sampling equipment is expected to sample the signals at different circuit configurations, one by one, by placing the probe tip and optical beam right above the measurement point. Since the $LiTaO_3$ probe perturbs signals slightly, its effects on incident, transmitted, and reflected signals have to be corrected for accurate measurement. A general and systematic model of $LiTaO_3$ probe test structure is required for quantitative measurement of E-O sampling.

We have introduced two models, a discrete time domain model [61] and a simplified model which in this case is a linear circuit model [62]. The discrete time domain model is extremely accurate but suffers from the disadvantage of requiring large amounts of computer resources, time and memory, to implement. It is quite impractical to use the discrete time domain model in calibration procedures that call upon the model many times to find the necessary parameters. The simplified linear circuit model [62] describes the scattering parameters of the probe as a function of the probe distance for the probe mounted near a specific CPW, which is

not applicable to different CPW configurations, also the optical properties of the probe are not included in the model. Obviously it is not sufficient for system applications. There is a need for a three-port model that accurately describes all of the performance features of the probe such as scattering parameters and system transfer function. The three-port electrical and optical model of the $LiTaO_3$ probe with CPW test structure is a function of the physical properties of the probe and CPW test structure.

A field based three-port electrical and optical model for $LiTaO_3$ probe with CPW test structure is developed by combining full wave electromagnetic modeling technique and neural network techniques. The influence of the $LiTaO_3$ probe on the scattering parameters of the CPW test structure and on the quality of sampled signals is taken into the consideration of the three-port electrical and optical model. First, the full wave modeling of the electromagnetic field in the sampling configuration and the resultant probe birefringence are required to obtain the scattering parameters and transfer functions of the probe with CPW test structure as a function of probe distance, CPW spacing, width of the CPW center conductor, and operating frequency. Second, the weighting parameters for the three-port model are optimized by mapping the full-wave field simulation results to the fully connected feedforward neural networks using neural network algorithms which is powerful in terms of its nonlinearity and adaptivity.

The three-port electrical and optical model provides necessary information for engineers to calibrate the E-O measurement and to set up E-O measurement

systems in order to achieve optimum E-O sampling results. The three-port model has the same accuracy as the full wave discrete time domain model, but electrical and optical characteristics are obtained much faster and simpler than the full wave simulation, so that it is a promising engineering tool for high-speed E-O sampling measurement. With this three-port electrical and optical model, it is possible to de-embed both invasiveness and waveform distortion in external E-O sampling given the sampling configuration and dimensions. It moves E-O sampling further towards the quantitative measurement.

6.2 Definition of the Three-Port Electrical and Optical Model

The probe invasiveness and distortion are the two major causes responsible for the discrepancies between the signal to be measured and the sampled signal. The three-port electrical and optical model developed in this chapter attempts to give a fast and simple calibration tool to correct the discrepancies.

The $LiTaO_3$ probe with CPW test structure and its three-port model are shown in Fig. 6.1. In this three-port model for the $LiTaO_3$ probe with CPW test structure, a commercially available Terametrics Model 200-TIR probe is used. The thickness of the $LiTaO_3$ probe tip is $20\mu m$ and the surface dimension is $200 \times 200 \mu m^2$. An electric high-speed signal is launched at the input reference plane towards port

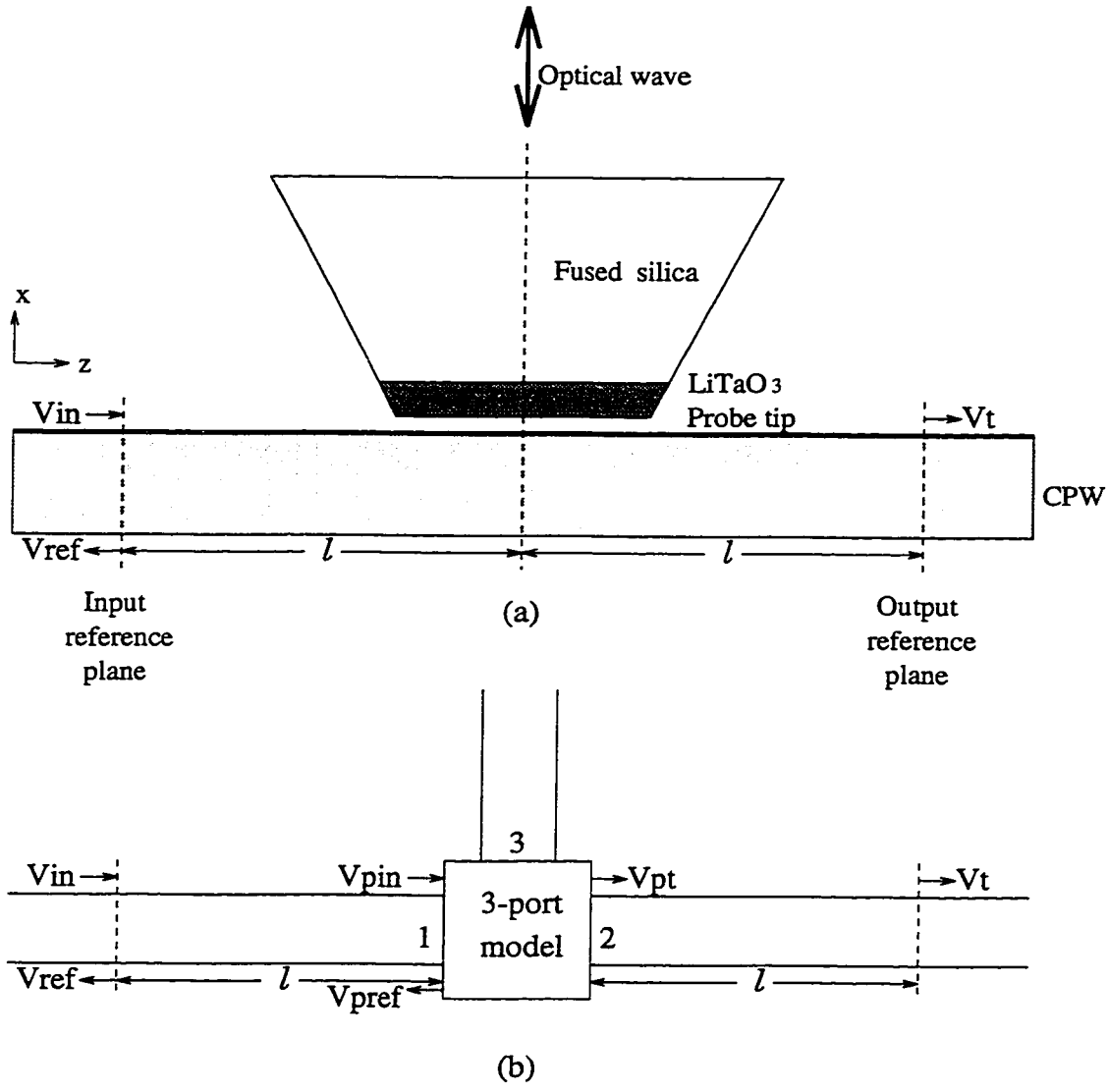

Figure 6.1: (a) $LiTaO_3$ probe with CPW test structure. (b) Three-port electrical and optical model for the above structure.

1. Because of the probe discontinuity, a small part of the input signal reflects from port 1 and propagates back towards the input reference plane. The main part of the input signal propagates through the three-port model and outputs at port 2. A laser beam travels down the port 3 along the axis of the probe and reflects off the probe tip, which yields an E-O measurement of the electric field at the optical sampling point.

The scattering parameters (S parameters) from microwave network theory are used to define the interrelation between the signals at port 1 and port 2 since the signals propagating through port 1 and port 2 are carried in the electromagnetic field on the CPW. The external probing system is symmetric so that only S_{11} and S_{21} are required for the three-port model. To be accurate, the input and output waves are measured on the input and output reference planes which are away from the probe region and the scattering parameters are directly obtained as

$$S_{11r} = \frac{V_{ref}}{V_{in}} \tag{6.1a}$$

$$S_{21r} = \frac{V_t}{V_{in}} \tag{6.1b}$$

The S parameters obtained from above equations are of course dependent of the positions of input and output reference planes, the physical dimension of the CPW test structure, the probe distance in respect to CPW, and the signal frequency.

To de-embed the effect of two reference planes, we move the reference planes to the center of the probe by assuming that the probe is taken away. From Fig. 6.1,

we have

$$V_{in}e^{-j\beta l} = V_{pin} \tag{6.2a}$$

$$V_{pt}e^{-j\beta l} = V_t \tag{6.2b}$$

$$V_{pref}e^{-j\beta l} = V_{ref} \tag{6.2c}$$

where the frequency-dependent phase is given in [62] as

$$\beta(f) = 2\pi\frac{f}{c}\sqrt{\epsilon_{eff}(f)} \tag{6.3}$$

The frequency-dependent effective dielectric constant is analytically approximated by [62, 63]

$$\sqrt{\epsilon_{eff}(f)} = \sqrt{\epsilon_q} + \frac{\sqrt{\epsilon_r} - \sqrt{\epsilon_q}}{1 + a(f/f_{te})^{-b}} \tag{6.4}$$

The parameter b has been found to be independent of geometry as a constant (~ 1.8) [62, 63]. The quasistatic effective permittivity takes the form

$$\epsilon_q = (\epsilon_r + 1)/2 \tag{6.5}$$

The coefficient a in (6.4), which is geometry dependent and determines the frequency dependency, is given by

$$q = \log\left(\frac{w}{d}\right) \tag{6.6a}$$

$$u = 0.54 - 0.64q + 0.015q^2 \tag{6.6b}$$

$$v = 0.43 - 0.86q + 0.54q^2 \tag{6.6c}$$

$$\log(a) = a_0\left(u\log\left(\frac{w}{s}\right) + v\right) \tag{6.6d}$$

where w is the center conductor width, s is the CPW spacing, d is the thickness of the CPW substrate, and the fitting coefficient a_0 is selected as 0.0013. The surface wave TE_1 mode cutoff frequency is defined as [62, 63]

$$f_{te} = \frac{c}{4d\sqrt{\epsilon_r - 1}} \tag{6.7}$$

where c is the speed of light in free space. With the moving of two reference planes, the S parameters at the probe center can be obtained from (6.1) and (6.2) as

$$S_{11} = \frac{V_{pref}}{V_{pin}} = \frac{V_{ref}e^{j\beta l}}{V_{in}e^{-j\beta l}} = S_{11r}e^{j2\beta l} = |S_{11}|e^{j\phi_{S_{11}}} \tag{6.8a}$$

$$S_{21} = \frac{V_{pt}}{V_{pin}} = \frac{V_t e^{j\beta l}}{V_{in}e^{-j\beta l}} = S_{21r}e^{j2\beta l} = |S_{21}|e^{j\phi_{S_{21}}} \tag{6.8b}$$

The S parameters obtained from (6.8) are not dependent of the positions of the input and output reference planes, and completely describe the electrical performance of the $LiTaO_3$ probe with the CPW test structure, therefore are the definition of the S parameters in the three-port model.

Port 3 is different from port 1 and port 2 because the input to port 3 is an optical beam and the output from port 3 is a modulated optical beam instead of the electrical signals in port 1 and port 2. The phase retardance Γ in the modulated output optical beam is a measure of the electro-optic response as a function of the electric field in the probe. It can be directly related to the electric field on the sampling spot on the CPW test structure and detected through a beam-splitter and a pair of photo detectors which convert the retardance to the voltage output. Since the electro-optic response is extremely small in most situations and the probing

beam is biased optically for maximum sensitivity and linearity, it can be assumed that the signal output voltage from the photo detectors is linearly proportional to the retardance Γ by a ratio of the photo diodes' efficiency.

Since the input and output reference planes have been moved to the center of the probe, the sampling spot on the CPW under the center of the probe is selected as the electric signal input port. Therefore, the probe transfer function H defined in the previous chapter

$$H = \frac{\Gamma}{E_{CPW}} = |H|e^{j\phi_H} \tag{6.9}$$

is reasonably selected as a characteristic function which completely describes the interrelation between the signals at port 1 (port 2) and port 3. The probe distortion and the CPW dispersion are fully characterized by the probe transfer function. The electric field E_{CPW} at the sampling spot on the CPW transmission line without the probe mounted is chosen as the input reference of the probe transfer function, which is convenient to directly obtain the electric signal at the sampling spot under the probe from the optical output Γ and the transfer function by putting the probe wherever interested.

The scattering parameters between port 1 and port 2 and the transfer function between port 1 (port 2) and port 3 fully characterize the three-port electrical and optical model of the $LiTaO_3$ probe with the CPW test structure. Certainly the scattering parameters and transfer function are dependent of the signal frequency and the physical properties of the test structure which include probe distance, CPW

spacing, and the width of the CPW center conductor. In diagnosing the integrated circuit, wherever the probe is moved to, the scattering parameters and the transfer function are expected in terms of the physical properties at the sampling spot. The full wave analysis for each individual sampling configuration is impractical because of the computation burden. Therefore, a fast, accurate, and effective three-port electrical and optical model is required with scattering parameters and transfer function as its outputs and signal frequency, probe distance, CPW spacing, and the width of the CPW center conductor as its inputs. In following sections, full wave computations for some individual cases covering the interested input range are carried out to obtain the corresponding output data for the three-port model. Then, simple neural networks are constructed for the three-port model and the input-output mapping algorithm is conducted to generate the weighting parameters for the model which allow the on-line calculation of the scattering parameters and transfer function at any sampling spot where the physical properties are within the validation range of the model.

6.3 Fundamentals of Neural Networks

The neural network technique is used to generate the three-port electrical and optical model for $LiTaO_3$ probe with CPW test structure because of the excellent input-output mapping capability of the neural network technique and the availability of the necessary input-output knowledge obtained through the full wave FD-TLM

simulation. The fundamentals of neural networks are briefly introduced in this section.

A neural network [64] is a massively parallel distributed processor that has a natural propensity for storing experimental knowledge and making it available for use. It resembles the brain in two respects:

1. Knowledge is acquired by the network through a learning process.

2. Interneuron connection strengths known as synaptic weights are used to store the knowledge [64].

The use of neural networks offers some useful properties and capabilities:

1. Nonlinearity. A neuron is basically a nonlinear device. Consequently, a neural network, made up of an interconnection of neurons, is itself nonlinear. Nonlinearity is a highly important property, particularly if the underlying physical mechanism responsible for the generation of an input signal is inherently nonlinear.

2. Input-output mapping. A popular learning process called supervised learning involves the modification of the synaptic weights of a neural network by applying a set of task examples. Each example consists of a unique input signal and the corresponding desired response. The network is presented an example picked at random from the set, and the synaptic weights of the network are modified so as to minimize the difference between the desired response and the actual response of the network produced by the input signal in accordance with an appropriate statistical criterion. The training of the network is repeated for many examples in the set until the network reaches a steady state, where there are no further significant changes

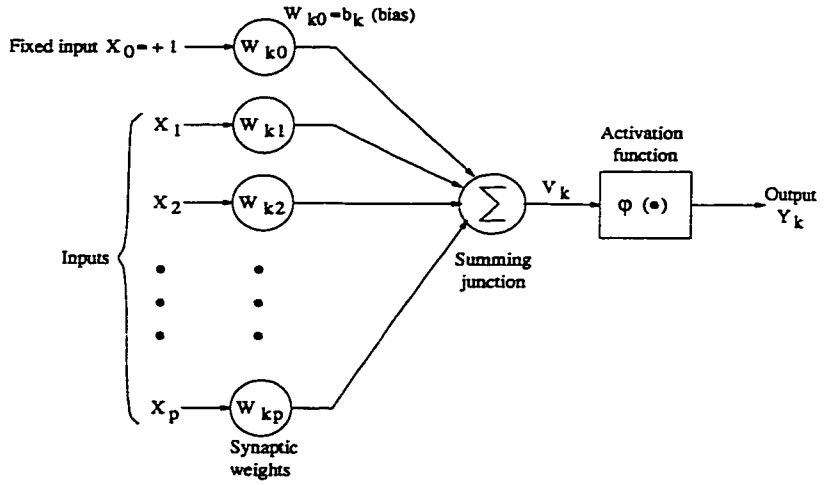

Figure 6.2: Nonlinear model of a neuron.

in the synaptic weights; the previously applied training examples may be reapplied during the training session but in a different order. Thus the network learns from the examples by constructing an input-output mapping for the problem at hand.

3. Adaptivity. Neural networks have a built-in capability to adapt their synaptic weights to the changes in the surrounding environment.

4. No information or knowledge of the system is needed. In neural networks, the system is a black box, the network will adapt its synaptic weights itself. In conventional methods, the function of the system is necessary at the beginning.

A neuron is an information-processing unit that is fundamental to the operation of a neural network. The nonlinear model of a neuron is shown in Fig. 6.2. Mathematically, we may describe a neuron k by writing the following equations:

$$v_k = \sum_{j=0}^{p} w_{kj} x_j = \sum_{j=1}^{p} w_{kj} x_j + b_k \tag{6.10}$$

and

$$y_k = \varphi(v_k) \tag{6.11}$$

where the combination of fixed input $x_0 = +1$ and whose weight $w_{k0} = b_k$ accounts for the bias b_k which may increase the net input of the activation function. The hyperbolic tangent activation function $\varphi(\cdot)$ is used in this research and written as [65]

$$\varphi(v_k) = \frac{1 - \exp(-2v_k)}{1 + \exp(-2v_k)} \tag{6.12}$$

The neural network structure applied in this research is a fully connected feedforward network with one hidden layer and output layer shown in Fig. 6.3, which is said to be fully connected in the sense that every node in each layer is connected to every other node in the adjacent forward layer. The input signal propagates through the network in a forward direction, on a layer-by-layer basis. The source nodes in the input layer of the network supply respective elements of the activation pattern (input vector), which constitute the input signals applied to the hidden neurons. The output signals of the hidden neurons are used as inputs to the output layer of neurons. The set of output signals of the output neurons constitutes the overall response of the network to the activation pattern supplied by the input source nodes. The function of the hidden neurons is to intervene between the external input and the network output.

Among the many interesting properties of a neural network, the property that is of primary significance is the ability of the network to learn from its environment,

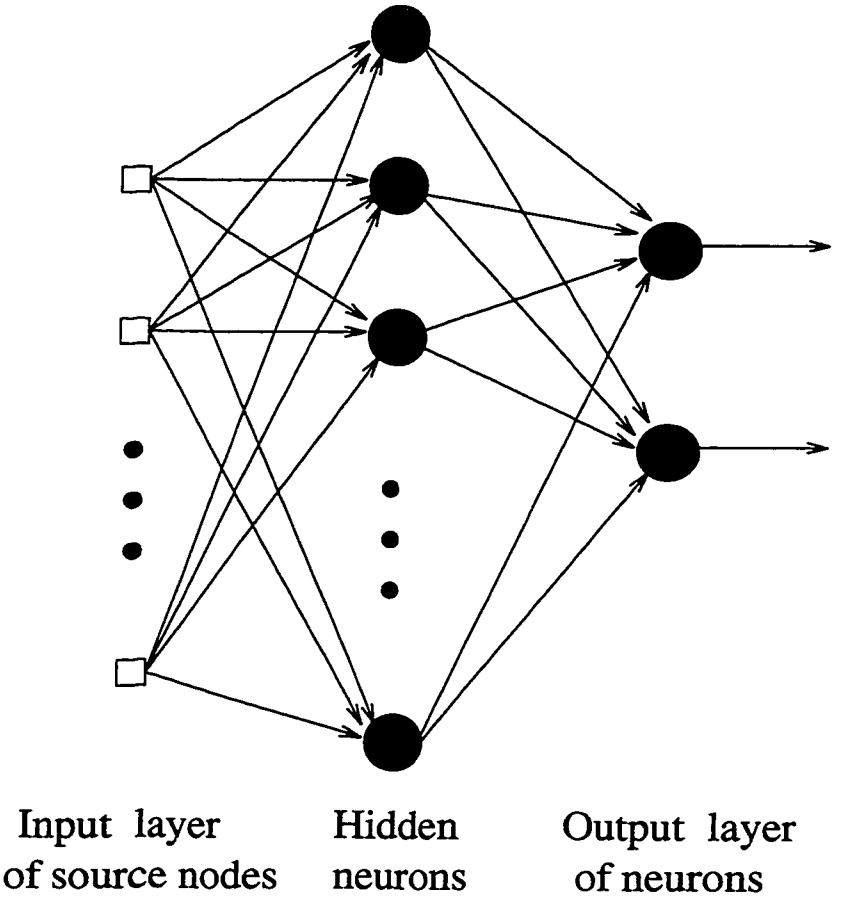

Figure 6.3: Fully connected feedforward network with one hidden layer and output.

and to improve its performance through learning. The learning process may be viewed as a "curve fitting" process, and the neural network itself may be considered simply as a nonlinear input-output mapping. A neural network learns about its environment through an iterative process of adjustments applied to its synaptic weights and biases. Ideally, the network becomes more knowledgeable about its environment after each iteration of the learning process.

To be specific, let $w_{kj}(n)$ denote the value of the synaptic weight w_{kj} at time n. At time n an adjustment $\Delta w_{kj}(n)$ is applied to the weight $w_{kj}(n)$, yielding the updated value $w_{kj}(n+1)$. We may thus write

$$w_{kj}(n+1) = w_{kj}(n) + \Delta w_{kj}(n) \tag{6.13}$$

The adjustment $\Delta w_{kj}(n)$ is computed as a result of stimulation by the environment, and the updated value $w_{kj}(n+1)$ defines the change made in the network as a result of this stimulation. The response of the new network, operating with the updated set of weights $\{w_{kj}(n+1)\}$, is reevaluated.

Typically, the actual response $y_k(n)$ of neuron k is different from the desired response $d_k(n)$. We may define an error signal as the difference between the desired response $d_k(n)$ and the actual response $y_k(n)$, as shown by

$$e_k(n) = d_k(n) - y_k(n) \tag{6.14}$$

The purpose of error-correction learning is to minimize a cost function based on the error signal $e_k(n)$, such that the actual response of each output neuron in the

network approaches the desired response for that neuron. Once a cost function is selected, error-correction learning is strictly an optimization problem to which the usual tools may be brought to bear. A criterion for the cost function is the instantaneous sum of squared errors

$$\mathcal{E}(n) = \frac{1}{2} \sum_{k \in C} e_k^2(n) \tag{6.15}$$

where the set C includes all the neurons in the output layer of the network. Let N denote the total number of examples contained in the training set. The average squared error is obtained as

$$\mathcal{E}_{av} = \frac{1}{N} \sum_{n=1}^{N} \mathcal{E}(n) \tag{6.16}$$

The instantaneous sum of error squares $\mathcal{E}(n)$, and therefore the average squared error $\mathcal{E}_{av}$, is a function of all the synaptic weights and biases of the network. The network is then optimized by minimizing $\mathcal{E}_{av}$ with respect to the synaptic weights of the network. Error-correction learning relies on the error signal $e_k(n)$ to compute the correction $\Delta w_{kj}(n)$ applied to the synaptic weight $w_{kj}(n)$ of neuron k, as shown by

$$\Delta w_{kj}(n) = \eta e_k(n) x_j(n) \tag{6.17}$$

where η is a positive constant that determines the rate of learning.

The error back-propagation algorithm is based on the error-correction learning. Basically, the error back-propagation process consists of two passes through the different layers of the network: a forward pass and a backward pass. In the forward pass, an input vector is applied to the sensory nodes of the network, and

its effect propagates through the network, layer by layer. Finally, a set of outputs is produced as the actual response of the network. During the forward pass the synaptic weights of the network are all fixed. During the backward pass, on the other hand, the synaptic weights are all adjusted in accordance with the error-correction rule. The error signal is propagated backward through the network, against the direction of synaptic connections. The synaptic weights are adjusted so as to make the actual response of the network move closer to the desired response. The error back-propagation algorithm is discussed in [64].

A multilayer neural network trained with the back-propagation algorithm may be viewed as a practical vehicle for performing a nonlinear input-output mapping of a general nature. The universal approximation theorem [64] states that a single hidden layer is sufficient to uniformly approximate any continuous function $f(\cdot)$ with support in a unit hypercube. The approximate realization of the function $f(\cdot)$ is defined as

$$F(x_1, \cdots, x_p) = \alpha_0 + \sum_{k=1}^{M} \alpha_k \varphi(v_k) \tag{6.18}$$

where the network has p input nodes and a single hidden layer consisting of M neurons, the inputs are denoted by $[x_1 \cdots x_p]'$. The activation function $\varphi(v_k)$ is defined in (6.12), the hidden neuron k has synaptic weights $w_{k1}, \cdots, w_{kp}$ and bias b_k as defined in (6.10). The network output is a linear combination of the outputs of the hidden neurons, with α_0 and $\alpha_1, \cdots, \alpha_M$ defining the coefficients of this combination [64, 65]. Eq. (6.18) is the general expression for the scattering parameters and transfer function of the three-port model, *i.e.*, $F(x_1, \cdots, x_p)$ represents $|S_{11}|$, $|S_{21}|$,

$|H|$, $\phi_{S_{11}}$, $\phi_{S_{21}}$, or ϕ_H, respectively.

6.4 Three-Port Electrical and Optical Model for $LiTaO_3$ Probe with CPW Test Structure

The full wave simulation is proceeded for the selected cases (Table 6.1) to cover the entire interested input range. The scattering parameters and transfer functions for the cases are obtained through full wave simulations. The combination of the inputs to the full wave simulation and the corresponding outputs from the full wave simulation for each individual case is taken as a training example to be presented to the neural network. The neural network structure for the three-port model is shown in Fig. 6.4. Based on the set of examples, the input-output mapping is carried out using back-propagation algorithm in MATLAB Application Toolbox - Neural Network [65], and the three-port electrical and optical model of the $LiTaO_3$ probe with CPW test structure is constructed.

In a recently reported automated electro-optic probing system [46], the probe distance is precisely controlled at $3\mu m$ and its position is encoded by the optical scale with an accuracy of $0.1\mu m$ for accurate and reproducible measurement. Also, the probe tip can be moved in the XY plane by step-motor stages in increments of $0.5\mu m$. Based on this equipment, the input validation range is selected as shown in Table 6.2 so that the three-port electrical and optical model can accommodate

Case	CPW center conductor $w(\mu m)$	CPW spacing $s(\mu m)$	Probe distance $h(\mu m)$
1	10	5	2
2	10	10	2
3	10	15	2
4	15	5	2
5	15	10	2
6	15	15	2
7	20	5	2
8	20	10	2
9	20	15	2
10	10	5	7
11	10	10	7
12	10	15	7
13	15	5	7
14	15	10	7
15	15	15	7
16	20	5	7
17	20	10	7
18	20	15	7

Table 6.1: Full wave simulation cases.

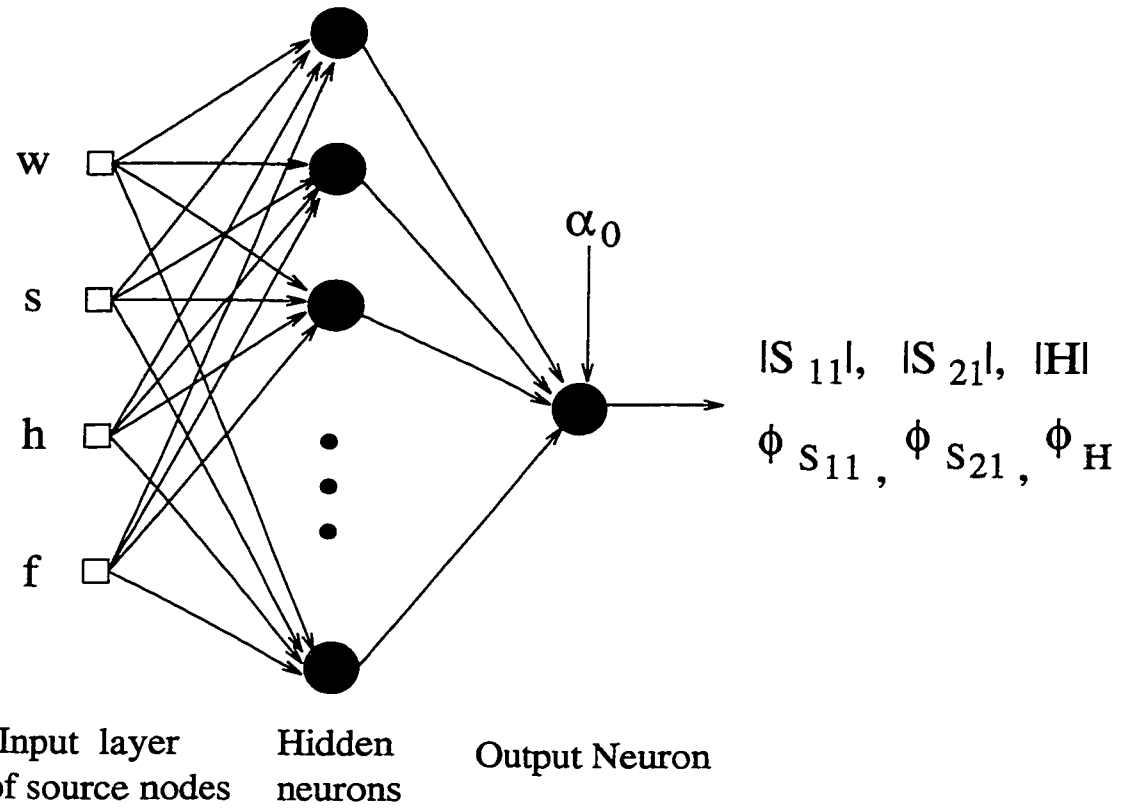

Figure 6.4: Neural network structure for the three-port model. For the input layer of source nodes, W is the width of CPW center conductor, s is the CPW spacing, h is the probe distance, and f is the operation frequency. For the output layer, S represents the scattering parameter, H represents the transfer function, and ϕ represents the corresponding phase of the scattering parameters and transfer function.

Input	physical parameter	Scaling unit	Validation range
x_1	CPW center conductor (w)	10^{-4} m	0.1×10^{-4} m — 0.2×10^{-4} m
x_2	CPW spacing (s)	10^{-4} m	0.05×10^{-4} m — 0.15×10^{-4} m
x_3	Probe distance (h)	10^{-4} m	0.02×10^{-4} m — 0.07×10^{-4} m
x_4	Signal frequency (f)	10^{12} Hz	0.02×10^{12} Hz — 0.1×10^{12} Hz

Table 6.2: Definition of the inputs to the neural network.

most external electro-optic probing systems. To ensure that the inputs to the neural networks are in a unit hypercube, the unit for each input variable is specially selected to meet the requirement. The definition of the inputs to the neural networks is listed in Table 6.2. The synaptic weights, biases, and coefficients in the approximation function (6.18) are then obtained through the mapping and are given in the following. By substituting these weighting parameters into (6.10), (6.12), and (6.18), $|S_{11}|$, $|S_{21}|$, $|H|$, $\phi_{S_{11}}$, $\phi_{S_{21}}$, or ϕ_H can be calculated respectively.

The weights, biases, and coefficients for the amplitude of S_{11}, or $|S_{11}|(dB)$, are listed in the following.

$$\mathbf{W} = \begin{bmatrix} 4.8585 & -6.6984 & -15.5367 & -13.6453 \\ -4.5503 & 7.0950 & 9.7614 & -16.4106 \\ -1.5169 & -16.2865 & -16.3818 & 0.4380 \\ 1.6293 & 2.8571 & 6.9304 & 32.7183 \\ -4.9442 & 8.6553 & -12.5205 & -10.8279 \\ -3.4552 & -0.1494 & 8.0707 & 22.6670 \\ 0.4375 & -3.6009 & -18.6755 & -20.5359 \\ -7.0084 & 7.6755 & -10.9240 & 3.4527 \\ -10.7485 & -0.6391 & 9.1997 & -3.3141 \\ -6.2846 & -1.5276 & -24.1670 & -3.0649 \\ -2.7441 & -3.3285 & 18.4234 & -8.8970 \\ -0.3041 & 5.8127 & -30.1657 & 5.6501 \end{bmatrix} \tag{6.19}$$

$$\mathbf{B} = \begin{bmatrix} -2.8971 \\ -5.0426 \\ 1.6547 \\ -0.4977 \\ -3.9081 \\ 3.8748 \\ -2.6771 \\ -3.0938 \\ 0.3874 \\ 1.7132 \\ 0.5713 \\ 6.1075 \end{bmatrix} \tag{6.20}$$

$$\boldsymbol{\alpha} = [4.4237 \quad 8.8738 \quad -5.9085 \quad 21.9294 \quad 6.1193 \quad -7.0430 \quad 5.8545$$
$$7.1234 \quad -7.4777 \quad 8.3919 \quad -7.6682 \quad -5.9655] \tag{6.21}$$

$$\alpha_0 = -9.7234 \tag{6.22}$$

An example of the amplitude of $S_{11}(dB)$ is plotted in Fig. 6.5.

The weights, biases, and coefficients for the phase of S_{11}, or $\phi_{S_{11}}(degree)$, are listed in the following.

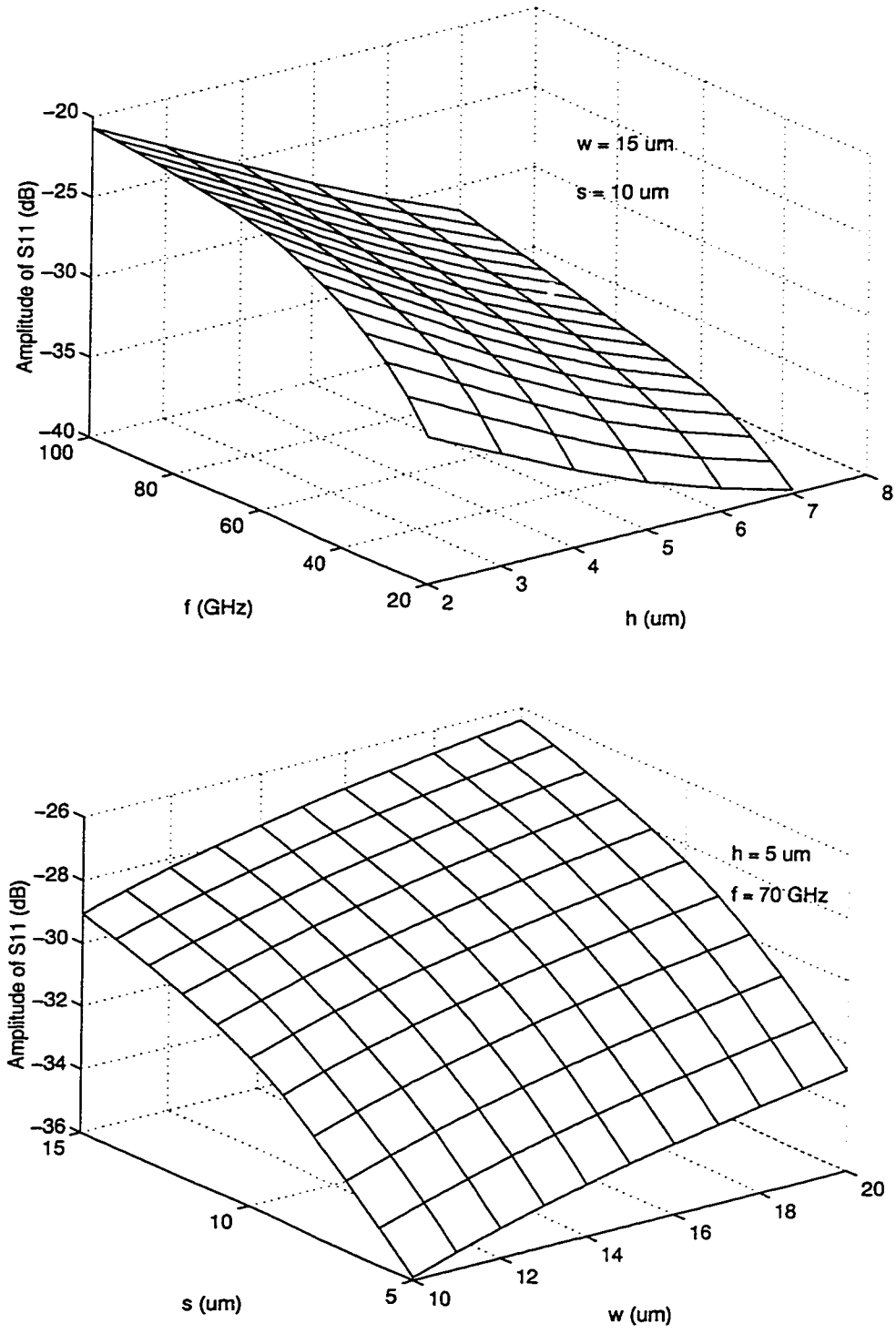

Figure 6.5: Example of the amplitude of S_{11} in three-port electrical and optical model.

$$\mathbf{W} = \begin{bmatrix} 5.1006 & -5.9632 & -15.4752 & -16.7450 \\ 3.3083 & 4.5492 & 14.8692 & -51.0825 \\ -1.7557 & -9.8598 & -17.7389 & 5.4352 \\ -0.0058 & -0.0026 & 0.9218 & 27.5408 \\ -6.4354 & 9.1100 & -12.3329 & -14.3173 \\ 1.1093 & 1.5074 & 5.4981 & 98.8176 \\ -0.3701 & 0.7032 & -14.6326 & -45.5857 \\ -7.5815 & 7.9596 & -10.7810 & 3.2181 \\ -9.7853 & 1.1934 & 6.0693 & 2.9178 \\ -7.4789 & -4.5927 & -22.8090 & 0.7316 \\ 0.0948 & 0.6601 & 23.2378 & -23.3237 \\ -0.3288 & 2.3389 & -26.0515 & 5.8783 \end{bmatrix} \tag{6.23}$$

$$\mathbf{B} = \begin{bmatrix} 1.5185 \\ -1.7053 \\ 5.9427 \\ -2.0800 \\ 1.2912 \\ -0.3704 \\ -0.2522 \\ -3.1626 \\ 3.9908 \\ -0.6143 \\ -0.9124 \\ 0.9467 \end{bmatrix} \tag{6.24}$$

$$\boldsymbol{\alpha} = [3.0452 \quad 31.7190 \quad 12.4018 \quad 34.3317 \quad 4.1910 \quad -67.3561 \quad 20.7916$$

$$-10.7838 \quad 16.3590 \quad -12.8074 \quad -9.0561 \quad -13.5861] \tag{6.25}$$

$$\alpha_0 = 6.9689 \tag{6.26}$$

An example of the phase of $S_{11}(degree)$ is plotted in Fig. 6.6.

The weights, biases, and coefficients for the amplitude of S_{21}, or $|S_{21}|(dB)$, are listed in the following.

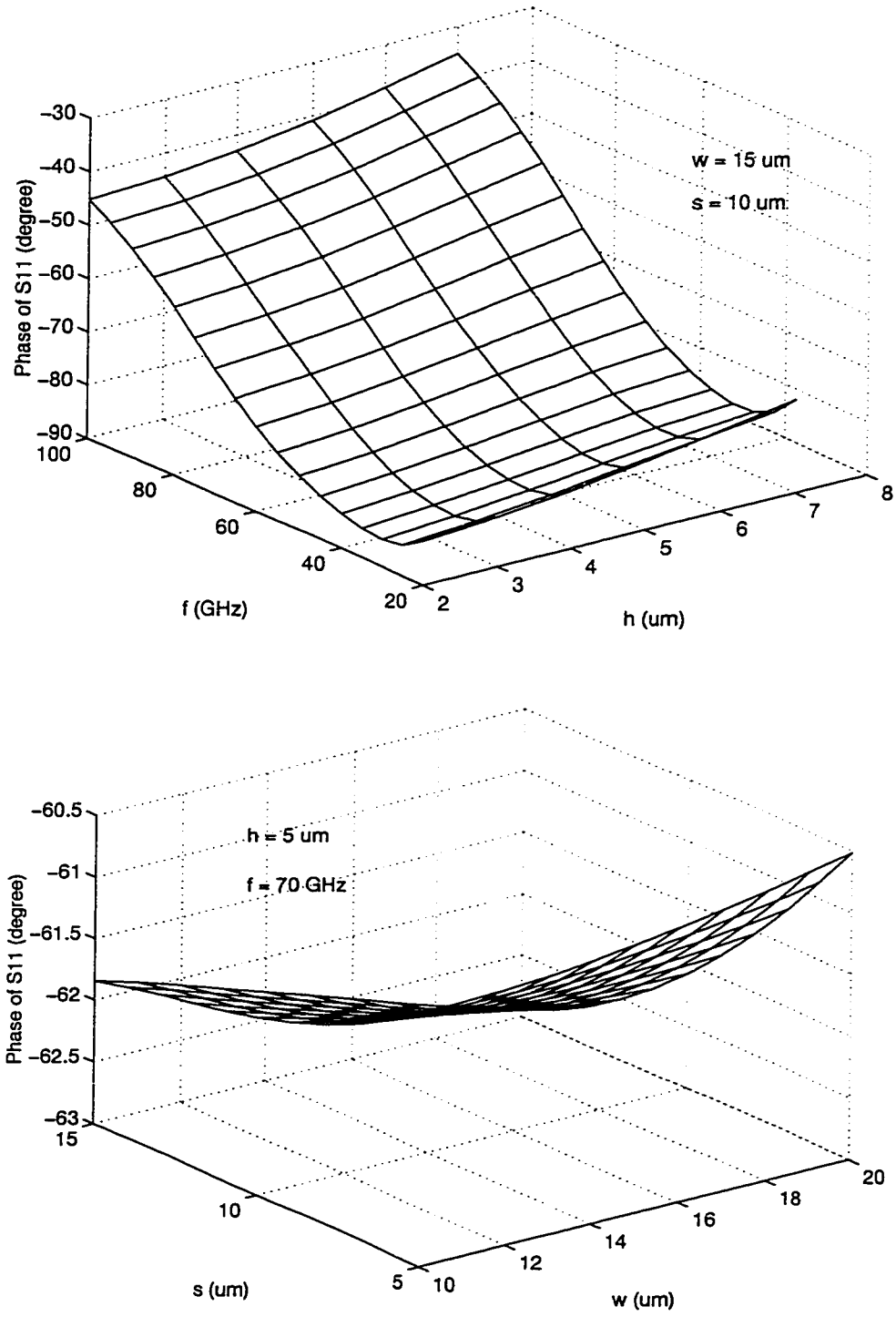

Figure 6.6: Example of the phase of S_{11} in three-port electrical and optical model.

$$\mathbf{W} = \begin{bmatrix} -0.7500 & -9.2174 & -5.4121 & 17.0048 \\ -4.4481 & -9.8494 & 3.1017 & 16.0491 \\ -0.1716 & -10.3695 & -2.9161 & 19.1429 \\ -2.5728 & 10.7608 & 22.7197 & 1.7280 \\ 9.9949 & -5.3672 & -2.0869 & 6.1883 \\ -5.6933 & 3.8333 & 18.8067 & 16.6098 \\ 7.2059 & 2.5785 & -10.0641 & -19.0416 \\ 6.3055 & -4.7886 & 4.2098 & -18.7788 \\ 6.0728 & 7.8330 & 16.2056 & 10.1950 \\ 4.9444 & 7.6068 & 22.4840 & -10.1883 \\ 6.6138 & 4.2186 & -23.9004 & 2.5915 \\ 4.2030 & 0.4186 & 27.8457 & 13.7999 \\ -6.8780 & -10.3584 & -2.1349 & 4.8773 \\ -0.3959 & -10.3413 & -22.2519 & -6.8709 \\ 0.7984 & 11.0643 & 20.7736 & 4.6747 \end{bmatrix} \tag{6.27}$$

$$\mathbf{B} = \begin{bmatrix} 1.4034 \\ 0.8340 \\ 1.3027 \\ -4.3334 \\ -1.5322 \\ -1.5405 \\ 0.4758 \\ 1.4217 \\ -3.2971 \\ -3.3806 \\ -1.2763 \\ -3.5099 \\ 3.7264 \\ 1.9707 \\ -3.6559 \end{bmatrix} \tag{6.28}$$

$$\begin{aligned} \boldsymbol{\alpha} = [&0.8638 \quad -0.0763 \quad -0.6588 \quad -0.1217 \quad 0.0205 \quad 0.0697 \quad 0.0406 \quad 0.0123 \\ &-0.0400 \quad 0.1610 \quad -0.1001 \quad -0.0092 \quad -0.0634 \quad 0.0068 \quad -0.0240] \end{aligned} \tag{6.29}$$

$$\alpha_0 = -0.1611 \tag{6.30}$$

An example of the amplitude of $S_{21}(dB)$ is plotted in Fig. 6.7.

The weights, biases, and coefficients for the phase of S_{21}, or $\phi_{S_{21}}(degree)$, are listed in the following.

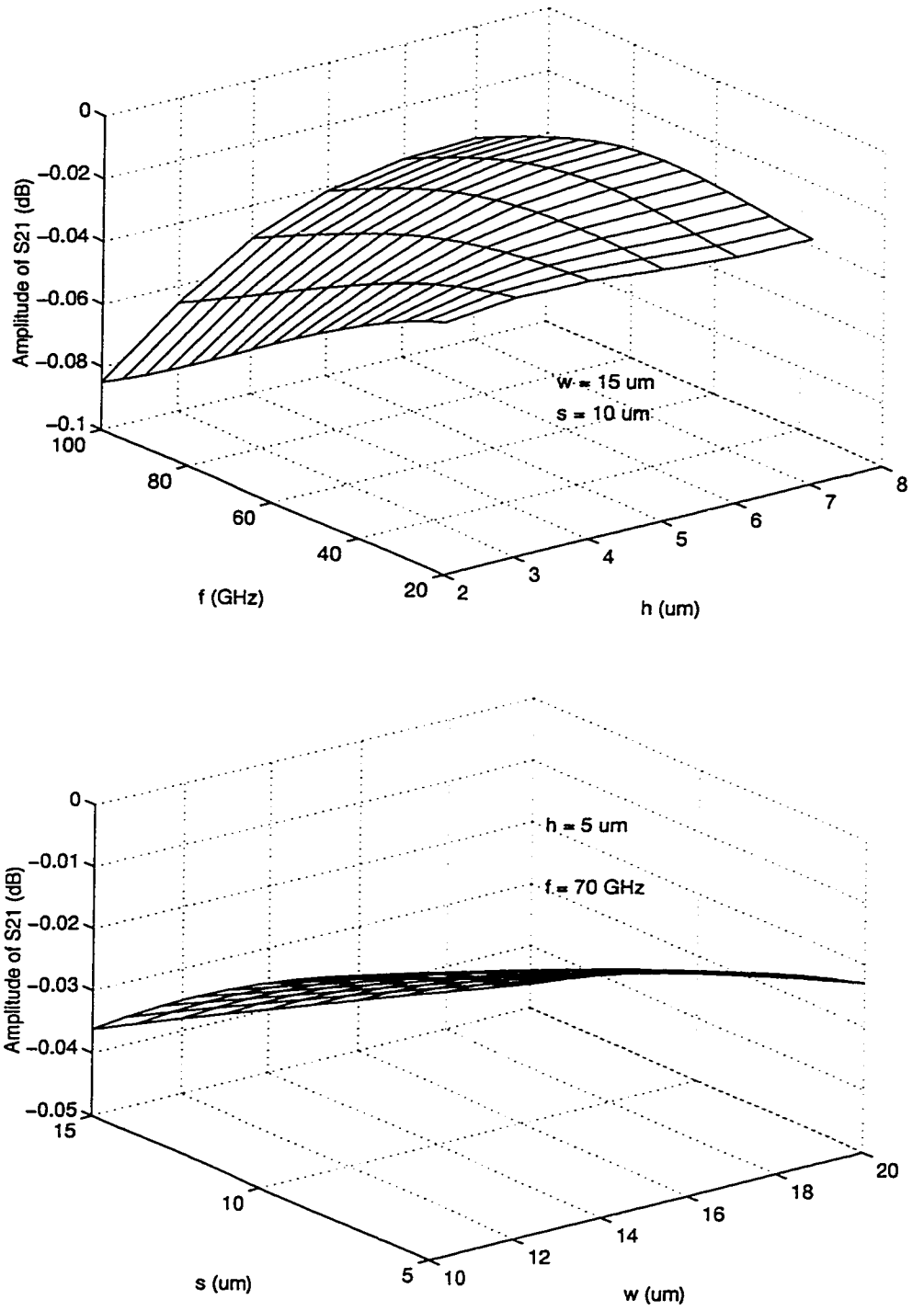

Figure 6.7: Example of the amplitude of S_{21} in three-port electrical and optical model.

$$\mathbf{W} = \begin{bmatrix} 5.9419 & -5.9183 & -15.0622 & -13.2263 \\ -1.0973 & 1.2897 & 4.9024 & -26.2820 \\ -1.6500 & -10.1781 & -17.7104 & 4.7051 \\ -0.7383 & -0.4326 & -1.0229 & 37.6931 \\ -7.3650 & 6.8150 & -10.4556 & -12.0078 \\ -7.9989 & 0.3768 & 11.3518 & 24.3107 \\ 3.7289 & -0.2240 & -10.6885 & -27.9625 \\ -10.2633 & 8.7427 & -10.5760 & 0.3384 \\ -10.4836 & 0.2266 & 5.5813 & 2.4200 \\ -7.0622 & -4.6731 & -22.8590 & 0.4265 \\ -3.2912 & 3.0826 & 27.7525 & -11.2930 \\ -0.1600 & 5.8982 & -30.3274 & 4.6180 \end{bmatrix} \tag{6.31}$$

$$\mathbf{B} = \begin{bmatrix} 5.2867 \\ 2.3269 \\ 6.1742 \\ -1.4844 \\ 2.6418 \\ -3.0740 \\ 2.2340 \\ 3.4377 \\ -3.8487 \\ -1.3236 \\ 0.4358 \\ 4.1426 \end{bmatrix} \tag{6.32}$$

$$\boldsymbol{\alpha} = [3.6324 \quad -12.2253 \quad 6.3529 \quad 9.9045 \quad -4.5807 \quad 14.0178 \quad -6.5951$$

$$4.4937 \quad -7.4962 \quad -5.9889 \quad 3.4502 \quad 7.0662] \tag{6.33}$$

$$\alpha_0 = 7.4058 \tag{6.34}$$

An example of the phase of $S_{21}(degree)$ is plotted in Fig. 6.8.

The weights, biases, and coefficients for the amplitude of the normalized transfer function H, or $|H|(dB)$, are listed in the following.

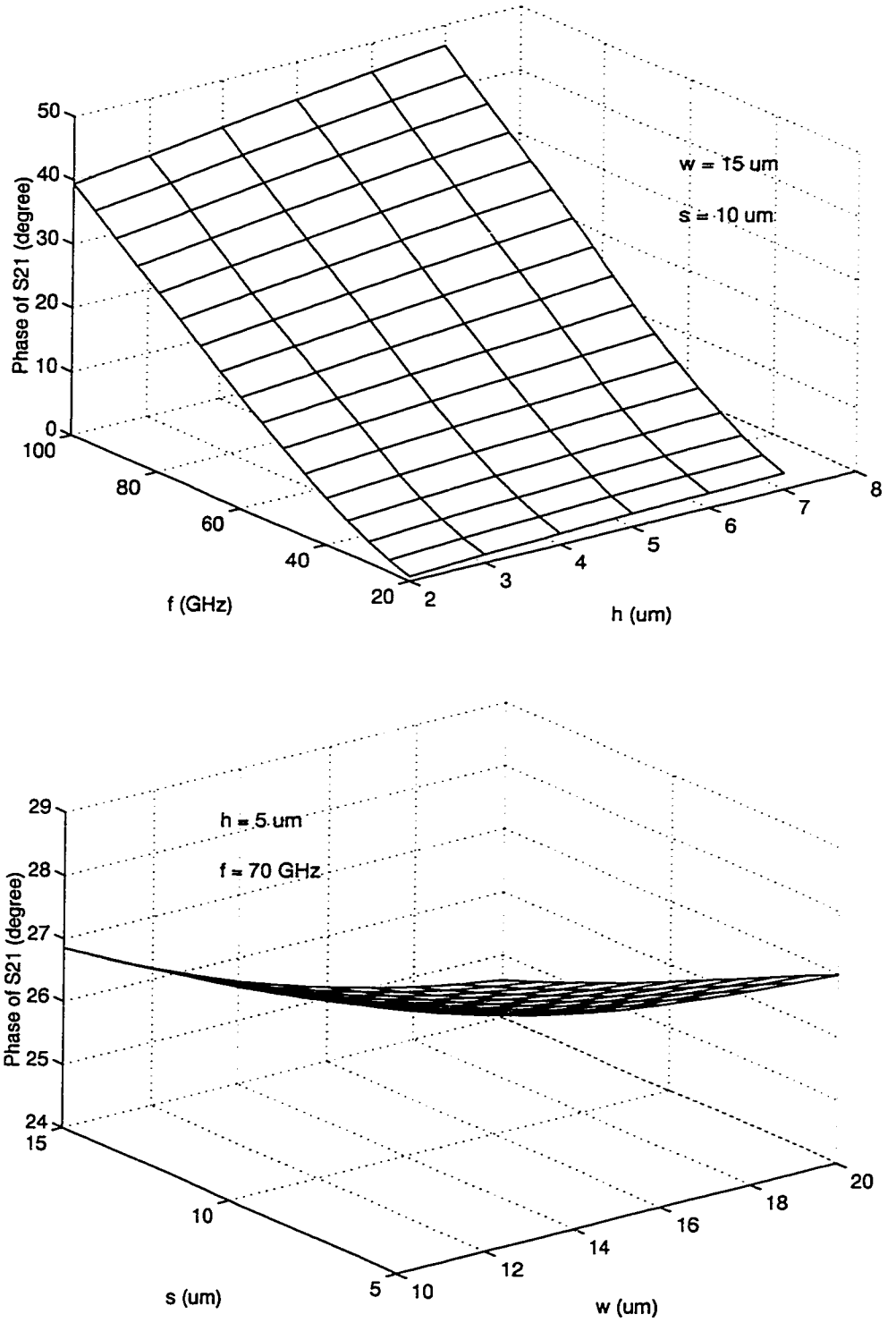

Figure 6.8: Example of the phase of S_{21} in three-port electrical and optical model.

$$\mathbf{W} = \begin{bmatrix} 4.5636 & -7.8380 & -14.7526 & -13.4622 \\ -4.3947 & 7.2476 & 9.7073 & -16.3404 \\ -10.7548 & -14.8335 & -15.7903 & 0.2730 \\ 0.2769 & 4.7466 & -3.1000 & 19.4241 \\ -4.9879 & 10.5404 & -12.3648 & -10.2457 \\ -5.4520 & 0.3450 & 8.1404 & 22.1068 \\ 1.4169 & -2.8134 & -19.4808 & -19.9990 \\ -11.5827 & 10.0793 & -9.2367 & 0.9638 \\ -18.9271 & 2.9939 & 6.2694 & 0.9083 \\ -4.6845 & -6.7945 & -23.6043 & -2.2472 \\ -5.1700 & 1.2950 & 28.1711 & -4.7786 \\ 0.2448 & 7.8315 & -32.0030 & 2.1171 \end{bmatrix} \tag{6.35}$$

$$\mathbf{B} = \begin{bmatrix} 1.2531 \\ -4.9522 \\ 2.6059 \\ -0.4425 \\ 0.5791 \\ 2.3920 \\ 0.0164 \\ 0.9497 \\ 2.3990 \\ 4.9041 \\ 0.3955 \\ -0.2326 \end{bmatrix} \tag{6.36}$$

$$\boldsymbol{\alpha} = [0.8883 \quad 4.0170 \quad -8.7165 \quad 1.1373 \quad 0.4598 \quad -2.0308 \quad 2.6331$$
$$8.4991 \quad -4.7907 \quad -1.6568 \quad -3.2906 \quad 2.1366] \tag{6.37}$$

$$\alpha_0 = -4.5440 \tag{6.38}$$

An example of the amplitude of the normalized transfer function $H(dB)$ is plotted in Fig. 6.9.

The weights, biases, and coefficients for the phase of the normalized transfer function H, or $\phi_H(degree)$, are listed in the following.

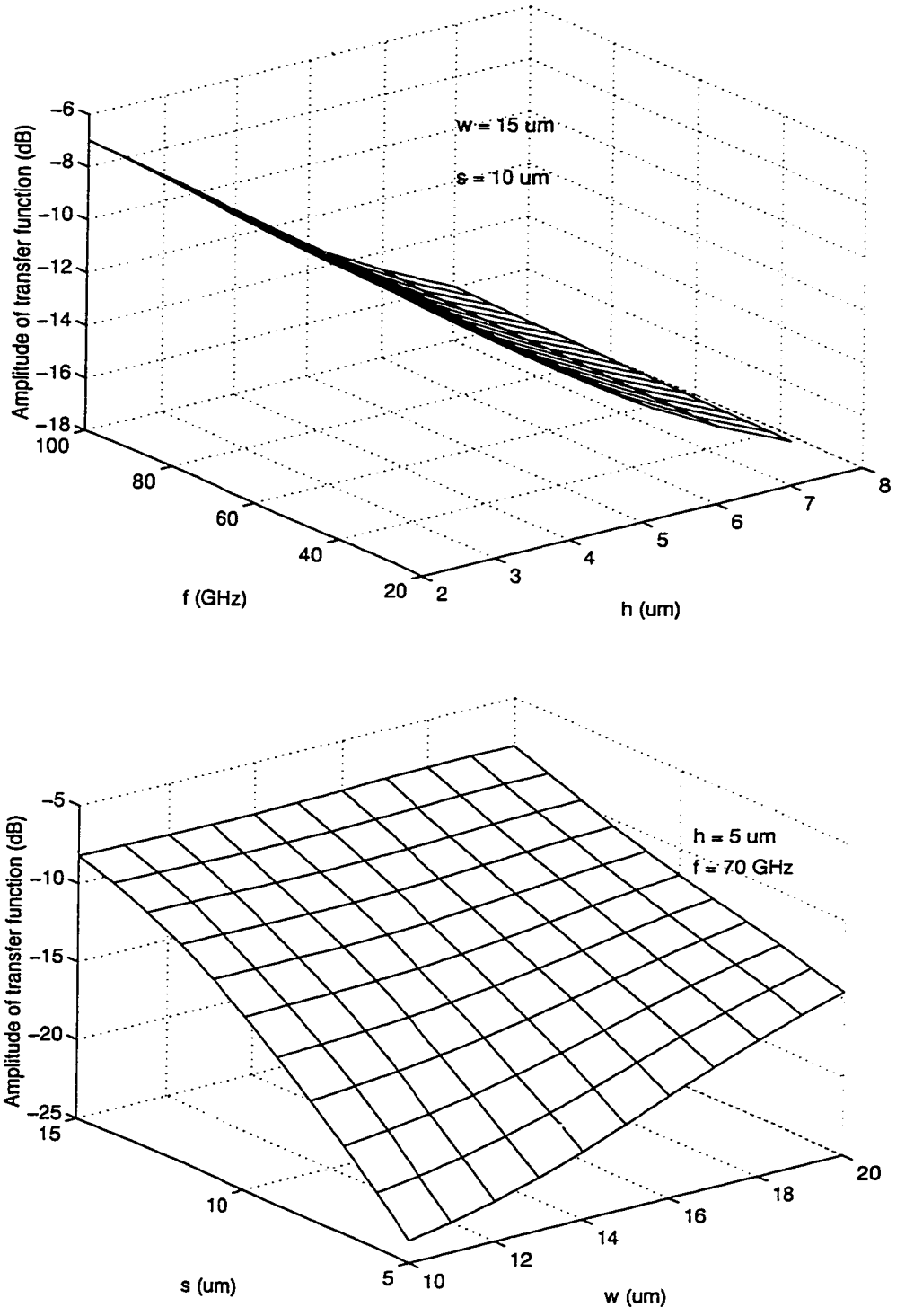

Figure 6.9: Example of the amplitude of the transfer function in three-port electrical and optical model.

$$\mathbf{W} = \begin{bmatrix} 1.9789 & -11.7136 & 19.0529 & -5.3139 \\ -10.2352 & -7.7410 & -1.1647 & 12.0823 \\ -1.9434 & -7.7360 & -10.5842 & -11.9775 \\ -3.5331 & -0.6128 & 24.0772 & -3.9410 \\ -7.6747 & -8.3865 & -0.7172 & -8.5479 \\ -3.5406 & 17.5667 & -13.8442 & 0.6863 \\ -4.5227 & -6.7197 & 12.8402 & -15.6511 \\ -4.0457 & 8.5139 & 15.7505 & -6.9680 \end{bmatrix} \tag{6.39}$$

$$\mathbf{B} = \begin{bmatrix} 1.1384 \\ 1.9182 \\ 2.6078 \\ -0.1067 \\ 1.8082 \\ -2.0746 \\ 3.0355 \\ 0.2445 \end{bmatrix} \tag{6.40}$$

$$\boldsymbol{\alpha} = [6.2758 \quad -0.8400 \quad -1.5749 \quad -2.8974 \quad 1.8454 \quad 4.3074 \quad 3.8362 \quad 3.1925] \tag{6.41}$$

$$\alpha_0 = -5.1512 \tag{6.42}$$

An example of the phase of the normalized transfer function $H(degree)$ is plotted in Fig. 6.10.

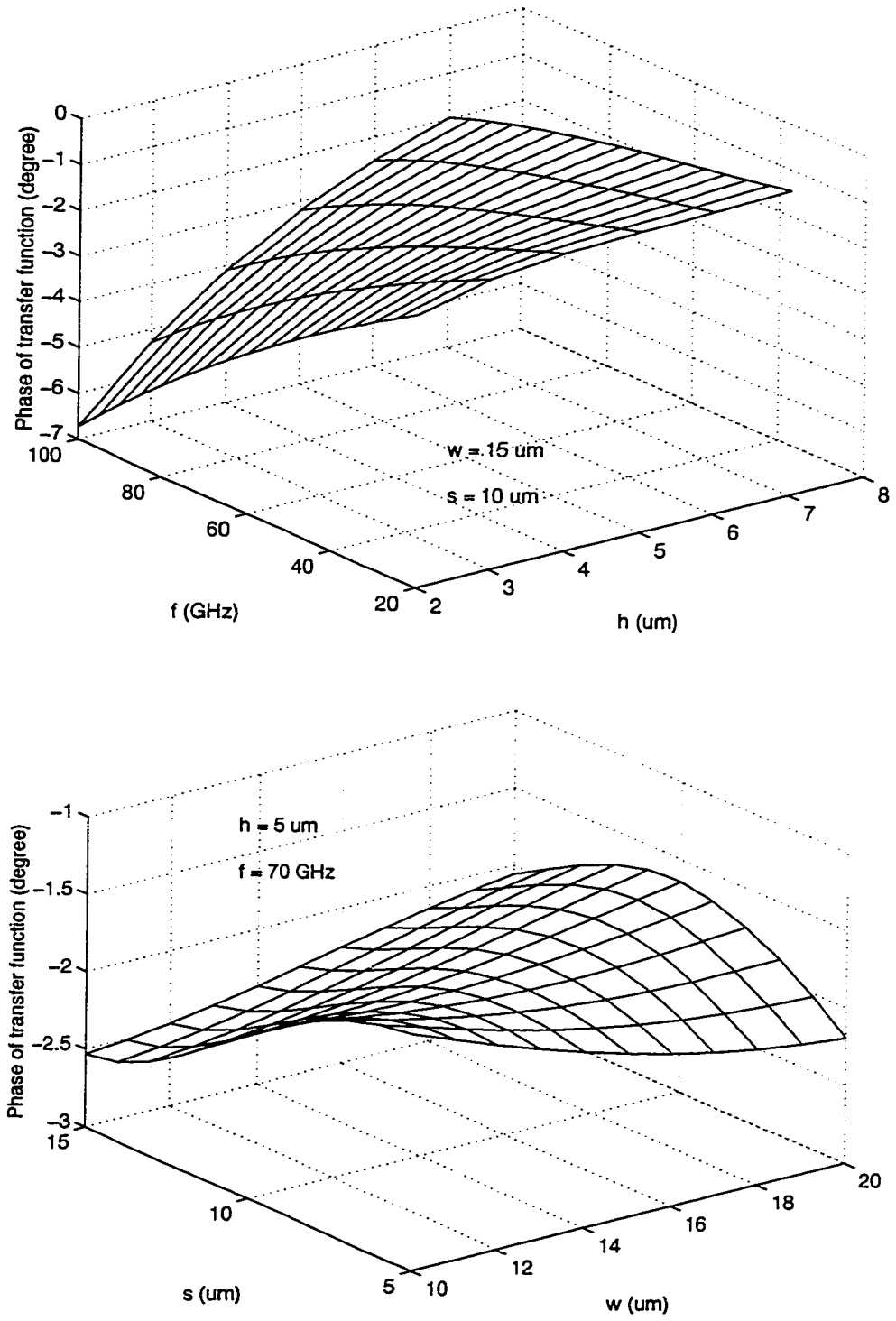

Figure 6.10: Example of the phase of the transfer function in three-port electrical and optical model.

6.5 Application of Three-Port model to Electro-Optic High-Speed Measurement

The external electro-optic sampling measurement shows promising results in its high frequency capability and small invasive property in measurement at internal circuits on MMICs and other high speed devices [46, 66]. The purpose of the calibration is to de-embed invasiveness and distortion caused by the probe, which are the two major issues for accurate and reliable measurement. The field based three-port model developed in this chapter enables the fast and effective calibration by means of network connection and system transfer function.

Scattering parameters are among the most important parameters of microwave and millimeter-wave devices and circuits. Almost all the linear circuit designs are made in the frequency domain by means of scattering parameters. In the calibration scheme of Fig. 6.11 for scattering parameters, the three-port model for the $LiTaO_3$ probe with CPW test structure is considered to connect to the device under test. The measured scattering parameters are from the two connected networks. Then the scattering parameters of the device under test can be calculated from the measured scattering parameters and the scattering parameters of the three-port model [45]. Such a procedure can effectively de-embed the probe invasiveness and the dispersion of CPW test structure.

One of the important applications of the probe transfer function is to correct

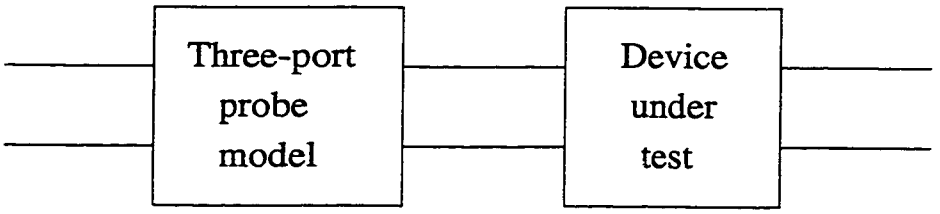

Figure 6.11: Calibration scheme for scattering parameters.

the waveform distortion in electro-optic sampling. The probing system transfer function $H(\omega)$ can be found from the three-port model in terms of the specific physical parameters of the test structure. Then, the unknown electric input $e_{CPW}(t)$ at the sampling spot corresponding to the measured optical retardation $\Gamma(t)$ can be determined by

$$e_{CPW}(t) = \mathcal{F}^{-1}\left[\frac{\Gamma(\omega)}{H(\omega)}\right] \tag{6.43}$$

where $\mathcal{F}^{-1}$ represents the inverse Fourier transform. Using (6.43), the probing distortion, CPW's dispersion and other parasitic effects with the system can be calibrated.

To demonstrate the waveform calibration by means of the probe transfer function, a simulation (Fig. 6.12) is made to verify the proposed calibration technique. In the simulation, a Gaussian pulse is launched down to the CPW which is shown as the solid line in Fig. 6.12. The optical output shown as the dashed line in Fig. 6.12 is found by the full wave simulation incorporated with E-O effect calculation. Using the probe transfer function obtained from the three-port model, the calibrated electric waveform on the CPW is determined by (6.43). The excellent agreement between the original electric input and the calibrated optical output

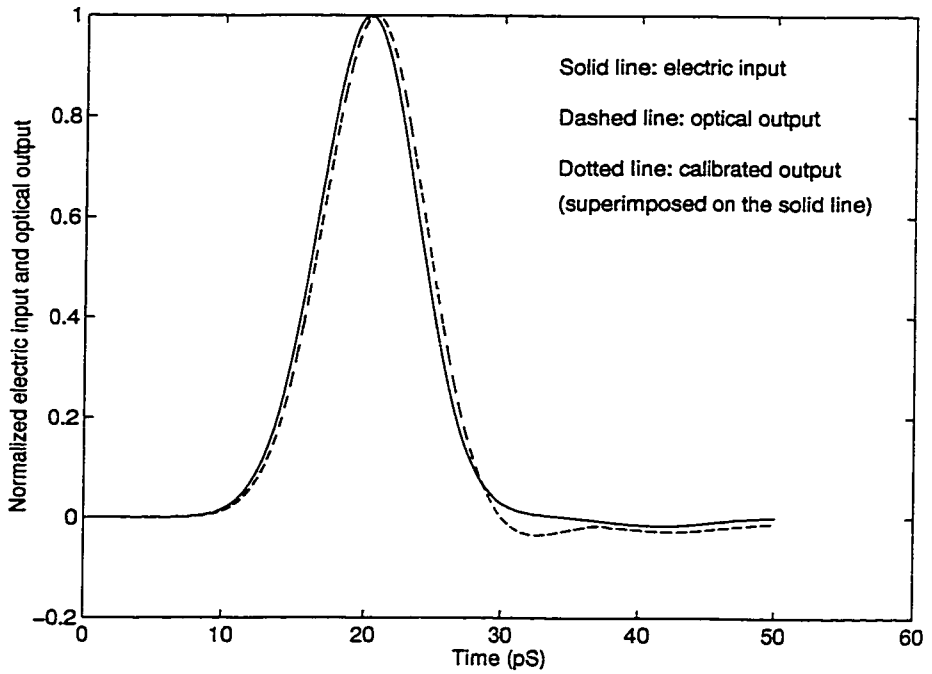

Figure 6.12: Comparison for the electric input, optical output, and calibrated output. The excellent agreement between solid line and dotted line confirms the calibration technique and the three-port model.

(dotted line, superimposed on the solid line) confirms the validity of the three-port model.

6.6 Concluding Remarks

A three-port field-based electrical and optical model for $LiTaO_3$ probe with CPW test structure is developed by combining full wave electromagnetic modeling technique and neural network techniques. It allows the probe test structure to be characterized fast and accurately without time-consuming full wave simulations. It is proved to be an effective calibration tool to de-embed the invasiveness and signal distortion caused by the probe. It can be used for the on-line calibration in electro-optic measurement systems.

Chapter 7

Conclusions

7.1 Contributions

This thesis has contributed an equivalent circuit microcavity model for the modeling of vertical cavity surface emitting lasers. The main contribution with the microcavity model is that a negative nonlinear resistance is derived to represent the optical gain in the cavity, which results in the estimation of the frequency chirping and is much easier than other equivalent circuit models. The model is used to analyze microcavities in both time and frequency domains in terms of material and physical parameters of the lasers, and provides a simple and fast way to optimize the cavity length, reflective mirror and active region of the lasers.

This thesis has also established a simplified three-dimensional microcavity

model with the effective mirror to replace the quarter-wave stack. The FD-TLM method is modified to include the three-dimensional distributed optical gain region in the simulation. The near-field and far-field distribution of the circular laser beam provides a guide for the design of the interconnection of optical components in fiber communication systems.

This thesis has contributed a dynamic equivalent circuit model for vertical cavity surface emitting lasers to the equivalent circuit family of lasers. The main contributions in the development of the dynamic equivalent circuit model are:

(a) The dynamic equivalent circuit model is established using two coupled circuits to couple the microcavity model to the rate equations.

(b) The frequency chirping is obtained from the resonant frequencies of microcavities.

(c) The relationship between the photon number and the standing wave in the cavity is derived for the implementation of the circuit coupling.

(d) The spontaneous emission noise source is developed and added to the dynamic equivalent circuit model.

This dynamic equivalent circuit model has advantages over other equivalent circuit models and can be directly connected to the electronic driving circuit so that laser transmitting systems can be modeled in general nonlinear circuit modeling software.

This thesis has successfully applied FD-TLM method to the modeling of the E-O probe with different CPW configurations. A new transfer function for the E-O probe with CPW test structure is defined to directly sample the signal on

the sampling point. The scattering parameters and transfer function versus CPW dimensions are reported in this thesis for the first time.

This thesis has contributed a three-port electrical and optical model with scattering parameters and transfer function as its characteristic functions for the $LiTaO_3$ probe with CPW test structure to the electro-optic sampling measurement category. With this model, both the probe invasiveness and the signal distortion can be de-embedded. This field based three-port model has the same accuracy as the full wave modeling but it is much faster and simpler to use than the full wave modeling so that it makes the on-line calibration of E-O sampling systems possible and practical.

7.2 Future Research

The dynamic equivalent circuit model for VCSEL lays a foundation of a class of laser models. The laser equivalent circuit models for other kinds of semiconductor laser devices can be established based on the model introduced in this thesis. Although the linear gain model is used in this dynamic equivalent circuit model, further research can be devoted to using more complex gain models to study the effects related with different gain models. Future research can also be related to the investigation of laser noise performance, modulation performance, linewidth, and frequency chirp *etc.* based on the model developed in this thesis. The performance evaluation of laser transmitting systems in fiber communication can be carried out

using the dynamic equivalent circuit model introduced in this thesis.

Future research for E-O sampling measurement can be considered in the modeling of the entire system including laser source, E-O probe, polarizer and polarization analyzer, wave plates, and photodetectors *etc.*. Efforts can be devoted to the application of the full wave modeling method to direct and hybrid E-O sampling problems, more general devices such as MMIC, and more complex circuit configurations. Further research can also be devoted to the design and calibration of the ultrahigh-frequency vector network analyzer by combining the E-O sampling equipment and the conventional vector network analyzer.

Bibliography

[1] P. L. Gourley, K. L. Lear, and R. P. Schneider Jr., "A different mirror ...," *IEEE Spectrum*, vol. 31, No. 8, pp. 31-37, Aug. 1994.

[2] Y. Yamamoto and R. E. Slusher, "Optical processes in microcavities," *Physics Today*, pp. 66-73, June 1993.

[3] G. A. Evans and J. M. Hammer, *Surface Emitting Semiconductor Lasers and Arrays*. Boston: Academic Press, 1993.

[4] S. A. Basinger and D. J. Brady, "Finite-difference time-domain modeling of dispersive nonlinear Fabry-Perot cavities," *J. Opt. Soc. Am. B*, vol. 11, No. 8, pp. 1504-1511, Aug. 1994.

[5] T. Baba, T. Hamano, F. Koyama, and K. Iga, "Spontaneous emission factor of a microcavity DBR Surface-emitting laser," *IEEE J. Quantum Electron.*, vol. 27, No. 6, pp. 1347-1358, June 1991.

[6] G. P. Agrawal and N. K. Dutta, *Semiconductor Lasers*. New York: Van Nostrand Reinhold, 1993.

[7] D. S. Gao, S. M. Kang, R. P. Bryan, and J. J. Coleman, "Modeling of quantum-well lasers for computer-aided analysis of optoelectronic integrated circuits," *IEEE J. Quantum Electron.*, vol. 26, No. 7, pp. 1206-1216, July 1990.

[8] A. J. Lowery, "New dynamic semiconductor laser model based on the transmission-line modeling method," *IEE Proc.*, vol. 134, Pt. J, No. 5, pp. 281-289, Oct. 1987.

[9] L. M. Zhang, S. F. Yu, M. C. Nowelll, D. D. Marcenac, J. E. Carroll, and R. G. S. Plumb, "Dynamic analysis of radiation and side-mode suppression in a second-order DFB laser using time-domain large-signal traveling wave model," *IEEE J. Quantum Electron.*, vol. 30, No. 6, pp. 1389-1395, June 1994.

[10] D. M. Pozar, *Microwave Engineering.* Massachusetts: Addison-Wesley, 1990.

[11] J-P. Zhang, "The dynamic properties and stability analysis for vertical-cavity surface-emitting lasers," *IEEE J. Quantum Electron.*, vol. 31, No. 12, pp. 2127-2132, Dec. 1995.

[12] L. A. Zadeh and C. A. Desoer, *Linear System Theory.* New York: McGraw-Hill, 1963.

[13] S-P. Chan, S-Y. Chan, and S-G. Chan, *Analysis of Linear Networks and Systems.* Massachusetts: Addison-Wesley, 1972.

[14] M. Zhang and D. R. Conn, "A transmission line model for vertical cavity surface emitting lasers," *Twentieth International Conference on Infrared and Millimeter Waves*, pp. 329-330, Orlando, Florida, 1995.

[15] M. Zhang and D. R. Conn, "A new transmission line microcavity model for vertical cavity surface emitting lasers," accepted for publication in *International Journal of Infrared and Millimeter Waves.*

[16] J. Zhang and K. Petermann, "Beam propagation model for vertical-cavity surface-emitting lasers: threshold properties," *IEEE J. Quantum Electron.*, vol. 30, No. 7, pp. 1529-1536, July 1994.

[17] R. H. Voelker and R. J. Lomax, "A finite-difference transmission line matrix method incorporating a nonlinear device model," *IEEE Trans. Microwave Theory Tech.*, vol. 38, No. 3, pp. 302-312, March 1990.

[18] M. Zhang, *Finite-difference transmission-line matrix method and its applications.* Master's thesis, McMaster University, Dec. 1993.

[19] P. B. Johns and R. L. Beurle, "Numerical solution of two-dimensional scattering problems using a transmission-line matrix," *Proc. IEE*, vol. 118, No. 9, pp. 1203-1208, Sept. 1971.

[20] K. S. Yee, "Numerical solution of initial boundary value problems involving Maxwell's equations in isotropic media," *IEEE Trans. Antennas Propagat.*, vol. AP-14, pp. 302-307, May 1966.

[21] X. Zhang and K. K. Mei, "Time-domain finite difference approach to the calculation of the frequency-dependent characteristics of microstrip discontinuities," *IEEE Trans. Microwave Theory Tech.*, vol. MTT-36, No. 12, pp. 1775-1787, Dec. 1988.

[22] G. Liang, Y. Liu and K. K. Mei, "Full-wave analysis of coplanar waveguide and slotline using the time-domain finite difference method," *IEEE Trans. Microwave Theory Tech.*, vol. 37, No. 12, pp. 1949-1957, Dec. 1989.

[23] P. B. Johns, "On the relationship between TLM and finite-difference methods for Maxwell's equations," *IEEE Trans. Microwave Theory Tech.*, vol. MTT-35, No. 1, pp. 60-61, Jan. 1987.

[24] W. K. Gwarek, "Comments on 'On the relationship between TLM and finite-difference methods for Maxwell's equations'," and reply by P. B. Johns, *IEEE Trans. Microwave Theory Tech.*, vol. MTT-35, No. 9, pp. 872-873, Sept. 1987.

[25] P. Russer, P. P. M. So, and W. J. R. Hoefer, "Modeling of nonlinear active regions in TLM," *IEEE Microwave and Guided Wave Letters*, vol. 1, No. 1, pp. 10-13, Jan. 1991.

[26] M. Born and E. Wolf, *Principles of Optics.* New York: Pergamon Press, 1977.

[27] C. S. Williams and O. A. Becklund, *Optics.* New York: Wiley-Interscience, 1972.

[28] X. Zeng and A. Naqwi, "Far-field distribution of double-heterostructure diode laser beams," *Applied Optics*, vol. 32, No. 24, pp. 4491-4494, Aug. 1993.

[29] P. M. Goorjian, A. Taflove, R. M. Joseph, and S. C. Hagness, "Computational modeling of femtosecond optical solitons from Maxwell's equations," *IEEE J. Quantum Electron.*, vol. 28, No. 10, pp. 2416-2422, Oct. 1992.

[30] P. M. Goorjian and A. Taflove, "Direct time integration of Maxwell's equations in nonlinear dispersive media for propagation and scattering of femtosecond electromagnetic solitons," *Optics Letters*, vol. 17, No. 3, pp. 180-182, Feb. 1992.

[31] R. M. Joseph, S. C. Hagness, and A. Taflove, "Direct time integration of Maxwell's equations in linear dispersive media with absorption for scattering and propagation of femtosecond electromagnetic pulses," *Optics Letters*, vol. 16, No. 18, pp. 1412-1414, Sept. 1991.

[32] S. Radic and N. George, "Ultrafast pulse propagation in periodic optical media: a generalized finite-difference time-domain approach," *Optics Letters*, vol. 19, No. 14, pp. 1064-1066, July 1994.

[33] J. Buus, "Principles of semiconductor laser modeling," *IEE Proc. J. Optoelectron.*, vol. 132, No. 1, pp. 42-51, Jan. 1985.

[34] R. S. Tucker, "Large-signal circuit model for simulation of injection-laser modulation dynamics," *IEE Proc.*, vol. 128, Pt. I, No. 5, pp. 180-184, Oct. 1981.

[35] H. A. Tafti, K. K. Kamath, G. Abraham, F. N. Farokhrooz, and P. R. Vaya, "Circuit modeling of multimode semiconductor lasers and study of pulse broadening effect," *Electron. Lett.*, vol. 29, No. 16, pp. 1443-1445, Aug. 1993.

[36] J. L. Jewell, A. Scherer, S. L. McCall, Y. H. Lee, S. J. Walker, J. P. Harbison, and L. T. Florez, "Low-threshold electrically pumped vertica-cavity surface emitting microlasers," *Electron. Lett.*, vol. 25, pp. 1123-1124, 1989.

[37] J. L. Jewell, Y. H. Lee, A. Scherer, S. L. McCall, N. A. Olsson, R. S. Tucker, C. A. Burrus, J. P. Harbison, L. T. Florez, A. C. Gossard, and J. H. English, "Nonlinear FP etalons and microlaser devices," *SPIE OE/LASE*, No. 1214-03, 1990.

[38] N. Schunk and K. Petermann, "Noise analysis of injection-locked semiconductor injection lasers," *IEEE J. Quantum Electron.*, vol. 22, No. 5, pp. 642-650, 1986.

[39] S. Haykin, *Communication Systems.* New York: John Wiley & Sons, 1983.

[40] K. Petermann, "Calculated spontaneous emission factor for double heterostructure injection lasers with gain induced mode guiding," *IEEE J. Quantum Electron.*, vol. QE-15, pp. 556-570, 1979.

[41] W. Cheney and D. Kincaid, *Numerical Mathematics and Computing.* California: Brooks/Cole Publishing Company, 1980.

[42] G. E. Forsythe, M. A. Malcolm, and C. B. Moler, *Computer Methods for Mathematical Computations.* New Jersey: Prentice-Hall, 1977.

[43] P. L. Liu, C. Lin, I. P. Kaminow, and J. J. Hsieh, "Picosecond pulse generation from InGaAsP lasers at 1.25 and 1.3 μm by electrical pulse pumping," *IEEE J. Quantum Electron.*, QE-17, pp. 671-674, 1981.

[44] M. Zhang and D. R. Conn, "A dynamic equivalent circuit model for vertical cavity surface emitting lasers," submitted to *Microwave and Optical Technology Letters.*

[45] X. Wu, "Field simulation and calibration in external electro-optic sampling". Ph.D. dissertation, McMaster University, July 1996.

[46] M. Shinagawa and T. Nagatsuma, "An automated electro-optic probing system for ultra-high-speed IC's," *IEEE Trans. Instrumentation and Measurement*, vol. 43, No. 6, pp. 843-847, 1994.

[47] J. A. Valdmanis, G. Mourou and C. W. Gabel, "Picosecond electro-optic sampling system," *Appl. Phys. Lett.* **41**, pp. 211-212, Aug. 1982.

[48] K. J. Weingarten, M. J. W. Rodwell and D. M. Bloom, "Picosecond optical sampling of GaAs integrated circuits," *IEEE J. Quantum Electron.*, vol. QE-24, pp. 198-220, 1988.

[49] D. Conn, X. Wu, J. Song and K. Nickerson, "Calibration of external electro-optic sampling using field simulation and system transfer function analysis," *IEEE MTT-S Int. Microwave Symp. Dig.*, pp. 221-224, Atlanta, Georgia, 1993.

[50] A. Yariv and P. Yeh, *Optical Waves in Crystals.* New York: John Wiley & Sons, 1982.

[51] A. Yariv, *Optical Electronics, Fourth Edition.* Philadelphia: Saunders College Publishing, A division of Holt, Rinehart and Winston, Inc., 1991.

[52] M. Y. Frankel, S. Gupta, J. A. Valdmanis and G. A. Mourou, "Terahertz attenuation and dispersion characteristics of coplanar transmission lines," *IEEE Trans. Microwave Theory Tech.*, vol. 39, pp. 910-915, June 1991.

[53] G. Hasnain, A. Dienes and J. R. Winnery, "Dispersion of picosecond pulse in coplanar transmission lines," *IEEE Trans. Microwave Theory Tech.*, vol. 34, pp. 738-741, 1986.

[54] S. S. Bedair and I. Wolff, "Fast, accurate and simple approximate analytic formulas for calculating the parameters of supported coplanar waveguides for MMIC's," *IEEE Trans. Microwave Theory Tech.*, vol. 40, pp. 41-48, 1992.

[55] M. Zhang, Z. Bi and J. Litva, "Boundary conditions for FD-TLM method," *IEEE AP-S Int. Symp. Dig.*, pp. 550-553, Ann Arbor, Michigan, June 1993.

[56] X. Wu, D. Conn, J. Song and K. Nickerson, "Invasiveness of $LiTaO_3$ and GaAs probes in external electro-optic sampling," *IEEE/OSA J. Lightwave Tech.*, vol. 11, pp. 448-454, Mar. 1993.

[57] M. Shinagawa and T. Nagatsuma, "Electro-optic sampling using an external GaAs probe tip," *Electron. Lett.*, vol. 26, pp. 1341-1343, Aug. 1990.

[58] J. A. Valdmanis and S. S. Pei, "A non-contact electro-optic prober for high speed integrated circuits," in *Picosecond Electronics and Optoelectronics II*, Springer-Verlag, New York, pp. 4-10, 1987.

[59] M. S. Heutmaker, G. T. Harvey, D. G. Cruickshank and P. E. Bechtold, "Electrooptic sampling of silicon integrated circuits using a GaAs probe tip," *Digest. of 17 Int. Conf. Quantum Electron IQEC*, pp. 50-53, 1990.

[60] B. P. Lathi, *Signals, Systems, and Controls.* New York: Index Educational Publishers, 1974.

[61] D. Conn, H. X. Wu, and M. Zhang, " Full wave electromagnetic simulation of electrooptic high-speed probes," *Optical and Quantum Electronics*, vol. 28, pp. 765-782, 1996.

[62] J. Song, D. Conn, X. Wu, and K. Nickerson, "An equivalent circuit model of the optical probe in electro-optical sampling systems," *Microwave and Optical Technology Letters*, vol. 6, No. 8, pp. 493-498, June 1993.

[63] G. Hasnain, A. Dienes, and J. R. Winnery, "Dispersion of picosecond pulse in coplanar transmission lines," *IEEE Trans. Microwave Theory Tech.*, vol. MTT-34, pp. 738-741, 1986.

[64] S. Haykin, *Neural Networks.* New York: Macmillan College Publishing Company, 1994.

[65] H. Demuth and M. Beale, *MATLAB Application Toolbox - Neural Network.* The Math Works Inc., 1993.

[66] M. Y. Frankel, J. F. Whitaker, and G. A. Mourou, "Optoelectronic transient characterization of ultrafast devices," *IEEE J. Quantum Electron.*, vol. QE-28, pp. 2313-2324, Oct. 1992.